#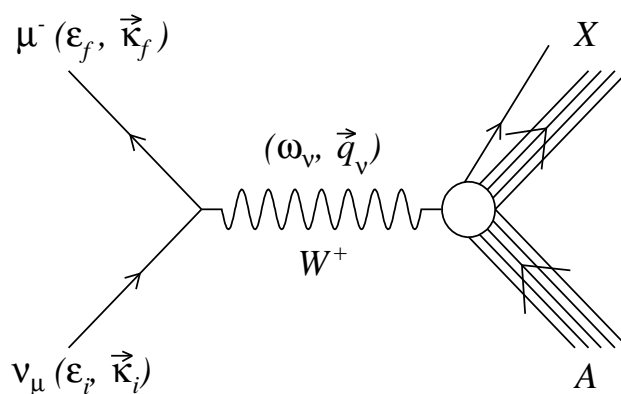 Quasielastic electroweak scattering cross sections in kinematics relevant for accelerator-based neutrino-oscillation experiments

Vishvas Pandey

$$\mu^{-}\,(\varepsilon_f,\,\vec{\kappa}_f)$$

$$X$$

$$(\omega_v,\,\vec{q}_v)$$

$$W^{+}$$

$$\nu_{\mu}\,(\varepsilon_i,\,\vec{\kappa}_i)$$

$$A$$

"On this page, trillions of neutrinos are crossing every second."

Acknowledgements

Abstract

The focus of this thesis is to study the electroweak scattering (of electrons and neutrinos) off nuclei from low energies (10s of MeV) to the intermediate energy region (few GeV) within a continuum random phase approximation (CRPA) model. The CRPA model was originally developed to describe giant-resonance (10s of MeV) physics. The goal of this thesis is to not only focus on the giant-resonance region but also to extend the model to intermediate energies to describe quasielastic (QE) scattering.

Motivation: There are two major motivations of this work. The first motivation comes from the fact that the study of neutrino-nucleus interactions is at the center of accelerator-based neutrino-oscillation experiments. In search of precise measurements of the neutrino-oscillation parameters, a number of accelerator-based neutrino-oscillation experiments are developed in recent years. These experiments, however, face a number of challenges especially related to the limited knowledge of the neutrino-nucleus signal in a detector, resulting in high systematic uncertainties. Major issues arise from the fact that the incident neutrino energy is not precisely known because neutrinos are produced as the decay product of a secondary beam of pions. The neutrino energy is reconstructed based on the kinematics of the outgoing lepton, resulting in a wide-ranged flux, from 10s of MeV to a few GeV. Hence, a number of nuclear effects over a broad kinematical range (from low-energy nuclear excitations, over QE scattering, to multinucleon emission) simultaneously come into play. The Monte-Carlo generators used in the analysis of the experiments are based mainly on relativistic Fermi gas (RFG) based models which can describe the general behavior of the QE cross section sufficiently accurately. But the description becomes poor for smaller momentum transfers, where collective nuclear effects are more prominent. The inadequacy of RFG in describing nuclear effects contributes to the systematic uncertainties. More detailed microscopic nuclear structure models are needed that can describe the neutrino-nucleus scatterings over the whole experimental energy range (10s of MeV to a few GeV).

The second motivation is that neutrino scattering off nuclei offers a great opportunity to study the complexity of the nuclear many-body system even beyond the information accessible in electron- or hadron-nucleus scattering. Using neutrinos as a probe for nuclear physics is a great tool to complement our knowledge of nuclear physics, for example to study the axial structure or the strangeness content of the nucleons. This makes neutrino-nucleus scattering a great testing ground for nuclear structure, many-body mechanisms and nuclear reaction models.

Approach: The model we use in this work takes the description of the nucleus in a mean-field (MF) approach as the starting point. We obtain the mean-field potential by solving the Hartree-Fock (HF) equations using a Skyrme (SkE2) two-body nucleon-nucleon interaction. In this potential we compute the bound and the continuum single-particle wave functions. In addition, we introduce long-range nuclear correlations by means of the CRPA framework. We solve the CRPA equations using a Green's function method. A number of issues required careful attention before the CRPA formalism was suited for the description of neutrino-nucleus scattering over the broad energy range that is covered in this work.

The first issue was related to the description of giant resonances. A limitation of the RPA formalisms is that only the escape-width contribution to the final-state interaction is accounted

for and the spreading width of the particle states is neglected. This affects the description of giant resonances in a underestimated width and overestimated height. We introduced a folding procedure with a Lorentzian which makes the description of the giant resonance region more realistic. Other issues are related to extend the formalism to intermediate energies. At intermediate energies relativistic effects become important. We implemented relativistic kinematic corrections which shifts the QE peak at roughly the right position. Further, the original SkE2 residual force was optimized against ground-state and low-excitation energy properties of spherical nuclei where the virtuality Q^2 of the nucleon-nucleon vertices is small. At high virtualities Q^2, the SkE2 force tends to be unrealistically strong. We remedy this by introducing a dipole hadronic form factor, with a cut-off parameter, at the nucleon-nucleon interaction vertices. We optimized the parameter in a χ^2 test of the comparison of $A(e,e^{'})$ CRPA cross sections with a comprehensive set of experimental data in the QE region. Also, in order to take into account the influence of the nuclear Coulomb field on the outgoing lepton, we implemented a 'modified effective momentum approximation approach'.

Results and Conclusions: In order to asses and test the reliability of the updated model, we performed an extensive study of inclusive QE electron-nucleus scattering. We compared our HF and CRPA predictions with the experimental data over a broad range of three- and four-momentum transfers: $95 \lesssim q \lesssim 1050$ MeV/c, and $0.009 \lesssim Q^2 \lesssim 0.900$ (GeV/c)^2 on ^{12}C, ^{16}O and ^{40}Ca nucleus. We also compared the separated longitudinal and transverse responses on ^{12}C, for $300 \lesssim |q| \lesssim 570$ MeV/c with the data. A successful overall description of the data, and especially the low-energy nuclear excitations ($\omega < 50$ MeV), confirmed the reliability of the model from the low-energy to the QE region. We then moved to neutrino scattering and calculated ^{12}C(ν_μ, μ^-) cross sections at the kinematics of MiniBooNE and T2K-like experiments. We illustrate how low-energy nuclear excitations are induced by neutrinos and draw special attention to contributions where nuclear-structure details become important, but remain unobserved in RFG-based models. We show that low-energy excitations can account for non-negligible contributions to the signal of accelerator-based neutrino-oscillation experiments, such as MiniBooNE and T2K, especially at forward neutrino-nucleus scattering.

We performed flux-folded double-differential cross section calculations off ^{12}C and compared them with MiniBooNE (CCQE neutrino and antineutrino) and T2K (inclusive QE) measurements. A comparison of the flux-unfolded total cross section with the CCQE measurements of MiniBooNE and T2K is also performed. Our predictions successfully describe the gross features of the measurements but underestimate the data in the dip region. This can be attributed to the lack of processes beyond the QE ones in our model. Focusing on forward scattering bins, we made a detailed analysis of the flux-folded double-differential cross sections and presented a comparison with MiniBooNE and T2K data. The low-energy excitations seem to have non-negligible contribution to cross sections at forward scattering angles.

We also performed a detailed comparison between two different theoretical models, our CRPA model and the RPA model of Martini *et al.*. We compared electron neutrino and muon neutrino cross sections, relevant for the experiments looking for muon-neutrino to electron-neutrino oscillations. Some non-trivial differences arise from the different lepton masses, and become evident at low neutrino energies.

Contents

*"A billion neutrinos go swimming in heavy water,
one gets wet."*

Michael Kamakana

1

Introduction

The quest for the smallest building blocks of matter led to the foundation of elementary particle physics. By using higher and higher energies in particle accelerators, reaching smaller and smaller length scales, a "zoo" of elementary particles was discovered. This led to the standard model (SM) of particle physics. The SM defines twelve matter particles, the fundamental building blocks of all matter in the observable universe. They can be classified in two categories, one consists of six quarks and the other of six leptons. All these matter particles have spin $\frac{1}{2}$ and are known as fermions. The matter particles interact with each other through four fundamental forces: gravitation, electromagnetism, strong interaction and weak interaction. These forces can be described by the exchange of force particles known as bosons. SM consists of an additional particle Higgs boson which gives rise to the masses of all the elementary particles in SM.

Neutrinos are the most abundant and yet the least known elementary matter particles. The history of the neutrino began with the investigation of β-decay in the 1930s, when Wolfgang Pauli first postulated the neutrino. Ever since, the neutrino's properties have been shown to be out of the ordinary. Being leptons, they do not participate in strong interactions, having no electric charge, they are not involved in electromagnetic interactions either. They mainly interact only via weak interactions which makes their experimental investigation (and hence their study) challenging. The study of the fundamental properties of neutrinos has been a strong and active area of research among particle and nuclear physicists. The investigation of the basic nature of neutrinos can help to explain many important questions about our universe, for example why is there matter-antimatter asymmetry? Physicists are probing neutrinos to explore many yet unanswered questions:
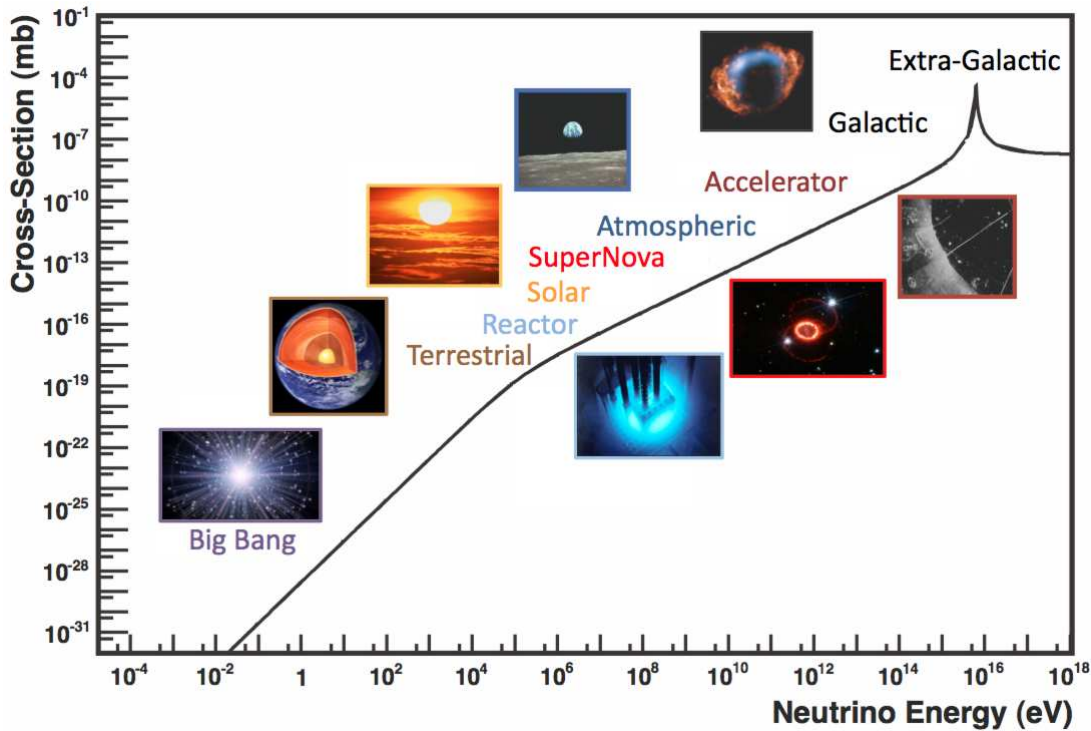
FIGURE 1.1: Neutrino sources across a wide range of energies. The curve shows the antineutrino cross section on a free electron ($\bar{\nu}_e e^- \to \bar{\nu}_e e^-$) as a function of neutrino energy (for a massless neutrino). The peak at 10^{16} eV is due to the W^- resonance. The figure is taken from Ref. [1].

- What is the neutrino mass ordering, is it normal or inverted?

- What are the absolute masses of neutrinos?

- Are neutrino Dirac, i.e., do they manifest the same matter/antimatter symmetry as in quarks and charged leptons, or do they have a completely different structure, i.e., are they Majorana particles?

- Is there CP violation in the neutrino sector?

- Are there additional sterile neutrinos?

Neutrinos are generated by a variety of sources: natural (solar, atmospheric, etc.) and artificial (reactor, accelerator) ones. The energy range of neutrinos varies from few eV to EeV depending on the source. Fig 1.1 shows how neutrino energies vary for the wide variety of neutrino sources [1]. In this figure, the electroweak cross section for antineutrino scattering off a free electron ($\bar{\nu}_e e^- \to \bar{\nu}_e e^-$) is plotted as a function of neutrino energy. Because of the diverse sources and the wide range of energies, neutrino studies extend over a variety of domains from astrophysics, cosmology, particle physics to nuclear physics.

- **Astrophysics:** Neutrinos play an important role in various astrophysical processes ranging from the Sun to supernovae, to distant galaxies. The nuclear reactions that power the sun generate a large flux of neutrinos. The dynamics of the neutron rich environment

of core-collapse supernovae is controlled by neutrino interactions. These supernovae emit spectacular amounts of neutrinos. Since the neutrino does not interact via electromagnetic and strong interactions and its mass is very small, it hardly interacts between its source and the detectors. Hence it carries precise information about extreme environments, complex processes and otherwise inaccessible sources. Because of their important impact on our understanding of the universe, the first observation of solar neutrinos (1960's) and supernovae neutrinos (1980's) in fact resulted in a shared Nobel Prize in physics in 2002.

- **Particle Physics:** The long-standing "solar neutrino deficit" turned out to be the first direct indication of neutrino oscillations and hence neutrino masses. Since neutrino masses are set to zero in the SM, any evidence of a nonvanishing neutrino mass indicates physics beyond the standard model. The firm evidence of neutrino oscillation in Super Kamiokande and SNO experiments also resulted in Nobel Prize in physics in 2015.

- **Nuclear Physics:** Many neutrino experiments are performed using nuclear targets. Most of our present knowledge about the nuclear structure arose from experiments with electromagnetic and hadronic probes. Using neutrinos as a probe can enhance our knowledge about hadrons, for example about the axial structure or the strangeness content of hadrons. This gives an opportunity to probe the complementary information, beyond the electron-nuclear scattering ones, about the complex nuclear environment and provide a testing ground for nuclear structure, many-body mechanisms and reaction models.

The research conducted in the later part of the 20th century strongly suggested that neutrinos oscillate between different flavors. The oscillation of neutrinos is possible only if the mass and flavor eigenstates do not coincide and if different neutrinos have different masses. This has impact on various physics processes. In the following section, we discuss the evidence for neutrino oscillations, its implications, and briefly describe oscillation parameters and their accessibility in various experiments.

1.1 Neutrino oscillations

Major evidence for a nonvanishing neutrino mass emerged from neutrino oscillation searches. The observation of oscillations is, however, sensitive to the mass-squared differences Δm^2 and does not allow absolute mass measurements. There are mainly two compelling pieces of evidences, one from solar neutrinos and another from atmospheric neutrinos, that established neutrino flavor oscillations:

- A deficit in the number of muons produced by atmospheric neutrinos. This was observed by a long-baseline accelerator experiment, Super Kamiokande, with the diameter of the earth as baseline. The first evidence of atmospheric neutrino oscillation was presented in 1998 [2]. This deficit can be explained by muon neutrinos oscillating into tau neutrinos with $\Delta m^2_{\mathrm{atm}} \approx 2.3 \times 10^{-3}$ eV^2 and $\sin^2 2\theta \approx 1$ (where, θ is the mixing angle).
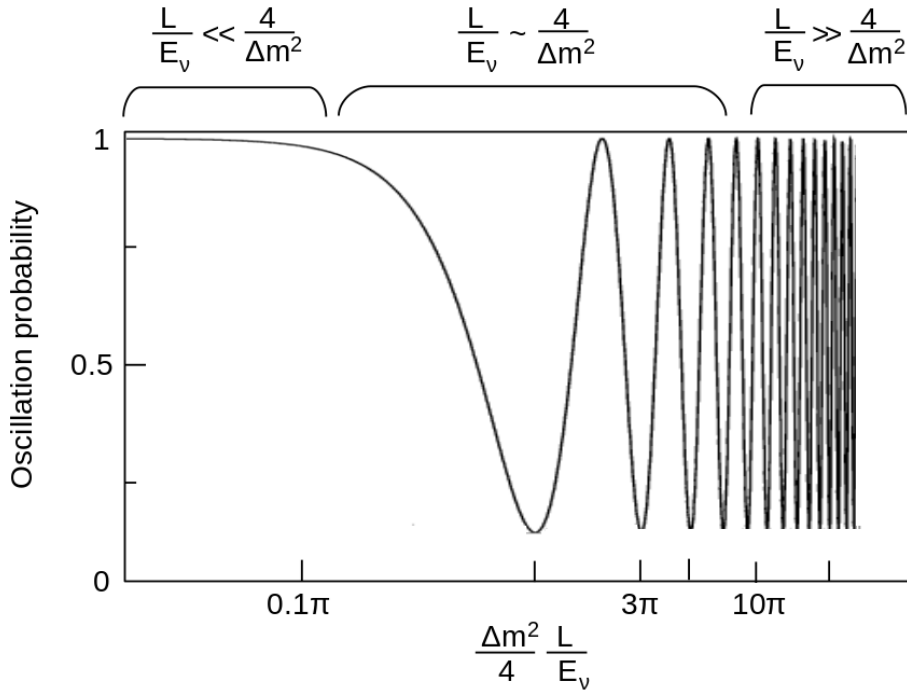
FIGURE 1.2: The oscillation probability is shown as a function of $\frac{\Delta m^2 L}{4 E_\nu}$ for $\sin^2 2\theta = 0.83$. Three possible cases are distinguished: (i) no oscillations $\frac{L}{E_\nu} \ll \frac{4}{\Delta m^2}$, (ii) maximal sensitivity to oscillations $\frac{L}{E_\nu} \sim \frac{4}{\Delta m^2}$ and (iii) possibility of only averaged oscillation measurement due to finite resolutions for $\frac{L}{E_\nu} \gg \frac{4}{\Delta m^2}$.

- The observation of a solar neutrino deficit. This is confirmed by the observations performed in the Sudbury Neutrino Observatory (SNO) [3], in 2001, together with other solar neutrino results. The same solar neutrino deficit results have been confirmed by the KamLAND experiment using a completely different method in a nuclear power plant. The combined best-fit value is $\Delta m^2_{\text{sol}} = (7.59 \pm 0.20) \times 10^{-5}$ eV^2 and $\theta \approx 34^o \pm 1^o$.

In 2015, Takaaki Kajita and Arthur B. McDonald were awarded the Nobel Prize in physics for their contribution to the Super Kamiokande and the SNO (respectively) experiments, which firmly established neutrino oscillations.

In the 21st century, neutrino investigations expanded in new directions. Over the past decade, the study of neutrino oscillations has been the major focus of neutrino physicists.

In two flavor oscillations, the probability of starting from one neutrino flavor (ν_i) at the source and detecting another flavor (ν_j) at the detector is

$$P(\nu_i \rightarrow \nu_j) \;=\; \sin^2 2\theta \; \sin^2 \left(\frac{\Delta m^2 L}{4 E_\nu} \right). \tag{1.1}$$

This equation has a number of variables:

- **The angle, θ:** This is called the mixing angle. It defines how different flavor states are combined into the mass states. The $\sin^2 2\theta$ determines the amplitude of the oscillation.

  If $\theta = 0$, flavor states are identical to the mass states, i.e., ν_i will propagate from source to detector as ν_i. Clearly in this case, oscillations cannot happen.

  If $\theta = \frac{\pi}{4}$, then all the ν_i will oscillate into the ν_j at some point between the source and detector. The oscillation is maximal in this case.

- **The mass squared difference, Δm^2:** This parameter is the difference in squared masses between the two mass states, $\Delta m^2 = m_1^2 - m_2^2$.

  For oscillations to happen the masses of both mass states must be different.

  This parameter, Δm^2, also sets the limitations on oscillation experiments: (a) only the mass squared difference can be measured and not the absolute mass of either state and (b) for $\Delta m^2 \to -\Delta m^2$, the probability $P(\nu_i \to \nu_j)$ is unaffected. Hence which mass state is larger than the other cannot be determined.

- **The ratio, L/E_ν:** L is the distance between source and detector and E_ν is the neutrino energy. For a given Δm^2, the probability of oscillation changes as one moves away from the source or scans different neutrino energies. Different neutrino source (solar, atmospheric, accelerator, etc.) experiments probe different oscillation regimes, i.e., high-energy accelerator ($E_\nu \approx 100$ GeV, $L \approx 1$ km) cannot check solar neutrino data ($E_\nu \approx 1$ MeV, $L \approx 10^8$ km). There are three possible cases, as shown in Fig. 1.2, for the observation of oscillations:

  (i) $\frac{L}{E_\nu} \ll \frac{4}{\Delta m^2}$: The experiment is too close to the source to develop oscillations.

  (ii) $\frac{L}{E_\nu} \sim \frac{4}{\Delta m^2}$: This is a necessary condition to observe oscillations. It is the most sensitive region.

  (iii) $\frac{L}{E_\nu} \gg \frac{4}{\Delta m^2}$: Several oscillations have already happened between source and detector. In this case, experiments usually measure only an average oscillation probability because the L/E_ν value is not suited to resolve the oscillation pattern.

The search for neutrino oscillations can be performed in two different ways:

- **Appearance mode:** These experiments search for a new neutrino flavor which is not present in the original neutrino beam. Or, they look for an enhancement of the neutrinos of a flavor that was already present. The flavor of the new neutrino is identified by the detection of the corresponding charged lepton produced in the final state, via a charged-current interaction process:

$$\nu_l + N \to l^- + X, \tag{1.2}$$

  with $l =$ e, μ, τ and X the final hadron state. The key issue in these experiments is to understand the background in the detector as this could mimic the appearance signature.

- **Disappearance mode:** In this case, one explores whether less than the expected number of a particular produced neutrino flavor arrives at the detector. Or, whether the spectral shape changes when observed at different distances from a source. The important thing in these experiments is to carefully understand the neutrino beam at the source.

There are several neutrino sources that can be used for the search of neutrino oscillations. Examples include nuclear reactors ($\bar{\nu}_e$), accelerator (ν_e, ν_μ, $\bar{\nu}_e$, $\bar{\nu}_\mu$), atmospheric (ν_e, ν_μ, $\bar{\nu}_e$, $\bar{\nu}_\mu$), solar (ν_e), etc.

For some neutrino-oscillation experiments, e.g., in the case of Sun, L and E_ν can not be varied and L/E_ν is fixed. So the explorable Δm^2 region is already constrained. Under these conditions only a certain range of $(\Delta m^2, \theta)$ combinations can be probed because other choices for the values of these parameters lead to probabilities that are too small for observations.

Accelerator-based experiments have the major advantage that one can vary L and E_ν independently. For a given Δm^2, the experiment can be designed to achieve the maximal sensitivity to the oscillation probability, i.e., the experiment should be constructed such that

$$\frac{\Delta m^2 L}{4 E_\nu} = \frac{\pi}{2} \ . \tag{1.3}$$

Thereby, both the beam energy E_ν and the baseline L can be adjusted. In principle, one could maximize the baseline L and minimize the beam energy E_ν. In practice, however, as one increases the baseline L, the neutrino beam diverges and the surface area of the detector has to grow (and so does the cost). Also, with a decrease in E_ν, the neutrino cross section decreases, so the running time to collect sufficient events increases (and again the cost increases). Experimentalists have to determine an optimum (L/E_ν) combination for the oscillation measurements [4].

A schematic overview of a long-baseline experiment is shown in Fig. 1.3. A beam is generated in the accelerator and first goes through a detector nearby, called the near detector, in order to measure the initial beam before any oscillations occur. The beam is then pointed at a detector a few hundreds of kilometers away. This detector is called the far detector. The far detector has to be large, in order to detect enough neutrinos to make a reasonably precise analysis. Usually, the same technology is used to build both the near and the far detector in order to minimize systematic errors.

We discuss the details of accelerator-based neutrino-oscillation experiments in the following subsection. We will briefly present an overview of different accelerator-neutrino oscillation experiments, their physics goals, systematic details, their status and their role in the measurement of different oscillation parameters.

1.1.1 Accelerator-based neutrino-oscillation experiments

The mixing of the three established neutrino flavors has been studied and confirmed by consistent results from a variety of experiments. However, precision measurements of the oscillation parameters θ_{13}, θ_{23}, Δm_{13}^2, Δm_{23}^2, the neutrino mass hierarchy and the CP violating phase δ_{CP} are still in progress in many accelerators-based neutrino-oscillation experiments. The aim of these experiments is either directly measuring those parameters, or indirectly contributing to
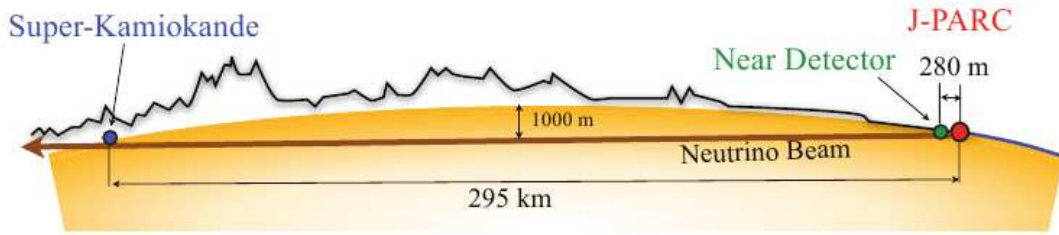
FIGURE 1.3: A schematic example (T2K experiment [5]) of a long-baseline neutrino oscillation experiment. The near detector is at 280 m away while the far detector is at 295 km away from the source.

Experiment	Nuclear Target	Neutrino Type	CCQE Event Selection
MiniBooNE	CH_2	$\nu_\mu, \bar{\nu}_\mu$	$1\mu + 0\pi$ (Michel e^- ID)
T2K	C_8H_8	ν_μ	$1\mu + 0\pi$
MINERvA	CH	$\nu_\mu, \bar{\nu}_\mu$	1μ + recoil consistent with CCQE Q^2
ArgoNeuT	Ar	$\nu_\mu, \bar{\nu}_\mu$	$1\mu + 0\pi$
NOvA ND	CH_2	ν_μ	1μ + multi-variate
SciBooNE	C_8H_8	ν_μ	(1μ) or $(1\mu + 1p)$
MINOS	Fe	ν_μ	$1\mu + (E_{had} < 225$ MeV$)$
NOMAD	64% C, 22% O, 6% N 5% H, 1.7% Al	$\nu_\mu, \bar{\nu}_\mu$	(1μ) or $(1\mu + 1p)$ (accepted)

TABLE 1.1: An overview of the experiments that have performed ν_μ CCQE cross-section measurements. The nuclear targets, neutrino types used and the definition of CCQE events are listed. The corresponding kinematics and measured cross sections are listed in Table 1.2.

"direct" measurements by producing data that can help in reducing the systematic and theoretical uncertainties.

In recent years, there have been substantial developments in accelerator-based neutrino oscillation searches. As discussed in Sec. 1.1, most of these experiments have a baseline of hundreds of km long and run in the 1 GeV energy region. In this region, the major contributions to the cross section arise from charged-current quasielastic (CCQE) reaction processes. Neutrino-nucleus scatterings and the different reaction channels will be discussed in Sec. 1.2.

We briefly compare the recent studies of CCQE events at various accelerator-based neutrino oscillation experiments (MiniBooNE [6, 7], T2K [8, 9], MINERvA [10, 11], ArgoNeut [12], NOvA [13], SciBooNE [14], MINOS [15] and NOMAD [16]), in Tables 1.1 and 1.2. In Table 1.1, we list different nuclear targets and the type of neutrino beam used in these experiments. We also show how different experiments select the CCQE events. Tabel 1.2 mainly compares the kinematics probed in the different experiments: the range of incoming neutrino energies, the scattering angle and the kinetic energy range of the outgoing muon. We also list the different types of muon measurements (cross sections, axial mass extraction, etc.) performed in these experiments.

From the comparison of the CCQE analysis in different experiments in Table 1.1 and Table 1.2, one can conclude the following:

Experiment	E_ν range (GeV)	Muon Angle $\theta_\mu(^\circ)$	Muon KE T_μ (GeV)	CCQE Results
MiniBooNE	$0.2 < E_\nu < 3$	$0 < \theta_\mu < 180$	$0.2 < T_\mu < 2$	$d^2\sigma/dT_\mu d\theta_\mu$ $d\sigma/dQ^2$ $\sigma(E_\nu), M_A$
T2K	$0.2 < E_\nu < 30$	$0 < \theta_\mu < 80$	$0 < T_\mu < 30$	$\sigma(E_\nu)$
MINERvA	$1.5 < E_\nu < 10$	$0 < \theta_\mu < 20$ (MINOS-match)	$1.5 < T_\mu < 10$	$d\sigma/dQ^2$
ArgoNeuT	$0.5 < E_\nu < 10$	$0 < \theta_\mu < 40$ (MINOS-match)	$T_\mu > 0.4$	# protons
NOvA ND	$0.2 < E_\nu < 3$	$0 < \theta_\mu < 45$	$0 < T_\mu < 1.4$	$\sigma(E_\nu)$
SciBooNE	$0.2 < E_\nu < 3$	$0 < \theta_\mu < 60$	$0.1 < T_\mu < 1.1$	$\sigma(E_\nu)$
MINOS	$0.2 < E_\nu < 6$	$0 < \theta_\mu < 180$	$0 < T_\mu < 5$	M_A
NOMAD	$2.5 < E_\nu < 300$	$0 < \theta_\mu < 100$	$T_\mu > 2$	$\sigma(E_\nu)$ M_A

TABLE 1.2: An overview of the energy ranges of neutrinos, muon scattering angle, muon kinetic energy and the measured cross sections of ν_μ CCQE scatterings in different experiments.

- **Nuclear target:** Most of the experiments use a nuclear target rich in carbon. The ArgoNeut and MINOS experiments use the heavier nuclear targets Ar and Fe, respectively.

- **Neutrino beam:** The neutrino beams in all of these experiments are generated as a result of pion decay into muons and hence the CCQE analysis is mainly performed for muon (anti)neutrinos.

- **CCQE event selection:** Different experiments use different criteria to identify CCQE events. The definition of CCQE events is mainly based on their hadron identification ability. MiniBooNE and MINOS identify a muon with restrictions on additional activity from hadrons (pions, etc.) in the event, without explicitly identifying knocked-out nucleon(s) because of their higher tracking thresholds (the Cherenkov threshold in the MiniBooNE case and from the presence of passive steel plates in MINOS). SciBooNE and NOMAD have detectors with fine-grained tracking capabilities, using recoil proton information to identify CCQE events.

- **Neutrino energies:** The neutrino energies range from hundreds of MeV to a few GeV for MiniBooNE, NOvA, SciBooNE and MINOS while it goes up to tens of GeV for T2K, MINERvA and ArgoNeuT. NOMAD was a higher energy neutrino experiment with energy ranging up to 300 GeV.

- **Angular acceptance:** The detectors have very different geometric acceptances according to their configurations. Experiments like MINERvA, MINOS, T2K-ND280 and SciBooNE have planar tracking geometries and hence their acceptances are concentrated in the forward and backward regions with respect to the neutrino beam direction. MiniBooNE, on the other hand, has full 4π acceptance. The difference in angular acceptance can play a significant role, but its importance depends on the incident neutrino energy:
(a) At lower energies (< 1 GeV), the outgoing particles are more isotropically distributed. So, if the angular acceptance is limited, a large fraction of the events will be inaccessible for the analysis.
(b) At higher energies, the particles are boosted into the forward direction. So the impact
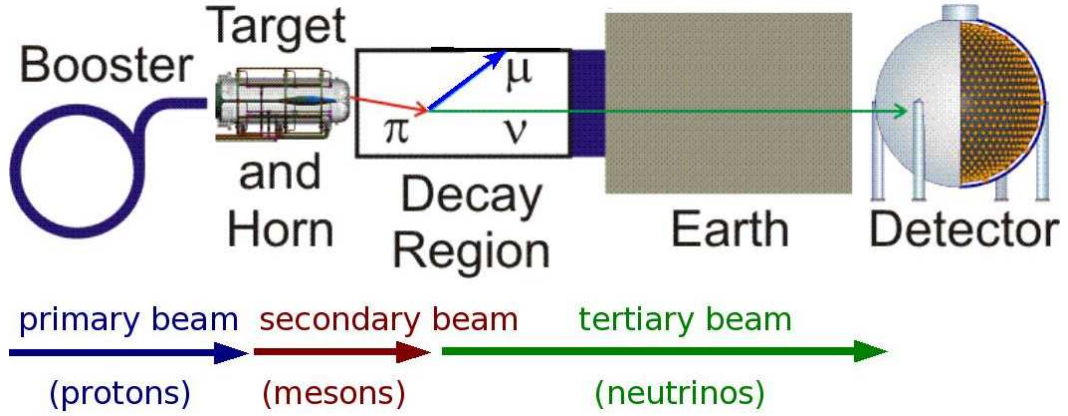
FIGURE 1.4: A schematic overview of the MiniBooNE beamline and detector [6].

of the limited wide-angle acceptance will be significantly smaller.

- **Muon kinetic energies:** The range of kinetic energies (KE) of the outgoing muon is distributed according to the incoming neutrino energy and the angular acceptance of the detector.

Now, we move our discussion to specific experiments. We briefly present the details of the MiniBooNE, T2K and MINERvA experiments.

(i) MiniBooNE

The MiniBooNE (Mini Booster Neutrino Experiment) experiment was built at Fermilab to study the short-baseline neutrino oscillations indicated by the LSND experiment. The aim of the experiment is to detect the $\nu_e(\bar{\nu}_e)$ appearance signal from the $\nu_\mu(\bar{\nu}_\mu)$ beam in the $\Delta m^2 \sim 1$ eV^2 region through CCQE interactions.

$$\nu_\mu \xrightarrow{\text{oscillation}} \nu_e + n \rightarrow e^- + p, \tag{1.4}$$

$$\bar{\nu}_\mu \xrightarrow{\text{oscillation}} \bar{\nu}_e + p \rightarrow e^+ + n. \tag{1.5}$$

The baseline $L \sim 500$ m and the energy $E_\nu \sim 800$ MeV are such that the ratio L/E_ν matches the signal reported by the LSND experiment, and suitable to test the mixing with $\Delta m^2 \sim 1$ eV^2.

Beamline and flux: The beamline of MiniBooNE, the Booster Neutrino Beamline (BNB), consists of three main components, as shown in Fig 1.4.

- **Primary proton beam:** Protons are accelerated to 8 GeV kinetic energy in the Fermilab Booster synchrotron and fast-extracted in 1.6 μs to the BNB. These protons collide with a beryllium (Be) target, on a 1.75 (g/cm^3) interaction length, centered in a magnetic focusing horn. This collision creates a shower of mesons.
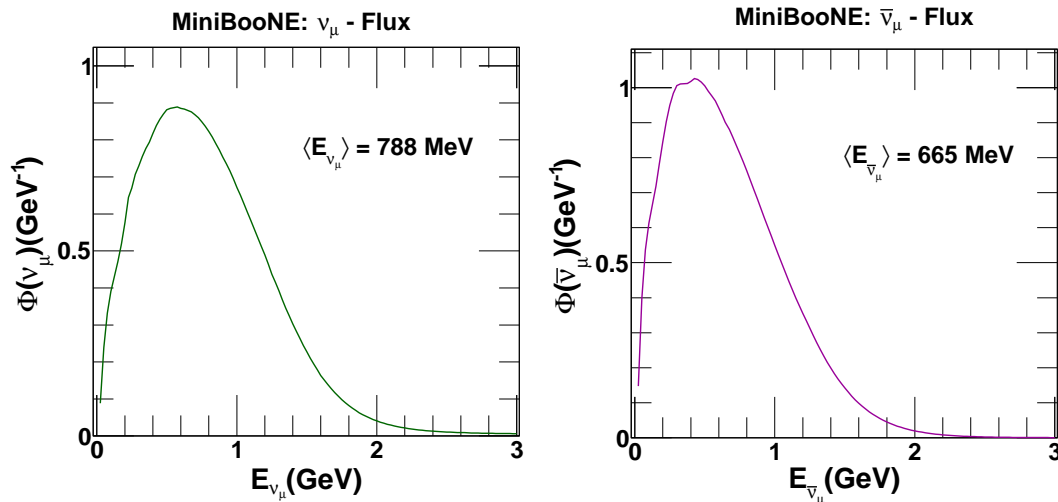
FIGURE 1.5: Predicted ν_μ (left) [6] and $\bar{\nu}_\mu$ (right) [7] flux at the MiniBooNE detector.

- **Secondary mesons:** Mesons in the secondary beam are focused using a toroidal magnetic field, $\pi^+(\pi^-)$ for $\nu(\bar{\nu})$ mode, and serve to direct the neutrino beam. The horn simultaneously defocuses $\pi^-(\pi^+)$ to reduce the background $\bar{\nu}(\nu)$ interactions in $\nu(\bar{\nu})$ mode. The decay in-flight of the pion leads to the final neutrino beam.

- **Tertiary neutrino beam:** It consists of mainly $\nu(\bar{\nu})$, goes towards the downstream detector. The $\nu(\bar{\nu})$ beam's energy is peaked around 800 (650) MeV.

The neutrino flux, at the detector, is calculated using a GEANT4-based [17] simulation. The simulation takes into account proton transport to the target, production of mesons in the collision of the proton-on-Be target and transport of the resulting particles through the horn and decay volume. In Fig. 1.5, we show the MiniBooNE $\nu_\mu(\bar{\nu}_\mu)$ energy distribution with an average energy around 788 (665) MeV. The contamination of non-$\nu_\mu(\bar{\nu}_\mu)$ neutrino types in $\nu_\mu(\bar{\nu}_\mu)$ is treated as background.

Detector: The MiniBooNE detector, as shown in Fig. 1.4, is a 12.2 m diameter spherical Cherenkov detector filled with ~ 800 tons of undoped mineral oil (CH_2) and located at ~ 500 m from the target. The volume in the tank is optically separated into an inner (with diameter 11.5 m) and outer (35 cm thick) region. The inner region is covered with 1280 8-inch photomultiplier tubes (PMTs) and the outer region is covered with 240 8-inch PMTs, which record the light produced by the charged particles entering or exiting the detector volume. The PMT timing information is used to identify and separate particles who during their transit emit a significant amount of Cherenkov light.

A schematic illustration of a CCQE process in MiniBooNE is shown in Fig. 1.6. The primary Cherenkov ring is produced by the muon (anti-muon) followed by a weaker Cherenkov ring from the electron (positron). This two-fold signal defines the CCQE interaction. The nucleon is often below the threshold and hence scintillation from the emitted nucleon(s) is not observed. The CCQE events are identified as those containing only one muon and one Michel decay electron arising from the $\mu \to e$ decay. The single Michel electron excludes the possibility of a charged
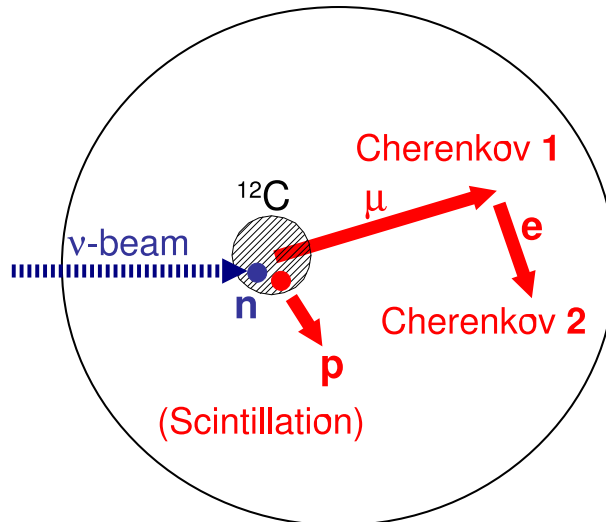
FIGURE 1.6: Illustration of CCQE event in the MiniBooNE detector [6].

pion in the final state because a charged pion would lead to a second Michel decay. So the CCQE events are defined as one muon and no pion in the final state. The disadvantage of not detecting the final nucleon is that the possibility of contributions stemming from multinucleon knock-out cannot be separated and are considered to be "CCQE" by (experimental) definition. The pion absorbed in the target nucleus is regarded as the primary background. These events have the same final state and are called "CCQE-like" events. The size of this background is partially constrained by the measured rate of the CC events with a pion in the final state. A natural advantage of the MiniBooNE Cherenkov detector is its spherical symmetric geometry which allows for angular acceptance over the full 4π of solid angle of the muon produced in the CCQE interaction.

Interaction Model: In order to estimate the neutrino interaction rates MiniBooNE uses NU-ANCE v3 as event generator [18]. The generator considers all the interaction processes expected in the energy region active in MiniBooNE. The NUANCE generator includes following components:

(a) a relativistic Fermi gas (RFG) model for CCQE (and neutral-current elastic) scattering in carbon [19],

(b) a baryonic resonance model for single and multipion production [20],

(c) a coherent CC/NC single-pion production model [21],

(d) a deep inelastic scattering model [22, 23], and

(e) a final-state interaction model [18].

CCQE interactions are the dominant neutrino interaction process at MiniBooNE kinematics, and account for $\sim 40\%$ of the events. This process is simulated with the RFG model [19]. A dipole axial form factor is used with an adjustable axial mass, M_A. A Pauli blocking parameter, κ, is used to allow to describe the data at low momentum transfer. The Fermi momentum is set to 220±30 MeV/c and binding energy is set to 34±9 MeV for carbon [24]. The parameters M_A and κ were extracted from CCQE data and were determined to be $M_A^{eff} = 1.35$ GeV and

$\kappa = 1.007$. The superscript "eff" on M_A is introduced to allow for the possibility that nuclear effects play an important role for the axial mass measurement and that scattering from bound and bare nucleons may be different.

From the neutrino data sample 146,070 CCQE events are extracted with an estimated 26% efficiency and 77% purity. The antineutrino sample includes 71,176 events with and estimated 29% efficiency and 61% purity. However for the antineutrino case there is an additional background from neutrino events because the MiniBooNE detector is not magnetized. The neutrino events from the antineutrino sample consist of 20% of the events.

After 10 years of data taking, MiniBooNE has reported cross-section measurements of CCQE neutrino and antineutrino scatterings using the first largest sample of CCQE interactions [6, 7]. They did the first measurement of the double differential cross section, $d^2\sigma/dT_\mu d\cos\theta_\mu$, and the differential cross section, $d\sigma/dQ^2$, for both neutrinos and antineutrinos. For the advantage of comparison with historical data, MiniBooNE also reported the total cross section as a function of reconstructed neutrino energy. The cross section is measured over the kinematic range, $0.2 < E_\nu < 3$ GeV, $0 < \theta_\mu < 180^o$ and $0.2 < E_\mu < 2$ GeV. The neutrino measurements are on C while the antineutrino measurements are on a CH_2. So there is an additional contribution from two free protons, which however was subtracted to report the Carbon-only measurements. The major uncertainty in the MiniBooNE measurements arises from the predicted flux. The total flux uncertainty is 10% in the neutrino and 17% for the antineutrino case. The cross section data are not used to determined the flux.

The broad definition of the CCQE and expanded kinematic coverage in MiniBooNE lead to larger cross sections than predicted in QE calculations. These results, however, initiated discussions about the possible connection between the enhanced observed cross sections in neutrino- and electron-nucleus scatterings.

(ii) T2K

The Tokai-to-Kamioka (T2K) experiment is a long-baseline neutrino oscillation experiment. T2K collaboration aim to study the ν_e appearance signal from a ν_μ beam at a distance where the oscillation is maximum for the produced neutrino beam energy, and to measure or constrain the mixing angles θ_{13} and θ_{23}, the mass splitting $|\Delta m^2_{32}|$ and the CP-violating phase δ_{CP}. T2K consists of an accelerator-generated neutrino beam, a near detector 280 m downstream of the neutrino beam target and a far detector, Super-Kamiokande (SK), located at 295 km away at an angle of 2.5 degrees from the axis of the neutrino beam. The near detector is composed of a detector positioned on the axis of the neutrino beam, called INGRID, and a detector 2.5 degrees off axis, in line with SK, called ND280. The INGRID detector is used to monitor the beam profile and stability. ND280 is used to measure neutrino fluxes and ν_μ cross sections.

T2K sends a beam of muon neutrinos produced at the Japan Proton Accelerator Research Center (J-PARC) 295 km away to the Super-Kamiokande (SK) detector. The muon neutrinos are produced mainly from the decay of pions, $\pi \to \mu + \nu_\mu$, generated in the interactions of 30 GeV protons from the J-PARC main ring on a carbon target. T2K is the first to employ the
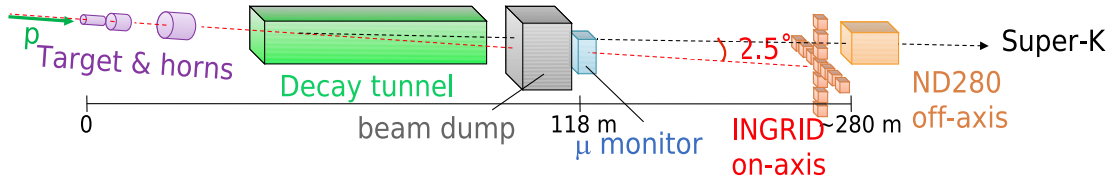
FIGURE 1.7: A schematic overview of the T2K beamline and detector [8].

"off-axis" beam configuration, i.e., the beam axis is directed (slightly) away from the detectors. The neutrino beam is 2.5^o shifted from the direction of the far detector (SK). With this off-axis configuration, the energy distribution of the ν_μ flux is made more narrowly peaked with an average energy of approximately 600 MeV, optimized to maximize the neutrino oscillation effect at $L = 295$ km.

Beamline and flux: An illustration of the neutrino beamline and near detectors is presented in Fig. 1.7. The protons are extracted and directed towards a 91.4 cm long graphite target aligned at an 2.5^o off-axis angle from Kamioka. The target is installed inside a magnetic horn. The charged mesons, generated by proton scattering off the target, are collected and directed by magnetic horns. Two additional magnetic horns are used to further focus the charged mesons before they enter a 96 m long steel decay volume filled with helium. The mesons further decay into muons and muon neutrinos. A beam dump stops most of the particles in the beam except the neutrinos. Some high-energy muons pass through but are observed by the muon monitor. These monitors provide the information about the track, beam direction and stability.

The flux is predicted using the simulation codes FLUKA2008 [25, 26] and GEANT3.21 [27, 28]. The simulation considers the processes involved in neutrino production, from the interaction of the primary beam proton, to the decay of hadrons and muons that produces neutrinos. In Fig. 1.8, the predicted ν_μ flux at the T2K near detector is shown. The total uncertainty in this flux is about 11%.

Detector: The on-axis near detector, Interactive Neutrino GRID (INGRID), consists of a set of 16 tracking detectors with scintillating bars planes. These planes are constructed with a grid of iron plates spanning the beam axis in horizontal and vertical direction to monitor the beam direction and profile. The off-axis ND280 near detector is used for the cross section analysis. ND280 is a magnetized particle tracking detector. The detector sits inside a magnet which provides a 0.2 T magnetic field for track-sign selection and momentum measurement. The detector is divided in two regions: a dedicated detector for the study of π^0 production P0D and a tracker region comprised of a series of fine-grained scintillating detectors (FGDs) and time projection chambers (TPCs). The tracker is designed to measure neutrino interactions in FGDs. The tracker and P0D are surrounded by electromagnetic calorimeters (ECals) consisting of scintillator bars.

The track ionization in the TPCs provides a powerful particle identification tool. When charged particles enter the TPC, a magnetic field allows the sign selection and momentum reconstruction by measuring the curvature of their path. Once a negative outgoing muon is identified in the FGD and TPC, the ν_μ CC sample is divided into three topological categories based on other particles identified in the event. Events without additional matching tracks, nor a delayed
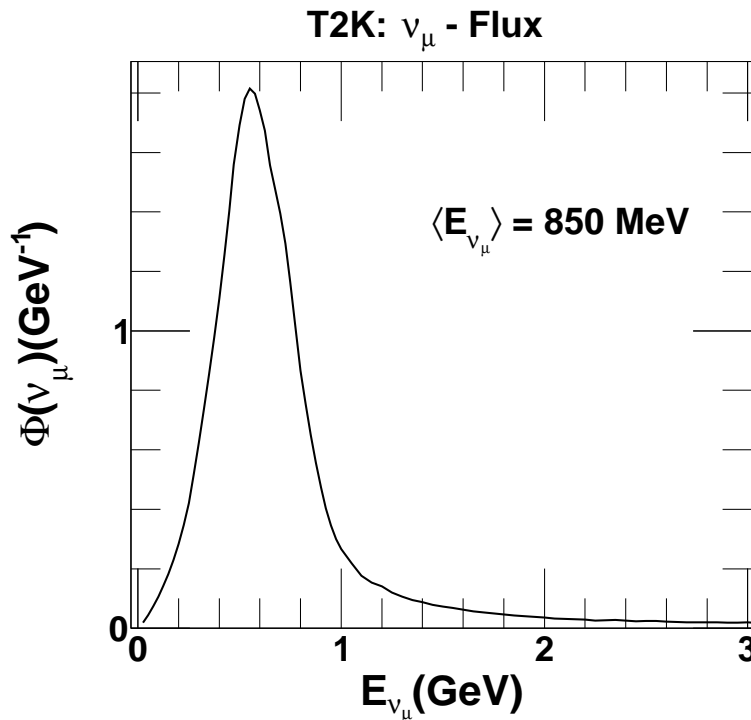
FIGURE 1.8: Predicted ν_μ flux at ND280 Detector in T2K [8].

electron resulting from the $\pi \to \mu \to e$ decay chain, are classified as "CC0π". Based on additional pion tracks or decay electrons found in the event, the remaining events are categorized as "CC1π", if the topology is consistent with CC interaction with a single π^+, otherwise it is categorized as "CC other".

Interaction Model: The neutrino interactions are simulated with the NEUT [29] and GENIE [30] Monte Carlo generators. NEUT is used as the primary generator and GENIE is used for cross checks. The interactions are simulated for quasielastic scattering, single meson production, single gamma production, coherent pion production and nonresonant inelastic scatterings. Both generators use the Llewellyn Smith formalism [31] for the description of the QE scattering cross sections. In this model the hadronic weak current is expressed in terms of two vector form factors, one pseudoscalar form factor and an axial form factor. The two vector form factors are studied in electron elastic scattering experiments and are fixed by the conserved vector current (CVC) hypothesis. The pseudoscalar form factor is assumed to have the form suggested by the partially conserved axial current (PCAC) hypothesis. A dipole form is assumed for the axial form factor with $M_A^{QE} = 0.99$ GeV for GENIE and 1.21 GeV for NEUT. Both GENIE and NEUT use a relativistic Fermi gas model (RFG) to describe the nuclear effects. GENIE also uses short-range nucleon-nucleon correlations in the RFG model and uses the Bodek and Ritchie model [32] to handle kinematics for off-shell scattering.

A number of studies on neutrino interactions have been carried out both with the on-axis and with the off-axis detector. Measurements of the flux-integrated double-differential cross section for the outgoing muon momentum and angle in the inclusive ν_μ CC sample have been published [8]. The CC0π selection results in a 72% pure CCQE sample with a 40% efficiency, from which a

CCQE cross section as a function of E_ν^{QE} is deduced. The CCQE total cross section as a function of reconstructed neutrino energies was also reported recently [9].

With an off-axis neutrino beam, current status of mixing parameter (θ_{23}) measured in T2K is: $\sin^2(\theta_{23}) = 0.514 \pm 0.055$ (0.511 ± 0.055), assuming normal (inverted) mass hierarchy with 68% confidence limit. And the status of mass-squared splitting is: $\Delta m_{32}^2 = (2.51 \pm 0.10) \times 10^{-3}$ eV^2 for normal hierarchy and $\Delta m_{13}^2 = (2.48 \pm 0.10) \times 10^{-3}$eV^2 for inverted hierarchy [33].

(iii) MINERvA

The MINERvA experiment was designed at Fermilab for a dedicated study of neutrino-nucleus interactions. It uses one neutrino beam and measures cross sections on various target nuclei. This allows one to study the nuclear dependence of the different neutrino interactions with a minimum effect of systematic uncertainties. MINERvA uses a finely segmented scintillator detector to measure the muon neutrino and antineutrino interactions on nuclear targets.

Beamline and flux: The neutrinos are produced in the NuMI (Neutrinos at the Main Injector) beam line from a 120 GeV proton beam. The proton beam strikes a graphite target and produces mesons. These mesons are directed by two magnetic horns into a 675 m long helium-filled decay pipe. The magnetic horn is set to focus positive (negative) mesons that results into a neutrino (antineutrino) beam with a peak energy of 3 GeV. The muons produced in meson decays are absorbed by a 240 m thick layer of rock.

The (antineutrino) neutrino flux prediction is generated by a GEANT4-based [17] simulation. The flux energy ranges from 1.5 GeV to 10 GeV with peak energy near 3 GeV.

Detector: The MINERvA detector consists of a fine-grained scintillator tracker surrounded by electromagnetic and hadronic calorimeters on the sides and at the downstream end of the detector. The strips are perpendicular to the z-axis (where z-axis is very nearly the beam axis) and are arranged in planes with a 1.7 cm strip-to-strip pitch. Three plane orientations enable reconstruction of the neutrino interaction point, the track of the outgoing charged particles, and calorimetric reconstruction of the other particles produced in the interaction. MINERvA is located 2 m upstream of the MINOS near detector, a magnetized iron spectrometer, which is used to reconstruct the momentum and charge of the muon. The MINERvA detector's performance is simulated by a tuned GEANT4-based [17] program.

Interaction Model: Neutrino interactions in the detector are simulated using the GENIE neutrino event generator. For quasielastic interactions, the cross section is described by the Llewellyn-Smith formalism [31]. The electromagnetic form factors are used from the fit to electron scattering cross sections. The axial form factors are used in dipole form with an axial mass (M_A) of 0.99 GeV, consistent with deuterium measurements. Other form factors are derived from PCAC or exact G-parity symmetry. The relativistic Fermi gas model (RFG) is used as nuclear model with a Fermi momentum of 221 MeV/c (for ^{12}C) and an extension to higher nucleon momenta to account for short-range correlations [32]. A tuned model of discrete baryon

resonance production is used for inelastic processes [20] and deep-inelastic scattering is simulated using the Bodek-Yang model [34].

MINERvA collected 16,467 event in antineutrino and 29,620 event in neutrino mode with an expected purity of CCQE events of 77% (antineutrino) and 49% (neutrino). The muon momentum is determined from the distance that the muon travels in the MINERvA detector plus the momentum measured in the MINOS near detector. The muon angle is determined using the MINERvA tracking facilities. From these two quantities the (anti)neutrino energy (E_ν^{QE}) and four-momentum transferred (Q_{QE}^2) are determined. Both ν_μ [10] and $\bar\nu_\mu$ [11] cross sections are presented as a function of Q_{QE}^2. The largest systematic error stems from flux uncertainties. The results favor an increase in the transverse response rather than an increased axial mass.

Current status of oscillation parameters: Combining measurements of several (solar, atmospheric, reactor and accelerated-based) neutrino-oscillation experiments, our current knowledge of oscillation parameter is

- $\sin^2(2\theta_{13}) = 0.093 \pm 0.008$, measured by Daya Bay, Double Chooz, and RENO experiments [35].

- $\sin^2(2\theta_{12}) = 0.846 \pm 0.021$, correspond to θ_{sol} (solar) obtained from Kamland, solar, reactor and accelerator results [35].

- $\sin^2(\theta_{23}) = 0.514 \pm 0.055$ (0.511 ± 0.055), assuming normal (inverted) mass hierarchy, measured by T2K [33].

- $\Delta m_{21}^2 \equiv \Delta m_{\mathrm{sol}}^2 = 7.53 \pm 0.18 \times 10^{-5}$ eV^2, combination of KamLAND and solar neutrino experiments [35].

- $\Delta m_{32}^2 = (2.51 \pm 0.10) \times 10^{-3}$ eV^2 for normal hierarchy, and $\Delta m_{13}^2 = (2.48 \pm 0.10) \times 10^{-3}$eV^2 for inverted hierarchy, measured by T2K [33].

- The phase factors δ (non-zero, if neutrino oscillation violates CP symmetry), α_1, α_2 (physically meaningful only if neutrinos are Majorana particles), and the sign of Δm_{32}^2 are currently unknown.

1.2 Neutrino-nucleus scattering

Since neutrino-oscillation experiments are moving into a precision era, a thorough understanding of neutrino interactions in the target's detection material has become essential in order to minimize the systematic uncertainties in the extraction of the neutrino-oscillation parameters. A detailed knowledge of neutrino-nucleus interactions is important to identify the interaction processes at play and to separate the signal from the background. The uncertainties in the determination of the interacting neutrino's energy will pose a serious issue in future oscillation measurements. Once the neutrino-nucleus interaction is sufficiently well understood, the various
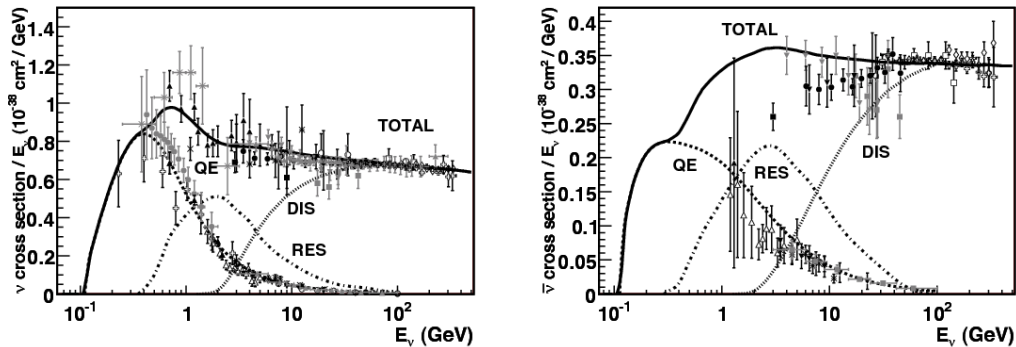
FIGURE 1.9: Total neutrino (left) and antineutrino (right) CC cross sections per nucleon are plotted as a function of (anti)neutrino energy. Various reaction channels contributing to the cross sections are shown separately. The figures are taken from Ref. [1].

interaction models need to be integrated in the event generators in order to reduce the systematic uncertainties in the experimental analysis.

Neutrino-nucleus interactions can be broadly classified into three main categories, depending on the energy of the neutrinos:

- **Low energy:** For neutrinos of the order of 10s of MeVs, the initial and final scattering states are specific nuclear levels. These interactions are of most interests to solar and reactor neutrino-oscillation experiments.

- **Intermediate energy:** In this energy region, of the order of 100s of MeV to a few 10s of GeV, the interaction length is hadronic and hence nuclear effects are important. These are the interactions of most interest to atmospheric and accelerator-based neutrino-oscillation experiments.

- **High energy:** At higher energies the (deep inelastic) scattering scale becomes partonic and hence nuclear effects become less significant.

In this work we focus on intermediate energies. Thereby, the description of the neutrino-nucleus interactions is most diverse and complicated. Various neutrino scattering mechanisms play a role. These different scattering mechanisms mainly fall into three categories:

- **Quasielastic scattering:** The process in which a neutrino scatters off a single bound nucleon and a nucleon is ejected from the target nucleus. This case is referred to as quasielastic (QE) scattering for charged-current neutrino interactions, while neutral current events are traditionally, in an experimental context, referred as elastic scatterings. However, in many neutrino experiments (MiniBooNE, T2K, etc.) QE is defined as the process where one lepton and no pion is detected in the final state and is referred to as "QE-like" scattering. Hence, "QE-like" scatterings, by definition, are contaminated with other processes such as short-range correlations (SRC), meson-exchange currents (MEC) induced multinucleon emissions (np-nh), and pionless resonance decay.
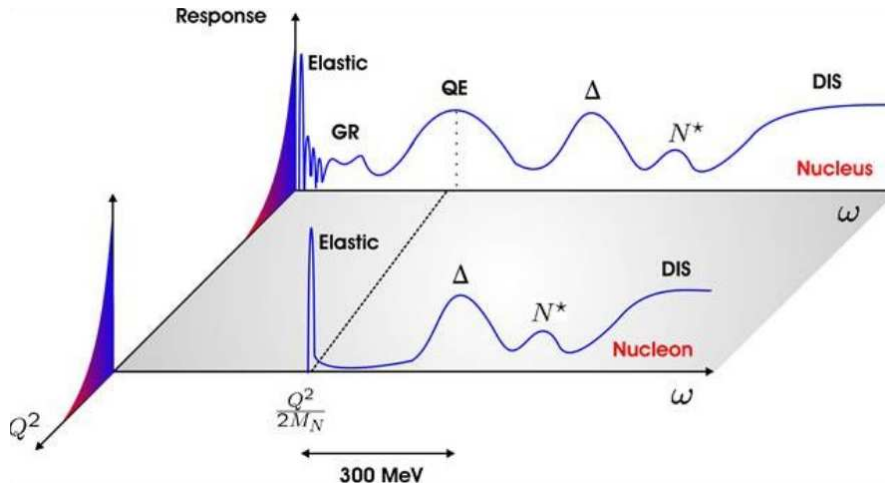
FIGURE 1.10: A schematic picture of the nuclear response to a weak probe as a function of the energy transfer ω and virtuality Q^2.

- **Resonance production:** When an incident neutrino excites the target nucleon to a resonance state, the resulting baryonic resonance (Δ, N^*) decays into a variety of final states with combinations of nucleons and mesons. Neutrino-induced pion-production is one of the dominant process in this region and is extensively studied in neutrino experiments.

- **Deep inelastic scattering:** Neutrinos with sufficiently high energies, break up the target nucleon producing a shower of hadrons in the final state.

Fig. 1.9 shows the contribution of different scattering mechanisms to neutrino and antineutrino cross sections, as a function of incoming (anti)neutrino energy. However, from a nuclear point of view the more important variables in a scattering reaction are energy and four-momentum transfer (ω, Q^2). In Fig. 1.10 we show the nuclear response to a (weak) probe as a function of the transferred energy and four-momentum to the nuclear target. Small energy transfers, just above single-particle energy threshold (~ 15 MeV in light nuclei), result in elastic scattering off the nucleus as a whole followed by the giant resonance (collective excitation of the nucleus). At further increasing energy transfers, the probe scatters off a bound nucleon resulting in a broad quasielastic peak centered around $\omega \sim Q^2/2M_N$ (where M_N is the nucleon mass). Higher transferred energies result in the production of nucleon resonances followed by deep inelastic scattering when the energy transfer is sufficiently high to break up the nucleon. As one can see in these figures (Fig. 1.9 and Fig. 1.10), at intermediate energies several processes overlap and the products of neutrino scattering result into a variety of final states ranging from one (or more) nucleon(s) to more complex states including pions, kaons and/or a collection of other mesons. In this thesis we will focus on quasielastic scattering which is the dominating process at these energies.

Theoretical advancements in CCQE neutrino-nucleus scatterings

The first MiniBooNE measurements for the CCQE cross sections [6] are significantly higher than what was predicted by several theoretical calculations [37]. In order to fit their data, MiniBooNE

increased the value of the axial mass (M_A) (in the nucleon's dipole axial form factor) from what was regarded as the world's averaged value (~ 1 GeV) emerging from bubble chamber experiments to ~ 1.35 GeV. This increased axial mass allowed MiniBooNE to fit their data with the proposition that nuclear effects in the nucleus are influencing the determination of M_A, which should be interpreted as *'effective'*. But this procedure was soon regarded as non-physical and is now understood to be a consequence of the inadequate nuclear modeling. Much of these differences, however, are associated to the different definition of CCQE used by MiniBooNE and by theorists. Theorist typically term CCQE as an event where one nucleon is knocked out in the final state along with a charged lepton. MiniBooNE on the contrary defines CCQE as an event where one lepton and no pion is observed in the final state, the definition which is now dubbed as 'CCQE-like'. Since then, a number of theoretical models are investigating these issues.

The first ones to point this out was Martini *et al.*, who were able to reproduce MiniBooNE's cross sections with $M_A \sim 1$ GeV by the inclusion of contributions arising from many-particle, many-hole (np-nh) excitations [38]. Those ejected low-energy nucleons are not detected in Mini-BooNE. These processes are not included in a impulse approximation-based approach and was not considered CCQE by theorists, but are now referred to as 'CCQE-like'. In the Martini *et al.* approach, the nuclear ground state is a Fermi gas of non-interacting nucleons characterized by a Fermi momentum (p_f) fixed according to the local density of protons and neutrons (local Fermi gas model). The RPA correlations are introduced through pion exchange, rho exchange and contact Landau-Migdal parameters. The same conjecture was supported by another extensive body of work by Nieves *et al.* [39]. Many aspects of this model are similar to those of Martini *et al.*. They both start with a local Fermi gas model and implement RPA correlations through pion exchange, rho exchange and contact Landau-Migdal parameters. A very different approach to neutrino-nucleus scattering is taken by the SuSA collaboration [40], who employ scaling behavior of the electron scattering data to predict cross sections for neutrino-nucleus scattering. The basic procedure consists of dividing the experimental (e, e') data by an appropriate single-nucleon cross section to obtain the scaling function. The scaling functions determined from (e, e') is extended to neutrino scatterings. A spectral function approach, where nuclear response is modeled using the local density approximation, in which the experimental information obtained from nucleon-knockout measurements is combined with theoretical calculations in nuclear matter at different densities has been employed to neutrino scattering as well [41]. A relativistic Green's function approach is used by the authors of Ref. [42] where the final-state interactions are included by the imaginary part of an optical potential. A semi-phenomenological model, where a density-dependent mean-field potential in which nucleons are bound, is employed in the GiBUU model [43]. A hadronic transport model, for propagation of final-state nucleon in the nucleus, which account for elastic and inelastic collision with the other nucleons is used in GiBUU approach.

Bibliography

[1] J. G. Morfin, J. Nieves, and J. T. Sobczyk, Adv. High Energy Phys. **2012**, 934597 (2012).

[2] Y. Fukuda et al., (Super-Kamiokande Collaboration), Phys. Rev. Lett. **81**, 1562 (1998).

[3] Q. R. Ahmad et al., (SNO Collaboration), Phys. Rev. Lett. **87**, 071301 (2001).

[4] K. Zuber, *Neutrino Physics (second edition)* (CRC Press, 2012).

[5] http://t2k-experiment.org/

[6] A.A. Aguilar-Arevalo et al., (MiniBooNE Collaboration), Phys. Rev. D **81**, 092005 (2010).

[7] A.A. Aguilar-Arevalo et al., (MiniBooNE Collaboration), Phys. Rev. D **88**, 032001 (2013).

[8] K. Abe et al., (T2K Collaboration), Phys. Rev. D**87**, 092003 (2013).

[9] K. Abe et al., (T2K Collaboration), Phys. Rev. D**92**, 112003 (2015).

[10] G.A. Fiorentini et al., (MINERvA Collaboration), Phys. Rev. Lett. **111**, 022502 (2013).

[11] L. Fields et al., (MINERvA Collaboration), Phys. Rev. Lett. **111**, 022501 (2013).

[12] C. Anderson et al., (ArgoNeuT Collaboration), Phys. Rev. Lett. **108**, 161802 (2012).

[13] http://www-nova.fnal.gov/

[14] Y. Nakajima et al., (SciBooNE Collaboration), Phys. Rev. D **83**, 012005 (2011).

[15] P. Adamson et al., (MINOS Collaboration), Phys. Rev. D **77**, 072002 (2008).

[16] P. Astier et al., (NOMAD Collaboration), Nucl. Instrum. Meth. A **515**, 800 (2003).

[17] S. Agostinelli et al., (GEANT4 Collaboration), Nucl. Instrum. Meth. A **506**, 250 (2003).

[18] D. Casper, Nucl. Phys. Proc. Suppl. **112**, 161 (2002).

[19] R. A. Smith, and E. J. Moniz, Nucl. Phys. B **43**, 605 (1972); Nucl. Phys. B **101**, 547 (1975).

[20] D. Rein, and L. M. Sehgal, Ann. Phys. **133**, 79 (1981).

[21] D. Rein, and L. M. Sehgal, Nucl. Phys. B **223**, 29 (1983).

[22] M. Gluck, E. Reya, and A. Vogt, Eur. Phys. J. C **5**, 461 (1998).

[23] A. Bodek, and U. K. Yang, AIP Conf. Proc. 670, 110 (2003).

[24] E. J. Moniz, I. Sick, R. R. Whitney, J. R. Ficenec, R. D. Kephart, and W. P. Trower, Phys. Rev. Lett. **26**, 445 (1971).

[25] G. Battistoni, S. Muraro, P. R. Sala, F. Cerutti, A. Ferrari, S. Roesler, A. Fasso, and J. Ranft, AIP Conf. Proc. **896**, 31 (2007).

[26] A. Ferrari, P. R. Sala, A. Fasso, and J. Ranft, Reports No. CERN-2005-010, SLAC-R-773, INFN-TC-05-11, 2005.

[27] R. Brun, F. Carminati, and S. Giani, Report No. CERN-W5013, 1994.

[28] C. Zeitnitz, and T. A. Gabriel, Nucl. Instrum. Meth. A **349**, 106 (1994).

[29] Y. Hayato, Acta Phys. Polon. B **40**, 2477 (2009).

[30] C. Andreopoulos et al., Nucl. Instrum. Meth. A **614**, 87 (2010).

[31] C. H. Llewellyn Smith, Phys. Rept. **3**, 261 (1972).

[32] A. Bodek, and J. L. Ritchie, Phys. Rev. D **24**, 1400 (1981).

[33] K. Abe et al., (T2K Collaboration), Phys. Rev. Lett. **112**, 181801 (2014).

[34] A. Bodek, I. Park, and U. K. Yang, Nucl. Phy. B **139**, 113 (2005).

[35] K. A. Olive et al., (Particle Data Group), "2014 Review of Particle Physics"(2014).

[36] K. Nakamura et al., "Review of Particle Physics", Journal of Physics G **37** (7A) (2010).

[37] S. Boyd, S. Dytman, E. Hernandez, J. Sobczyk, and R. Tacik, AIP Conf. Proc. **1189**, 60 (2009).

[38] M. Martini, M. Ericson, G. Chanfray, and J. Marteau, Phys. Rev. C **80**, 065501 (2009).

[39] J. Nieves, I. Ruiz Simo, and M.J. Vicente Vacas, Phys. Rev. C **83**, 045501 (2011).

[40] J. E. Amaro, M. B. Barbaro, J. A. Caballero, T. W. Donnelly, C. F. Williamson, Phys. Lett. B **696**, 151 (2011).

[41] O. Benhar, P. Coletti, D. Meloni, Phys. Rev. Lett. **105**, 132301 (2010).

[42] A. Meucci, M. B. Barbaro, J. A. Caballero, C. Giusti, J. M. Udias, Phys. Rev. Lett. **107**, 172501 (2011).

[43] O. Lalakulich, U. Mosel, K. Gallmeister, Phys. Rev. C **86**, 054606 (2012).

"Physics is really nothing more than a search for ultimate simplicity,
but so far all we have is a kind of elegant messiness."

Bill Bryson

2

Formalism

2.1 Quasielastic scattering

In inclusive charged-current quasielastic scattering, an incoming lepton scatters off a target nucleus and a nucleon and a charged lepton appears in the final state. In principle the neutrino-nucleus scattering process is similar to that of electron-nucleus scattering. Since there is a wealth of high-precision data available for electron-nucleus scattering, any model should be tested against electron-nucleus data. Once the model is validated against electron scattering data, it can be extended to describe neutrino scattering off nuclei. In this section, we present a general formalism for the description of cross sections for quasielastic (QE) electron and charged-current (CCQE) neutrino-nucleus scattering.

Let us consider inclusive QE electron and CCQE neutrino scattering off a nucleus, where the details of the final hadron state remain unobserved. As shown in Fig. 2.1(a), an incident electron with four-momentum $(E_i, \vec{k}_i)$ scatters off a nucleus via the exchange of a photon and only the outgoing charged lepton with four-momentum $(E_f, \vec{k}_f)$ is detected in the final state

$$ e(E_i, \vec{k}_i) + A \rightarrow e'(E_f, \vec{k}_f) + X. \tag{2.1} $$

In Fig. 2.1(b), a neutrino with four-momentum $(\varepsilon_i, \vec{\kappa}_i)$ scatters off a nucleus, exchanges a W boson and a charged lepton with four-momentum $(\varepsilon_f, \vec{\kappa}_f)$ is detected in the final state
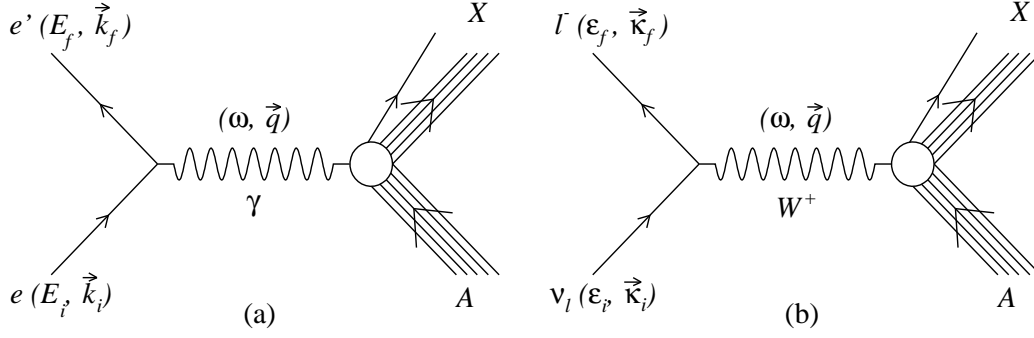
FIGURE 2.1: Inclusive (a) QE electron-nucleus and (b) CCQE neutrino-nucleus ($l = e, \mu, \tau$) scattering. X is the undetected hadronic final state.

$$\nu_l(\varepsilon_i, \vec{\kappa}_i) + A \rightarrow l^-(\varepsilon_f, \vec{\kappa}_f) + X, \tag{2.2}$$

where l represents e, μ, or τ. In both reactions, A is the nucleus in its ground state $|J_i, M_i\rangle$ and X is the unobserved hadronic final state. The transferred energy (ω_e, ω_ν) and momentum ($\vec{q}_e$, $\vec{q}_\nu$) to the nuclear target can be written as:

$$\omega_e = E_i - E_f, \tag{2.3}$$

$$\omega_\nu = \varepsilon_i - \varepsilon_f, \tag{2.4}$$

$$
\begin{aligned}
q_e^2 &= (\vec{k}_i - \vec{k}_f)^2 \tag{2.5} \\
&= E_i^2 + E_f^2 - 2m_e^2 - 2\sqrt{((E_f^2 - m_e^2)(E_i^2 - m_e^2))} \cos\theta, \tag{2.6}
\end{aligned}
$$

$$
\begin{aligned}
q_\nu^2 &= (\vec{\kappa}_i - \vec{\kappa}_f)^2 \tag{2.7} \\
&= \varepsilon_i^2 + \varepsilon_f^2 - m_l^2 - 2\varepsilon_i\varepsilon_f \sqrt{\left(1 - \frac{m_l^2}{\varepsilon_f^2}\right)} \cos\theta, \tag{2.8}
\end{aligned}
$$

where m_e is the electron mass, m_l is the outgoing lepton mass and θ is the lepton scattering angle. The squared transferred four momentum Q^2 is given as

$$Q_{e,\nu}^2 = q_{e,\nu}^2 - \omega_{e,\nu}^2.$$

The double differential cross section for electron and neutrino-nucleus scattering of Eqs. (2.1) and (2.2) can be expressed as

$$\left(\frac{d^2\sigma}{d\omega d\Omega}\right)_e = \frac{\alpha^2}{Q^4}\left(\frac{2}{2J_i+1}\right)E_f k_f \cos^2(\theta/2)$$

$$\times \; \zeta^2\left(Z', E_f, q\right)\left[\sum_{J=0}^{\infty}\sigma_{L,e}^J + \sum_{J=1}^{\infty}\sigma_{T,e}^J\right], \tag{2.9}$$

and

$$\left(\frac{d^2\sigma}{d\omega d\Omega}\right)_\nu = \frac{G_F^2\,\cos^2\theta_c}{(4\pi)^2}\left(\frac{2}{2J_i+1}\right)\varepsilon_f\kappa_f$$

$$\times \; \zeta^2\left(Z', \varepsilon_f, q\right)\left[\sum_{J=0}^{\infty}\sigma_{CL,\nu}^J + \sum_{J=1}^{\infty}\sigma_{T,\nu}^J\right], \tag{2.10}$$

where α is the fine-structure constant, G_F is the Fermi coupling constant, and θ_c is the Cabibbo angle. The direction of the outgoing lepton is described by the solid angle Ω. The function $\zeta(Z', E, q)$ is introduced in order to take into account the distortion of the lepton wave function in the Coulomb field generated by Z' protons. We treat this effect in the modified effective momentum approximation, as will be discussed in the forthcoming chapter.

The $\sigma_{L,e}^J$ (J denotes the multipole number) and $\sigma_{T,e}^J$ are the longitudinal and transverse components of the electron-nucleus scattering cross section, while $\sigma_{CL,\nu}^J$ and $\sigma_{T,\nu}^J$ are the Coulomb-longitudinal and transverse contributions of the neutrino-nucleus scattering cross section. Both, the (Coulomb) longitudinal and transverse part of the cross section are composed of a kinematical factor (v) and a response function (R).

In the electron scattering case, the longitudinal $(\sigma_{L,e}^J)$ and transverse components $(\sigma_{T,e}^J)$ of the cross section can be expressed as follows

$$\sigma_{L,e}^J = v_e^L R_e^L, \tag{2.11}$$

$$\sigma_{T,e}^J = v_e^T R_e^T, \tag{2.12}$$

where the leptonic factors, v_e^L and v_e^T, are given by

$$v_e^L = \frac{Q^4}{|\vec{q}|^4}, \tag{2.13}$$

$$v_e^T = \left[\frac{Q^2}{2|\vec{q}|^2} + \tan^2(\theta/2)\right]. \tag{2.14}$$

Longitudinal R_e^L and transverse R_e^T response functions are defined as

$$R_e^L = |\langle J_f||\widehat{\mathcal{M}}_J^e(|\vec{q}|)||J_i\rangle|^2, \tag{2.15}$$

$$R_e^T = \left[|\langle J_f||\widehat{\mathcal{J}}_J^{mag,e}(|\vec{q}|)||J_i\rangle|^2 + |\langle J_f||\widehat{\mathcal{J}}_J^{el,e}(|\vec{q}|)||J_i\rangle|^2 \right]. \tag{2.16}$$

Here $\widehat{\mathcal{M}}_J^e$, $\widehat{\mathcal{J}}_J^{mag,e}$ and $\widehat{\mathcal{J}}_J^{el,e}$ are the longitudinal, transverse magnetic and transverse electric operators. The $|J_i\rangle$ and $|J_f\rangle$ denote the initial and final state of the nucleus.

Similarly for the neutrino scattering case, we express the Coulomb-longitudinal ($\sigma_{CL,\nu}^J$) and transverse ($\sigma_{T,\nu}^J$) parts of the cross section as follows

$$\sigma_{CL,\nu}^J = \left[v_\nu^{\mathcal{M}} R_\nu^{\mathcal{M}} + v_\nu^{\mathcal{L}} R_\nu^{\mathcal{L}} + 2 \, v_\nu^{\mathcal{ML}} R_\nu^{\mathcal{ML}} \right], \tag{2.17}$$

$$\sigma_{T,\nu}^J = \left[v_\nu^T R_\nu^T \pm 2 \, v_\nu^{TT} R_\nu^{TT} \right], \tag{2.18}$$

where the leptonic coefficients $v_\nu^{\mathcal{M}}$, $v_\nu^{\mathcal{L}}$, $v_\nu^{\mathcal{ML}}$, v_ν^T and v_ν^{TT} are given by

$$v_\nu^{\mathcal{M}} = \left[1 + \frac{\kappa_f}{\varepsilon_f} \cos\theta \right], \tag{2.19}$$

$$v_\nu^{\mathcal{L}} = \left[1 + \frac{\kappa_f}{\varepsilon_f} \cos\theta - \frac{2\varepsilon_i\varepsilon_f}{|\vec{q}|^2} \left(\frac{\kappa_f}{\varepsilon_f} \right)^2 \sin^2\theta \right], \tag{2.20}$$

$$v_\nu^{\mathcal{ML}} = \left[\frac{\omega}{|\vec{q}|} \left(1 + \frac{\kappa_f}{\varepsilon_f} \cos\theta \right) + \frac{m_l^2}{\varepsilon_f|\vec{q}|} \right], \tag{2.21}$$

$$v_\nu^T = \left[1 - \frac{\kappa_f}{\varepsilon_f} \cos\theta + \frac{\varepsilon_i\varepsilon_f}{|\vec{q}|^2} \left(\frac{\kappa_f}{\varepsilon_f} \right)^2 \sin^2\theta \right], \tag{2.22}$$

$$v_\nu^{TT} = \left[\frac{\varepsilon_i + \varepsilon_f}{|\vec{q}|} \left(1 - \frac{\kappa_f}{\varepsilon_f} \cos\theta \right) - \frac{m_l^2}{\varepsilon_f|\vec{q}|} \right], \tag{2.23}$$

and the response functions $R_\nu^{\mathcal{M}}$, $R_\nu^{\mathcal{L}}$, $R_\nu^{\mathcal{ML}}$, R_ν^T and R_ν^{TT} are defined as

$$R_\nu^{\mathcal{M}} = |\langle J_f||\widehat{\mathcal{M}}_J^\nu(|\vec{q}|)||J_i\rangle|^2, \tag{2.24}$$

$$R_\nu^{\mathcal{L}} = |\langle J_f||\widehat{\mathcal{L}}_J^\nu(|\vec{q}|)||J_i\rangle|^2, \tag{2.25}$$

$$R_\nu^{\mathcal{ML}} = \mathcal{R} \left[\langle J_f||\widehat{\mathcal{L}}_J^\nu(|\vec{q}|)||J_i\rangle \langle J_f||\widehat{\mathcal{M}}_J^\nu(|\vec{q}|)||J_i\rangle^* \right], \tag{2.26}$$

$$R_\nu^T = \left[|\langle J_f || \widehat{\mathcal{J}}_J^{mag,\nu}(|\vec{q}|) || J_i \rangle|^2 + |\langle J_f || \widehat{\mathcal{J}}_J^{el,\nu}(|\vec{q}|) || J_i \rangle|^2 \right], \tag{2.27}$$

$$R_\nu^{TT} = \mathcal{R} \left[\langle J_f || \widehat{\mathcal{J}}_J^{mag,\nu}(|\vec{q}|) || J_i \rangle \langle J_f || \widehat{\mathcal{J}}_J^{el,\nu}(|\vec{q}|) || J_i \rangle^* \right]. \tag{2.28}$$

Here $\widehat{\mathcal{M}}_J^\nu$, $\widehat{\mathcal{L}}_J^\nu$, $\widehat{\mathcal{J}}_J^{mag,\nu}$ and $\widehat{\mathcal{J}}_J^{el,\nu}$ are the Coulomb, longitudinal, transverse magnetic and transverse electric operators given as [1–4]

$$\widehat{\mathcal{M}}_{JM}(\kappa) = \int d\vec{x} \, \left[j_J\,(\kappa r)\, Y_J^M\,(\Omega_x) \right] \, \hat{J}_0(\vec{x}) \ , \tag{2.29}$$

$$\widehat{\mathcal{L}}_{JM}(\kappa) = \frac{i}{\kappa} \, \int d\vec{x} \, \left[\vec{\nabla} \left(j_J\,(\kappa r)\, Y_J^M\,(\Omega_x) \right) \right] \, \cdot \, \widehat{\vec{J}}(\vec{x}) \ , \tag{2.30}$$

$$\widehat{\mathcal{J}}_{JM}^{el}(\kappa) = \frac{1}{\kappa} \, \int d\vec{x} \, \left[\vec{\nabla} \, \times \, \left(j_J\,(\kappa r)\, \vec{\mathcal{Y}}_{J,J}^M\,(\Omega_x) \right) \right] \, \cdot \, \widehat{\vec{J}}(\vec{x}) \ , \tag{2.31}$$

$$\widehat{\mathcal{J}}_{JM}^{mag}(\kappa) = \int d\vec{x} \, \left[j_J\,(\kappa r)\, \vec{\mathcal{Y}}_{J,J}^M\,(\Omega_x) \right] \, \cdot \, \widehat{\vec{J}}(\vec{x}) \ . \tag{2.32}$$

Where, $j_J\,(\kappa r)$ denote the spherical Bessel functions of order J, and Y_J^M, $\vec{\mathcal{Y}}_{J,J}^M$ are spherical harmonics. The response functions of Eqs. (2.15), (2.16), and (2.24) - (2.28) contains all nuclear structure information. We calculate these response functions within a continuum random phase approximation formalism, discussed in the following section.

2.2 Continuum random phase approximation

We start the description of a nucleus in a mean-field (MF) approximation, i.e., in our initial picture of the nucleus, the nucleons experience the presence of the others through a mean-field generated by their mutual interaction. We obtain the MF potential and wave functions by solving the Hartree-Fock equations with a Skyrme nucleon-nucleon interaction. Once we have the bound and continuum single-nucleon wave functions, we introduce nuclear long-range correlations in the continuum random phase approximation (CRPA). So, the nucleons which were initially solely under the influence of the MF potential, now additionally interact with each other by means of the two-body SkE2 interaction. In this way, a nucleon interacting with an external field is still able to exchange energy and momentum with the other particles in the nucleus. The model is described in detail in Refs. [1, 5–11].

The CRPA approach [5, 8] describes a nuclear excited state as the linear combination of particle-hole (ph^{-1}) and hole-particle (hp^{-1}) excitations out of a correlated nuclear ground state.

$$|\Psi_{RPA}^C\rangle = \sum_{C'} \left\{ X_{C,C'} \, |p'h'^{-1}\rangle - Y_{C,C'} \, |h'p'^{-1}\rangle \right\}, \tag{2.33}$$

here C denotes a set of quantum numbers representing a reaction channel:

$$C = \{n_h, l_h, j_h, m_h, \varepsilon_h; l_p, j_p, m_p, \tau_z\} \quad . \tag{2.34}$$

p and h represent the quantum numbers related to the particle or hole state, ε_h is the binding-energy of the hole state and τ_z defines the isospin of the particle-hole pair.

The propagation of particle-hole pairs in the nuclear medium is described by the polarization propagator. In the Lehmann representation, this particle-hole Green's function is given by [12]

$$\Pi(x_1, x_2, x_3, x_4; E_x) = \hbar \sum_n \left[\frac{\langle \Psi_0 | \hat{\psi}^\dagger(x_2) \hat{\psi}(x_1) | \Psi_n \rangle \langle \Psi_n | \hat{\psi}^\dagger(x_3) \hat{\psi}(x_4) | \Psi_0 \rangle}{E_x - (E_n - E_o) + i\eta} \right.$$
$$\left. - \frac{\langle \Psi_0 | \hat{\psi}^\dagger(x_3) \hat{\psi}(x_4) | \Psi_n \rangle \langle \Psi_n | \hat{\psi}^\dagger(x_2) \hat{\psi}(x_1) | \Psi_0 \rangle}{E_x + (E_n - E_o) - i\eta} \right] \quad , \tag{2.35}$$

where $|\Psi_0\rangle$ and $|\Psi_n\rangle$ denote the ground and excited state with eigenvalue E_0 and E_n of the many-particle system, respectively. The parameter η is an infinitesimal positive value inserted to deal with the poles in the denominator of the propagator expression. E_x is the excitation energy of the target nucleus and x is the shorthand notation for the combination of the spatial, spin, and isospin coordinates. The field operators $\hat{\psi}(x)$ annihilate a nucleon at a point x. In an RPA-approach, not all the intermediate states $|\Psi_n\rangle$ in expansion (2.35) are considered. Only a limited class of excited states is retained. Contributions are restricted to those excitations where only one-particle one-hole pairs are present.

The CRPA equations are solved using a Green's function approach. The Green's function approach allows one to treat the single-particle energy continuum exactly by solving the RPA equations in coordinate space. The local RPA-polarization propagator is obtained by an iteration to all orders of the first order contribution to the particle-hole Green's function

$$\Pi^{(RPA)}(x_1, x_2; E_x) = \Pi^{(0)}(x_1, x_2; E_x) + \frac{1}{\hbar} \int dx dx' \; \Pi^0(x_1, x; E_x)$$
$$\times \tilde{V}(x, x') \; \Pi^{(RPA)}(x', x_2; E_x) \quad . \tag{2.36}$$

The Π^0 denotes the zeroth-order contribution to the polarization propagator which is equivalent to the HF contribution. The HF responses can be retrieved by switching off the second interaction term in the right hand side of Eq. (2.36). Fig. 2.2 represents different components contributing to the polarization propagator. The first term (a) corresponds to the Π^0 of Eq. (2.36). The second (b) and third term (c) are the first order RPA diagrams while the last term (d) is a higher order RPA diagram, achieved by successive iteration of the first order RPA diagrams. $\tilde{V}$ is the antisymmetrized form of the nucleon-nucleon interaction which we assume to be rotationally invariant, allowing to write $\tilde{V}(x_1, x_2)$ as

$$\tilde{V}(x_1, x_2) = \sum_{\alpha\beta, JM} U_{\alpha\beta}^J(r_1, r_2) \; X_\alpha^{JM\dagger}(\hat{x}_1) \; X_\beta^{JM}(\hat{x}_2) \quad , \tag{2.37}$$
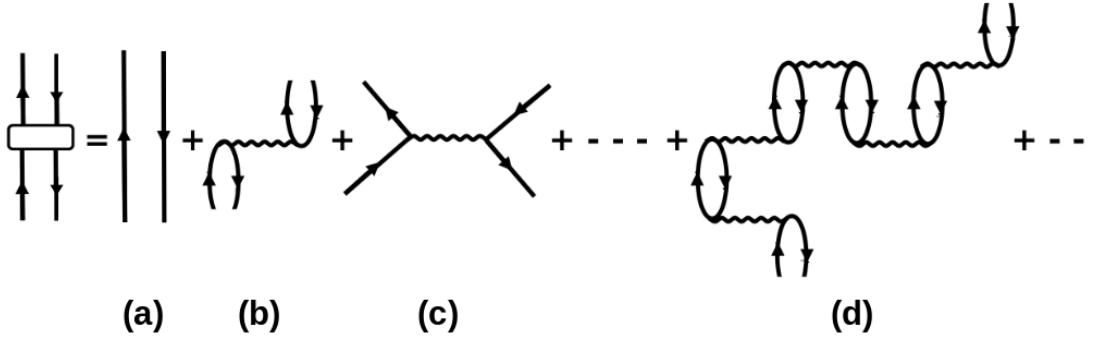
FIGURE 2.2: Diagrammatic representation of the polarization propagator $\Pi^{(RPA)}$ for particle-hole states. Panel (a) corresponds to the unperturbed polarization propagator $\Pi^{(0)}$, (b) and (c) are the first-order direct and exchange RPA diagrams and (d) represents a typical higher-order RPA diagram.

where $X_\gamma^{JM}(\hat{x})$ represents spherical tensor operator of rank J, M and the summation extends over all contributing interaction channels.

From Eqs. (2.33) and (2.36), a solution to the RPA Eq. (2.36) is given by the set of wave functions

$$
\begin{aligned}
|\Psi_C(E)\rangle &= |ph^{-1}(E)\rangle + \int dx_1 \int dx_2 \; \tilde{V}(x_1, x_2) \\
&\times \sum_{C'} \mathcal{P} \int d\varepsilon_{p'} \; \langle \Psi_o | \hat{\psi}^\dagger(x_2)\hat{\psi}(x_2) | \Psi_C(E)\rangle \\
&\times \left[\frac{\psi_{h'}(x_1)\psi_{p'}^\dagger(x_1, \varepsilon_{p'})}{E - \varepsilon_{p'h'}} |p'h'^{-1}(\varepsilon_{p'h'})\rangle - \frac{\psi_{h'}^\dagger(x_1)\psi_{p'}(x_1, \varepsilon_{p'})}{E + \varepsilon_{p'h'}} |h'p'^{-1}(-\varepsilon_{p'h'})\rangle \right],
\end{aligned}
\tag{2.38}
$$

where $\mathcal{P}$ denotes the Cauchy principle value, $|ph^{-1}(E)\rangle$ and $|hp^{-1}(-E)\rangle$ are the unperturbed particle-hole and hole-particle solutions of the mean field problem. In Eq. (2.38), the notation $\varepsilon_{ph} = \varepsilon_p - \varepsilon_h$ is used. The summation is restricted to the open channels $\varepsilon_p - \varepsilon_h > 0$. Furthermore, the wave functions of Eq. (2.38) are of the standard form of Eq. (2.33) with

$$
\begin{aligned}
X_{C,C'}(E, \varepsilon_{p'}) &= \delta_{C,C'} \; \delta(E - \varepsilon_{p'h'}) + \mathcal{P} \int dx_1 \int dx_2 \; \tilde{V}(x_1, x_2) \\
&\times \frac{\psi_{h'}(x_1)\psi_{p'}^\dagger(x_1, \varepsilon_{p'})}{E - \varepsilon_{p'h'}} \langle \Psi_o | \hat{\psi}^\dagger(x_2)\hat{\psi}(x_2) | \Psi_C(E)\rangle,
\end{aligned}
\tag{2.39}
$$

and

$$
\begin{aligned}
Y_{C,C'}(E, \varepsilon_{p'}) &= \int dx_1 \int dx_2 \; \tilde{V}(x_1, x_2) \\
&\times \frac{\psi_{h'}^\dagger(x_1)\psi_{p'}(x_1, \varepsilon_{p'})}{E + \varepsilon_{p'h'}} \langle \Psi_o | \hat{\psi}^\dagger(x_2)\hat{\psi}(x_2) | \Psi_C(E)\rangle.
\end{aligned}
\tag{2.40}
$$

The first part of second term in Eq. (2.38) corresponds to the Tamm-Dancoff approximation (TDA) and the second one represents the negative energy RPA contribution. From the energy

dependence of the denominators, it is clear that the first term will dominantly contribute to the total wave function. The backward RPA contribution becomes only important for states whose energy eigenvalue deviates substantially from the unperturbed value ε_{ph}. This makes RPA a well-suited tool for describing collective excitations in nuclei.

In the angular-momentum coupled form, the RPA wave functions read as

$$|\Psi_C(JM; E)\rangle = \sum_{m_h, m_p} (-1)^{j_h - m_h} \langle j_h \ -m_h \ j_p m_p | JM \rangle |\Psi_C(E)\rangle, \qquad (2.41)$$

where C now represents a reaction channel in the coupled scheme:

$$C = \{n_h, l_h, j_h, m_h, \varepsilon_h; l_p, j_p, m_p, \tau_z\}_{JM}. \qquad (2.42)$$

From the wave function (Eq. 2.41) the correctly normalized solutions of the scattering problem can be obtained by taking suitable linear combinations. Defining the K matrix by

$$
\begin{aligned}
K_{C,C'}^J \ &= \ \frac{(-1)}{2J+1} \sum_{\alpha\beta} \int dr_1 \int dr_2 U_{\alpha\beta}^J(r_1, r_2) \\
&\times \ \langle h' || X_\alpha^J(x_1) || p'(E + \varepsilon_{h'}) \rangle_{r_1}^* \\
&\times \ \langle \Psi_0 || X_\beta^J(x_1) || \Psi_C(J; E) \rangle_{r_2} \ ,
\end{aligned}
\qquad (2.43)
$$

where the subscript r of the transition densities denotes that all coordinates except the radial one have been integrated, it can be shown that the wave functions constructed by putting

$$|\Psi_C^+(JM; E)\rangle = \sum_{C'_{open}: \varepsilon_p = \varepsilon_h + E > 0} \left[1 + i\pi K^J \right]_{C,C'}^{-1} |\Psi_{C'}(JM; E)\rangle, \qquad (2.44)$$

contain asymptotically only one incoming wave. They allow us to describe systems where one particle is excited to an unbound state with $\varepsilon_p > 0$, and is able to escape from the nuclear potential. Furthermore they obey the same normalization conditions as the unperturbed $|ph^{-1}\rangle$ wave functions. The wave functions (Eq. 2.44) will be used to evaluate the transition densities in the cross section.

Defining the unperturbed radial response functions as

$$
\begin{aligned}
\int dr \int dr' R_{\eta\mu}^{(0)JM}(r, r'; E) \ &= \ \frac{1}{\hbar} \int dx \int dx' X_\eta^{JM}(x) \\
&\times \ \Pi^{(0)}(x, x'; \omega) X_{\eta'}^{JM\dagger}(x') \ ,
\end{aligned}
\qquad (2.45)
$$

the RPA transition densities are determined by a set of coupled integral equations

$$
\begin{aligned}
\langle \Psi_0 || X_\eta^J || \Psi_C(J; E) \rangle_r \ &= \ -\langle h || X_\eta^J || p(\varepsilon_{ph}) \rangle_r \\
&+ \sum_{\mu,\nu} \int dr_1 \int dr_2 \ U_J^{\mu\nu}(r_1, r_2) \mathcal{R} \left(R_{\eta\mu}^{(0)J}(r, r_1; E) \right) \\
&\times \ \langle \Psi_0 || X_\nu^J || \Psi_C(J; E) \rangle_{r_2}.
\end{aligned}
\qquad (2.46)
$$

Discretizing these equations on a mesh in the radial coordinate, the transition densities for each reaction channel (Eq. 2.46) are obtained as the solution of the matrix equation

$$\rho_C^{RPA} = -\frac{1}{1 - RU} \ \rho_C^{HF}.$$ (2.47)

Here ρ^{RPA} and ρ^{HF} represent column vectors containing the RPA and the Hartree-Fock transition densities for all included interaction channels η and for a number of mesh points in coordinate space. The R and U are block matrices containing the unperturbed response functions (Eq. 2.45) and the radial part of the interaction, evaluated at the appropriate channels and r values. The discretization in coordinate space is well under control. It does not demand large numbers of mesh points for the calculated transition densities to become mesh independent, thus keeping the dimension of matrix inversions to be performed sufficiently small. From the form of Eq. (2.47) it is clear that the wave functions (Eq. 2.38) can be considered as the solution to the RPA equivalent of the Lippmann-Schwinger integral scattering equations. In Eq. (2.47) as well as in Eq. (2.46), the minus sign arises from the phase convention adopted in the definition of the K matrix (2.43). This formalism has the interesting feature that treating the RPA equations in coordinate space allows us to deal with the energy continuum in an exact way, without cutoff or discretization of the excitation energies.

2.3 Skyrme interaction

The HF and CRPA calculations are performed using the SkE2 parameterization [7, 13]. This parameter set was designed to yield a realistic description of nuclear structure properties in both particle-particle and particle-hole channels over the whole mass table. This is achieved by replacing the three-particle contribution by a momentum-dependent two-body term. The extra obtained free parameter is used to guarantee correct two-body characteristics in nuclei containing few valence nucleons outside of the closed shells. Furthermore, the SkE2 parameter set allows a good reproduction of the experimental single-particle energies.

Skyrme's interaction, in its original form, is written as

$$V \ = \ \sum_{i<j} V_{ij} \ + \ \sum_{i<j<k} V_{ijk} \ ,$$ (2.48)

with a two body part V_{ij} and three-body part V_{ijk}. The two body interaction matrix element in momentum space is expressed as

$$\begin{aligned} \langle \vec{k} | V_{12} | \vec{k'} \rangle \ &= \ t_0 \ (1 + x_0 P_\sigma) \ + \ \frac{1}{2} t_1 (k^2 + k'^2) + t_2 \vec{k} \cdot \vec{k'} \\ &\quad + \ i W_0 (\vec{\sigma}_1 + \vec{\sigma}_2) \cdot \vec{k} \times \vec{k'} \ , \end{aligned}$$ (2.49)

where $\vec{k}$, $\vec{k'}$ are relative wave vectors of two nucleons and P_σ is a spin-exchange operator where $\vec{\sigma}$ are Pauli spin matrices. In configuration space Eq. (2.49) can be written as

$$
\begin{aligned}
V_{12} &= t_0 \left(1 + x_0 \hat{P}_\sigma\right) \delta(\vec{r}_1 - \vec{r}_2) \\
&\quad - \frac{1}{8} t_1 \left[(\overleftarrow{\nabla}_1 - \overleftarrow{\nabla}_2)^2 \, \delta(\vec{r}_1 - \vec{r}_2) + \delta(\vec{r}_1 - \vec{r}_2)\,(\overrightarrow{\nabla}_1 - \overrightarrow{\nabla}_2)^2 \right] \\
&\quad + \frac{1}{4} t_2 (\overleftarrow{\nabla}_1 - \overleftarrow{\nabla}_2)\,\delta(\vec{r}_1 - \vec{r}_2)\,(\overrightarrow{\nabla}_1 - \overrightarrow{\nabla}_2) \\
&\quad + i W_0 \, (\vec{\sigma}_1 + \vec{\sigma}_2)\cdot(\overleftarrow{\nabla}_1 - \overleftarrow{\nabla}_2) \times \delta(\vec{r}_1 - \vec{r}_2)\,(\overrightarrow{\nabla}_1 - \overrightarrow{\nabla}_2) \,,
\end{aligned}
\tag{2.50}
$$

where $\vec{k}$ denotes the operator $(\overrightarrow{\nabla}_1 - \overrightarrow{\nabla}_2)/2i$ acting to the right and $\vec{k'}$ is the operator $-(\overleftarrow{\nabla}_1 - \overleftarrow{\nabla}_2)/2i$ acting to the left.

For the three-body part in Eq. (2.48), a zero-range force can be written as

$$
V_{123}^{(a)} = t_3 \, \delta(\vec{r}_1 - \vec{r}_2)\,\delta(\vec{r}_1 - \vec{r}_3) \,,
\tag{2.51}
$$

and for the Hartree-Fock calculations of even-even nuclei, this force is equivalent to a two-body density-dependent interaction

$$
V_{12}^{(a)} = \frac{1}{6}\, t_3 \, (1 + \hat{P}_\sigma)\, \rho \left(\frac{\vec{r}_1 + \vec{r}_2}{2} \right) \delta(\vec{r}_1 - \vec{r}_2) \,.
\tag{2.52}
$$

In the extended Skyrme interaction, the SkE interaction, only a fraction $(1 - x_3)$ of the three-body force (Eq. 2.51) is replaced by the density-dependent two-body force (Eq. 2.52). The advantage of such a partition is that the Hartree-Fock equations become independent of the fraction parameter x_3 in time-reversal invariant nuclear system and both forces (Eq. 2.51, 2.52) yield equivalent contributions to the Hamiltonian density.

A further extension of the Skyrme interaction, the SkE2 interaction, consists of adding a momentum dependent zero-range three-body part

$$
\begin{aligned}
V_{123}^{(b)} &= \frac{1}{6}\, t_4 \, [(\vec{k'}_{12}^2 + \vec{k'}_{23}^2 + \vec{k'}_{31}^2) \\
&\quad + (\vec{k}_{12}^2 + \vec{k}_{23}^2 + \vec{k}_{31}^2)] \,,
\end{aligned}
\tag{2.53}
$$

to the conventional Skyrme three-body part (Eq. 2.51). In configuration space, Eq. (2.53) can be expressed as

$$
\begin{aligned}
V_{123}^{(b)} &= -\frac{1}{24}\, t_4 \left\{ \left[(\overleftarrow{\nabla}_1 - \overleftarrow{\nabla}_2)^2 + (\overleftarrow{\nabla}_2 - \overleftarrow{\nabla}_3)^2 + (\overleftarrow{\nabla}_3 - \overleftarrow{\nabla}_1)^2 \right] \right\} \\
&\quad \times \ \delta(\vec{r}_1 - \vec{r}_2)\,\delta(\vec{r}_1 - \vec{r}_3) + \ \delta(\vec{r}_1 - \vec{r}_2)\,\delta(\vec{r}_1 - \vec{r}_3) \\
&\quad \times \ \left\{ \left[(\overrightarrow{\nabla}_1 - \overrightarrow{\nabla}_2)^2 + (\overrightarrow{\nabla}_2 - \overrightarrow{\nabla}_3)^2 + (\overrightarrow{\nabla}_3 - \overleftarrow{\nabla}_1)^2 \right] \right\}.
\end{aligned}
\tag{2.54}
$$

So, the antisymmetrized SkE2 interaction, in coordinate space, adapts the form

$$
\begin{aligned}
V(\vec{r_1}, \vec{r_2}) \;=\;& t_0\,(1 + x_0 \hat{P}_\sigma)\,\delta(\vec{r_1} - \vec{r_2}) \\
& - \frac{1}{8} t_1 \left[(\overleftarrow{\nabla}_1 - \overleftarrow{\nabla}_2)^2\,\delta(\vec{r_1} - \vec{r_2}) + \delta(\vec{r_1} - \vec{r_2})\,(\overrightarrow{\nabla}_1 - \overrightarrow{\nabla}_2)^2 \right] \\
& + \frac{1}{4} t_2 (\overleftarrow{\nabla}_1 - \overleftarrow{\nabla}_2)\,\delta(\vec{r_1} - \vec{r_2})\,(\overrightarrow{\nabla}_1 - \overrightarrow{\nabla}_2) \\
& + i W_0\,(\vec{\sigma}_1 + \vec{\sigma}_2) \cdot (\overleftarrow{\nabla}_1 - \overleftarrow{\nabla}_2) \times \delta(\vec{r_1} - \vec{r_2})\,(\overrightarrow{\nabla}_1 - \overrightarrow{\nabla}_2) \\
& + \frac{1}{6} t_3\,(1 - x_3)\,(1 + \hat{P}_\sigma)\,\rho\,\frac{(\vec{r_1} + \vec{r_2})}{2}\,\delta(\vec{r_1} - \vec{r_2}) \\
& + \frac{e^2}{|\vec{r_1} - \vec{r_2}|} \;+\; x_3 t_3\,\delta(\vec{r_1} - \vec{r_2})\,\delta(\vec{r_1} - \vec{r_3}) \\
& - \frac{1}{24} t_4 \left\{ \left[(\overleftarrow{\nabla}_1 - \overleftarrow{\nabla}_2)^2 + (\overleftarrow{\nabla}_2 - \overleftarrow{\nabla}_3)^2 + (\overleftarrow{\nabla}_3 - \overleftarrow{\nabla}_1)^2 \right] \right\} \\
& \qquad \delta(\vec{r_1} - \vec{r_2})\,\delta(\vec{r_1} - \vec{r_3}) + \delta(\vec{r_1} - \vec{r_2})\,\delta(\vec{r_1} - \vec{r_3}) \\
& \qquad \left\{ \left[(\overrightarrow{\nabla}_1 - \overrightarrow{\nabla}_2)^2 + (\overrightarrow{\nabla}_2 - \overrightarrow{\nabla}_3)^2 + (\overrightarrow{\nabla}_3 - \overleftarrow{\nabla}_1)^2 \right] \right\}.
\end{aligned}
\tag{2.55}
$$

In the calculation of the transition densities, only the most important channels resulting from (2.55) are taken into account. For natural parity transitions these are

$$
Y_J,\, [Y_J \otimes \vec{\sigma}]_J,\, \left[Y_{J\pm1} \otimes (\overrightarrow{\nabla} \pm \overleftarrow{\nabla}) \right]_J,\, \left[Y_J \otimes (\overrightarrow{\nabla^2} + \overleftarrow{\nabla^2}) \right]_J.
\tag{2.56}
$$

For unnatural parity transitions, the dominant channels are

$$
\begin{aligned}
& [Y_{J\pm1} \otimes \vec{\sigma}]_J,\, \left[Y_J \otimes (\overrightarrow{\nabla} \pm \overleftarrow{\nabla}) \right]_J,\, \left[[Y_J \otimes (\overrightarrow{\nabla} - \overleftarrow{\nabla})]_J \otimes \vec{\sigma} \right]_J, \\
& \left[[Y_J \otimes (\overrightarrow{\nabla} - \overleftarrow{\nabla})]_{J\pm1} \otimes \vec{\sigma} \right]_J,\, \left[[Y_{J\pm1} \otimes (\overrightarrow{\nabla^2} - \overleftarrow{\nabla^2})]_J \otimes \vec{\sigma} \right]_J.
\end{aligned}
\tag{2.57}
$$

All operators can be combined with the isospin operators 1 and $\vec{\tau}$. As the same SkE2 interaction with the same parameter values is used for the calculation of the unperturbed as well as the RPA wave-functions, the formalism is self-consistent with respect to the residual interaction used.

An alternative approach is the use of a Landau-Migdal particle-hole interaction, which has the form

$$
V(r) = C_0 \left\{ f_0(\rho) \;+\; f_0^{'}(\rho)\,(\tau_1.\tau_2) \;+\; g_0\,(\sigma_1.\sigma_2) \;+\; g_0^{'}(\sigma_1.\sigma_2)(\tau_1.\tau_2) \right\},
\tag{2.58}
$$

where a density dependence is introduced through the parameterization

$$
f(\rho(r)) = (1 - \rho(r))\,f^{ext} \;+\; \rho(r)\,f^{int}.
\tag{2.59}
$$

The density has the familiar form

$$
\rho(r) \;=\; \frac{1}{1 + e^{\frac{r-R}{a}}}.
\tag{2.60}
$$

The parameter set for Landau-Migdal interaction is taken from Ref. [14].

2.4 Other approximations

There are a number of additional approximations that made the CRPA formalism more realistic. Some of them (e.g., relativistic correction, modified effective momentum approximation, regularization of the nucleon-nucleon interaction) are added to adapt the formalism to intermediate energies (since the CRPA formalism was originally developed to describe the low-energy nuclear scatterings). And other (folding procedure) to improve the description of the giant resonance region. We briefly describe all these approximations in this section.

(a) Folding procedure

Low energy (few 10s of MeV) projectiles can excite the nucleus above the nucleon emission threshold, in the giant resonance region. The CRPA approach is used to describe the excitation of the nuclear giant resonances. However, a limitation of the RPA formalism is that the configuration space is restricted to 1p-1h excitations. As a result, only the escape-width contribution to the final-state interaction is accounted for and the spreading width of the particle states is neglected. This affects the description of giant resonances in the CRPA formalism. In comparison with experimental data, the energy location of the giant resonance is generally well predicted but its width is underestimated, and the height of the response in the peak is overestimated. This limitation is not related to the choice of different input (wave functions, residual interactions, etc.) but is due to some intrinsic approximations connected to the RPA theory [15]. These problems can be solved by extending the CRPA configuration space beyond elementary excitations of the 1p-1h type. As an effective method, effects beyond CRPA such as final state interactions (FSI) to allow for the re-interaction of the emitted nucleon with the residual nucleus, in terms of a folding procedure [15–18], is often used.

We use a similar phenomenological approach where the modified response functions $R'(q, \omega')$ are obtained after folding the HF and CRPA response functions $R(q, \omega)$:

$$R'(q, \omega') = \int_{-\infty}^{\infty} d\omega \ R(q, \omega) \ L(\omega, \omega'), \tag{2.61}$$

with L a Lorentzian

$$L(\omega, \omega') = \frac{1}{2\pi} \left[\frac{\Gamma}{(\omega - \omega')^2 + (\Gamma/2)^2} \right]. \tag{2.62}$$

We use an effective value of $\Gamma = 3$ MeV which complies well with the predicted energy width in the giant-resonance region [16], where one expects the effect of the folding to be most important. The overall effect of folding is a redistribution of strength from peak to tails. In line with the conclusions drawn in Refs. [15, 19], the energy-integrated response functions are not much affected by the folding procedure of Eq. (2.61).

(b) Semi-relativistic correction

Our description of the nuclear dynamics is based on a nonrelativistic framework because it was originally developed to describe the low-energy nuclear physics where relativistic effects are negligible. One of the challenges in extending the nonrelativistic model to intermediate energies, is to account for relativistic effects. For $q > 500$ MeV/c, the momentum of the emitted nucleon is comparable with its rest mass, and relativistic effects become important. We have implemented relativistic corrections in an effective fashion, as suggested in Refs. [18, 20, 27]. Those references show that a satisfactory description of relativistic effects can be achieved by the following kinematic substitution in the nuclear response

$$\lambda \rightarrow \lambda \left(1 + \lambda \right), \tag{2.63}$$

where $\lambda = \omega / 2 M_N$ and M_N is the nucleon mass. This modification is used only for the calculations of responses and not in the nucleon form factors because the energy and momentum transfers remain ω and q. This substitution is only meant to adapt the momentum of the ejected nucleon by using the relativistic energy-momentum relation. It effectively changes squared three-momentum transfers (q^2) into squared four-momentum transfers (Q^2), resulting in a shift of the QE peak from $\omega = q^2 / 2 M_N$ to $\omega = Q^2 / 2 M_N$. The overall effect on the cross section is a reduction of the width of the one-body responses and a shift of the QE peak towards smaller values of ω. The correction becomes sizable for $q \gtrsim 500$ MeV/c.

(c) Regularization of the nucleon-nucleon interaction

As we mentioned before, our CRPA approach is self-consistent with respect to the nucleon-nucleon interaction, because we use the same SkE2 interaction in solving the HF as well as CRPA equations. The parameters of the momentum-dependent SkE2 force are optimized against ground-state and low-excitation energy properties of spherical nuclei [13]. Under those conditions the virtuality Q^2 of the nucleon-nucleon vertices is small. At high virtualities Q^2, the SkE2 force tends to be unrealistically strong. We remedy this by introducing a dipole hadronic form factor at the nucleon-nucleon interaction vertices

$$V(Q^2) \rightarrow V(Q^2 = 0) \frac{1}{(1 + \frac{Q^2}{\Lambda^2})^2} , \tag{2.64}$$

where we introduced the free cut-off parameter Λ. We adopt $\Lambda = 455$ MeV, a value which is optimized in a χ^2 test within global maximum of 'goodness of fit' criteria, in the comparison of $A(e, e')$ CRPA cross sections with the almost all available experimental data of Refs. [22–29]. In the χ^2 test, we consider the theory-experiment comparison from low values of omega up to the maximum of the quasielastic peak. We have restricted our fit to the low-ω side of the quasielastic peak, because the high-ω side is subject to corrections stemming from meson-exchange currents, multinucleon emissions and Δ excitations, which are not included in our model.

(d) Modified effective momentum approximation

In order to take into account the influence of the Coulomb field of nucleus on the outgoing lepton, Fermi function is often employed in the calculations. The Fermi function, taken as the ratio of the Coulomb wave to free s-wave evaluated at the origin, works well only for low energy processes such as beta decay where only s-wave contributes to the process. At higher energies, the Fermi function does not work well even for electrons. However, an effective momentum approximation (EMA) can be used when the outgoing lepton is an electron. EMA typically consists of shortening the lepton wavelength resulting in a larger effective momentum transfer

$$q_{eff} \; = \; q + 1.5 \; \left(\frac{Z'\alpha\hbar c}{R} \right), \tag{2.65}$$

where $R = 1.24 \; A^{1/3}$ fm, and rescaling the amplitude of wave function by q_{eff}/q. EMA does not take into account the effect of the mass of the lepton. For the massive lepton case, such as for a muon, a modified effective momentum approximation (MEMA) seems to work well [30]. MEMA suggests that beside shortening the wavelength in the matrix element, the phase factor qE in cross section can be replaced by $q_{eff}E_{eff}$. So, the lepton wave functions in the density of final state are modified accordingly

$$\Psi_l^{eff} \; = \; \zeta(Z', E, q) \; \Psi_l \,, \tag{2.66}$$

with

$$\zeta(Z', E, q) \; = \; \sqrt{\frac{q_{eff}E_{eff}}{qE}}, \tag{2.67}$$

where E (E_{eff}) is the energy (effective-energy) of the outgoing lepton. So the rescaling of amplitude becomes $\sqrt{q_{eff}E_{eff}/qE}$ instead of $\sqrt{q_{eff}/q}$.

Bibliography

[1] N. Jachowicz, S. Rombouts, K. Heyde, and J. Ryckebusch, Phys. Rev. C**59**, 3246 (1999).

[2] J. D. Walecka, *Theoretical Nuclear and Subnuclear Physics* (Oxford University Press, New York, 1995).

[3] J. D. Walecka, in Muon Physics, Vol. 2, edited by V. W. Hughes, and C. S. Wu (Academic Press, New York, 1975).

[4] J. S. O' Connell, T. W. Donnelly, and J. D. Walecka, Phys. Rev. C **6**, 719 (1972).

[5] J. Ryckebusch, *Photon and electron-induced one-nucleon emission wintin a selfconsistent HF-RPA model*, PhD-thesis, Ghent University (1988).

[6] J. Ryckebusch, M. Waroquier, K. Heyde, J. Moreau, and D. Ryckbosch, Nucl. Phys. A**476**, 237 (1988).

[7] J. Ryckebusch, K. Heyde, D. Van Neck, and M. Waroquier, Nucl. Phys. A**503**, 694 (1989).

[8] N. Jachowicz, *Many-body description of neutrino-nucleus interactions*, PhD-thesis, Ghent University (2000).

[9] N. Jachowicz, K. Heyde, J. Ryckebusch, and S. Rombouts, Phys. Rev. C**65**, 025501 (2002).

[10] V. Pandey, N. Jachowicz, J. Ryckebusch, T. Van Cuyck, and W. Cosyn, Phys. Rev. C**89**, 024601 (2014).

[11] V. Pandey, N. Jachowicz, T. Van Cuyck, J. Ryckebusch, and M. Martini, Phys. Rev. C**92** (2), 024606 (2015) .

[12] A. L. Fetter, and J. D. Walecka, *Quantum Theory of Many-Particle Systems* (McGraw-Hill Book Company, New York, 1971).

[13] M. Waroquier, J. Ryckebusch, J. Moreau, K. Heyde, N. Blasi, S.Y. van de Werf, and G. Wenes, Phys. Rep. **148**, 249 (1987).

[14] G. Co', and S. Krewald, Phys. Lett. 137 B, 145 (1984).

[15] A. Botrugno, and G. Co', Nucl. Phys. **A761**, 200 (2005).

[16] R. D. Smith, J. Wambach, Phys. Rev. C**38**, 100 (1988).

[17] A. De Pace, and M. Viviani, Phys. Rev. C**48**, 2931 (1993).

[18] J. E. Amaro, M. B. Barbaro, J. A. Caballero, T. W. Donnelly, and J. M. Udias, Phys. Rev. C**75**, 034613 (2007).

[19] A. Gil, J. Nieves, and E. Oset, Nucl. Phys. A **627**, 543 (1997).

[20] S. Jeschonnek, T. W. Donnelly, Phys. Rev. C**57**, 2438 (1998).

[21] J. E. Amaro, M. B. Barbaro, J. A. Caballero, T. W. Donnelly, and C. Maieron, Phys. Rev. C**71**, 065501 (2005).

[22] P. Barreau *et al.*, Nucl. Phys. A**402**, 515 (1983).

[23] J. S. O'Connell *et al.*, Phys. Rev. C**35**, 1063 (1987).

[24] R. M. Sealock *et al.*, Phys. Rev. Lett.**62**, 1350 (1989).

[25] D. S. Bagdasaryan *et al.*, YERPHI-1077-40-88 (1988).

[26] D. B. Day *et al.*, Phys. Rev. C **48**, 1849 (1993).

[27] D. Zeller, DESY-F23-73-2 (1973).

[28] M. Anghinolfi *et al.*, Nucl. Phys. A**602**, 405 (1996).

[29] C. F. Williamson*et al.*, Phys. Rev. C**56**, 3152 (1997).

[30] J. Engel, Phys. Rev. C**57**, 2004 (1998).

"It doesn't matter how beautiful your theory is, it doesn't matter how smart you are. If it doesn't agree with experiment, it's wrong."

Richard P. Feynman

3

Results and Discussion

The search for the measurement of neutrino-oscillation parameters is moving into a precision era. There has been an enormous enhancement in the experimental activities in recent years, but experiments also face a number of challenges related to systematic uncertainties. The major uncertainties are related to the underlying neutrino-nucleus signal in the detector. As discussed in Chapter 1, the neutrinos are generated as secondary decay products and the incident neutrino energy is not known. The neutrino energy is reconstructed based on the calorimetric information and the kinematics of the leptons detected in the final state. This results in neutrino energies distributed over a wide range. Hence, a number of nuclear interaction mechanisms over a broad kinematic range (from low-energy nuclear excitation, quasielastic scattering, multinucleon emission to deep inelastic scattering) simultaneously come into play. The Monte-Carlo generators used in the analysis of the experiments are based mainly on the relativistic Fermi gas based models which can describe the general behavior of the QE cross section sufficiently accurately. But its description becomes poor for smaller momentum transfers, where nuclear effects are more prominent. The inadequacy of RFG in describing nuclear effects results into high systematic uncertainties. In order to minimize systematic errors, one needs microscopic nuclear structure models which can describe cross sections over the broad energy range active in these experiments.

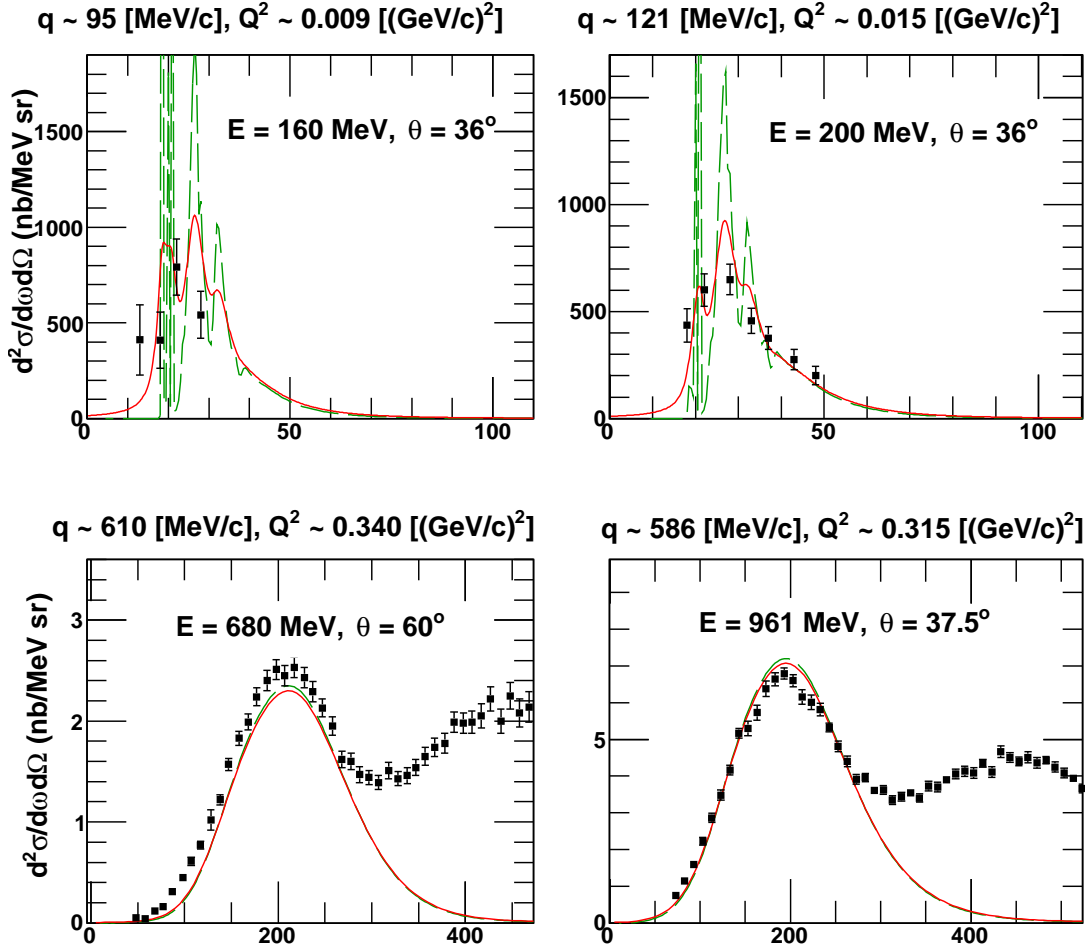We start this chapter by presenting results of several extensions that we added in our CRPA formalism.

FIGURE 3.1: Comparison of ^{12}C(e, e') cross sections obtained with (full line) and without (dashed lines) the folding method. The experimental data are from Refs. [1, 2]. The q and Q^2 values are evaluated at the quasielastic peak. E denotes the incident energy and θ the lepton scattering angle.

(a) Folding procedure

We start with the extension used to improve the model at low energies. The CRPA formalism describes the position of giant resonances well enough, but underpredicts their width and over-predicts their height, as one can observe in the dashed curve in Fig. 3.1. This limitation is due to the fact that the configuration space in the RPA formalism is restricted to 1p-1h excitations and hence only the escape-width contribution to the final-state interactions is accounted for, while the spreading width of the particle states is neglected. Several effective methods are proposed in Refs. [3–6] to remedy this shortcoming. We used a simplified folding procedure (Eq. (2.61)) where we fold HF and CRPA response functions with a Lorentzian using an effective value for the energy width, $\Gamma = 3$ MeV. The results are shown in Fig. 3.1, where we compare the (e, e') cross sections obtained with and without folding procedure. Top panels clearly show that in the giant-resonance region, the adopted folding procedure spreads the strength over a broader ω range, thereby considerably improving the quality of agreement with the data. The energy-integrated cross section remains unaffected. At higher ω (bottom panels) the effect of the folding
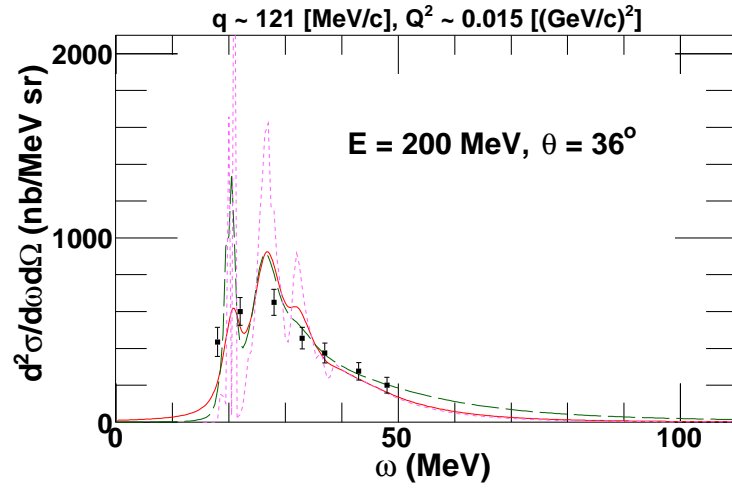
FIGURE 3.2: Comparison of ^{12}C(e, e') CRPA cross sections with the data from Ref. [1]. The short-dashed line is the bare CRPA result. The other two curves have been folded to correct for the missing spreading width. The long-dashed line uses the procedure suggested by Smith and Wambach [3] and the full line show results where response functions were folded with a Lorentzian with $\Gamma = 3$ MeV.
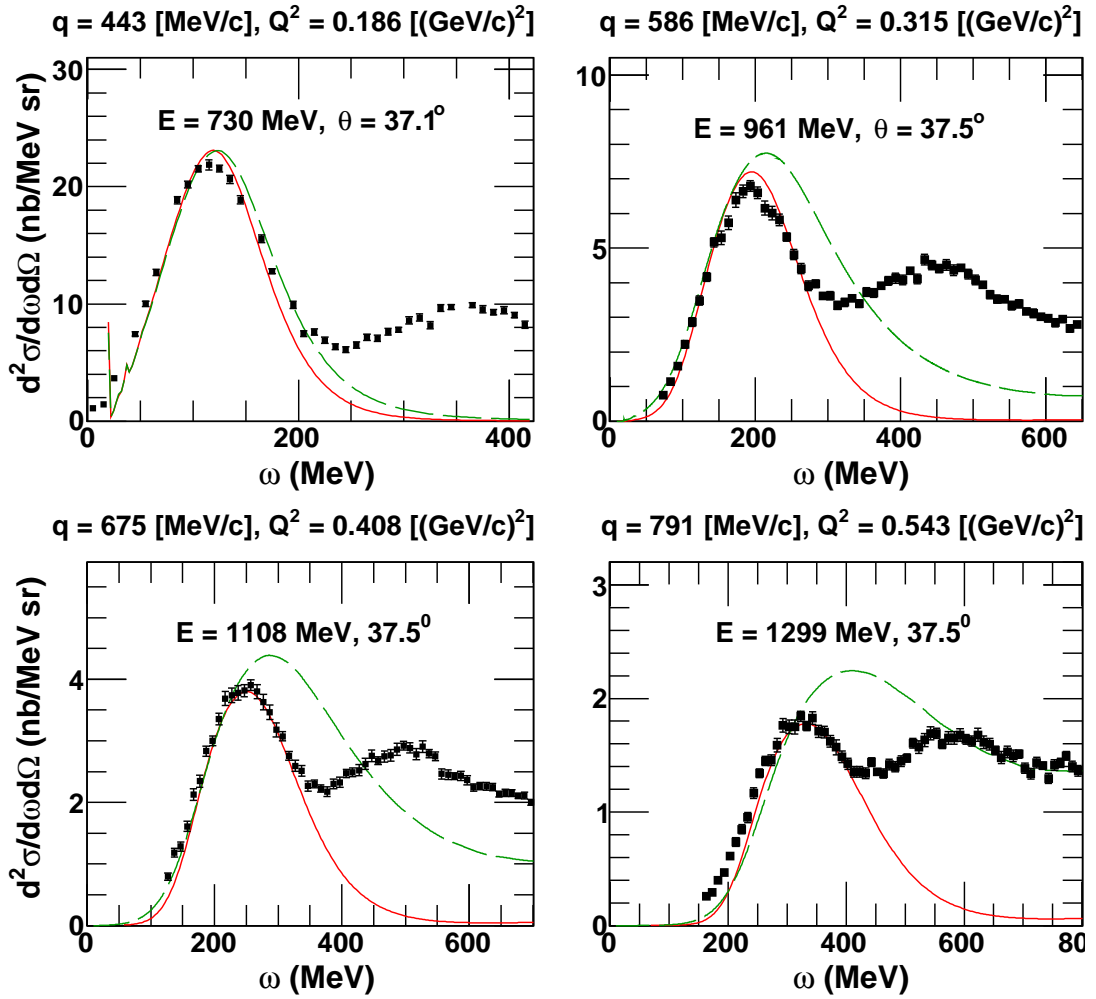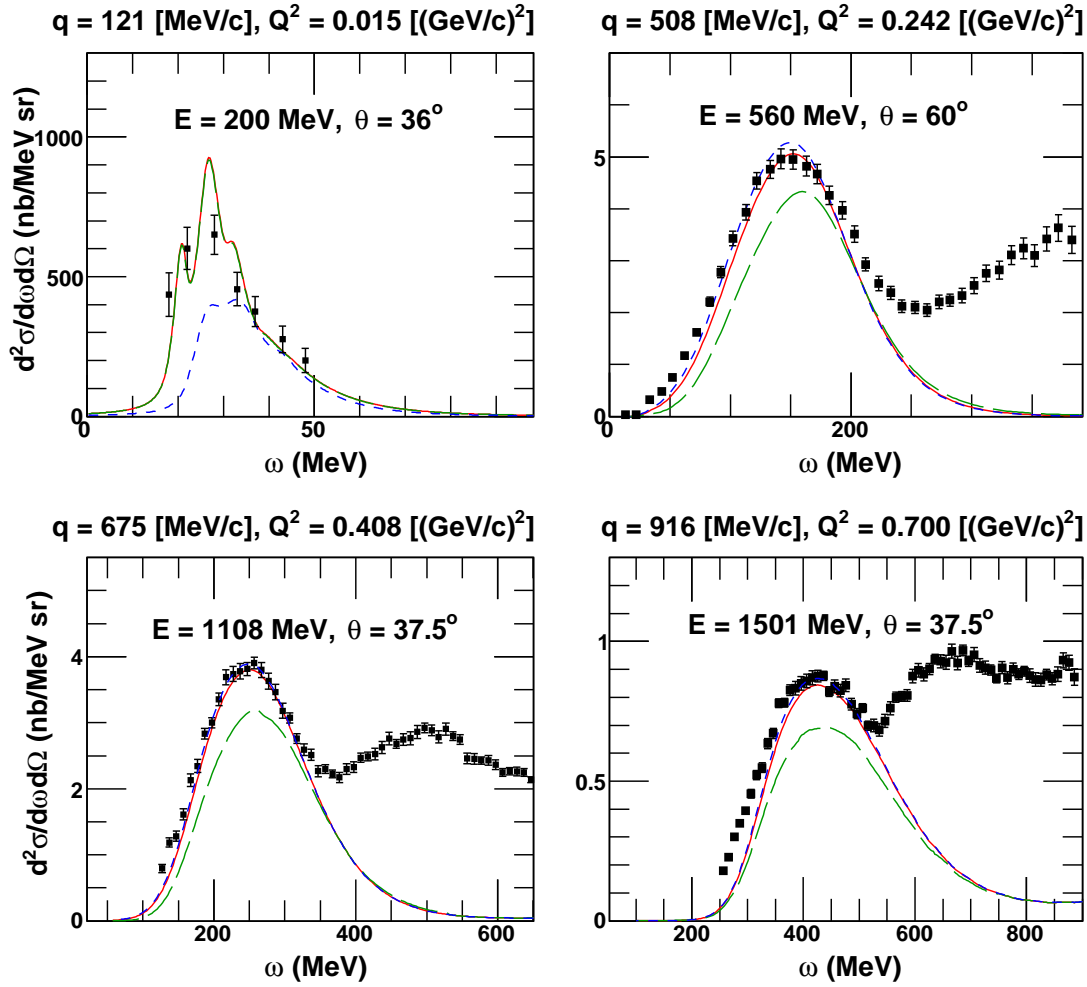

FIGURE 3.3: Comparison of ^{12}C(e, e') cross sections obtained with (full line) and without (dashed lines) the relativistic corrections. The experimental data are from Ref. [1, 2].

FIGURE 3.4: Comparison of ^{12}C(e, e') cross sections obtained with (full line) and without (large-dashed lines) using a dipole hadronic form factor at the nucleon-nucleon interaction vertices. The short-dashed lines are HF calculations. The experimental data are from Ref. [1, 2].

is negligible. Hence the adapted folding procedure significantly improved our description of data in giant resonance region but does not impact cross section at higher energies. For the sake of illustration, in Fig. 3.2, we compare cross sections achieved with two different folding procedures. The one we adapt (Eq. 2.61) and the one of Ref. [3]. As one can observe, both procedures have a quite similar effect on the cross-sections.

(b) Semi-relativistic correction

Our formalism is non-relativistic because it was originally developed to describe the low-energy nuclear physics where relativistic effects are negligible. The first challenge in the extension of the non-relativistic model to intermediate energies, is to account for relativistic effects. In order to improve our description at higher momentum transfers, we implemented a relativistic correction by a kinematic substitution (Eq. 2.63), in the nuclear response. This substitution effectively changes squared three-momentum transfers (q^2) into squared four-momentum transfers (Q^2).
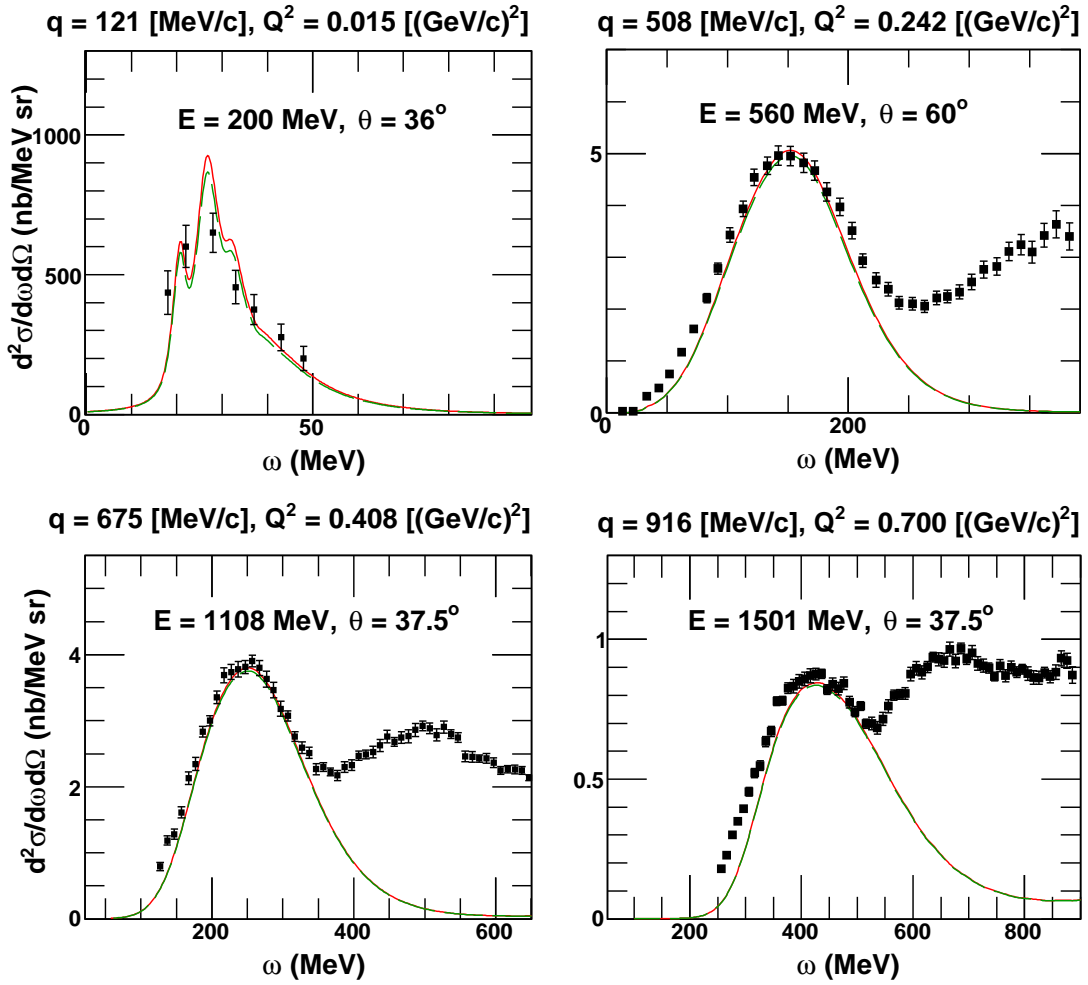
FIGURE 3.5: Comparison of ^{12}C(e, e') cross sections obtained with (full line) and without (dashed lines) using a modified effective momentum approximation. The experimental data are from Ref. [1, 2].

As a result shifting the QE peak roughly to right position. We show the effect of this relativistic correction in Fig. 3.3. It is evident from the figure that as one moves higher in energy and/or momentum transfer the non-relativistic description (dashed curves) becomes unrealistic. The relativistic correction reduces the width of the one-body responses and shifts the QE peak towards the correct value of ω. These relativistic corrections remarkably improve our description of the data at intermediate energy.

(c) Regularization of the nucleon-nucleon interaction

The parameters of SkE2 residual force were optimized against ground-state and low-excitation energy properties of spherical nuclei. At those conditions, the virtuality Q^2 of the nucleon-nucleon vertices is small. At intermediate energies, the Q^2 is higher and the SkE2 interaction becomes unrealistically strong. As shown in Fig. 3.4, at low energies (first panel) the CRPA cross sections are fine but as one moves higher in energy this unrealistically strong SkE2 residual force takes too much strength away from CRPA response (large-dashed curves). In order to remedy
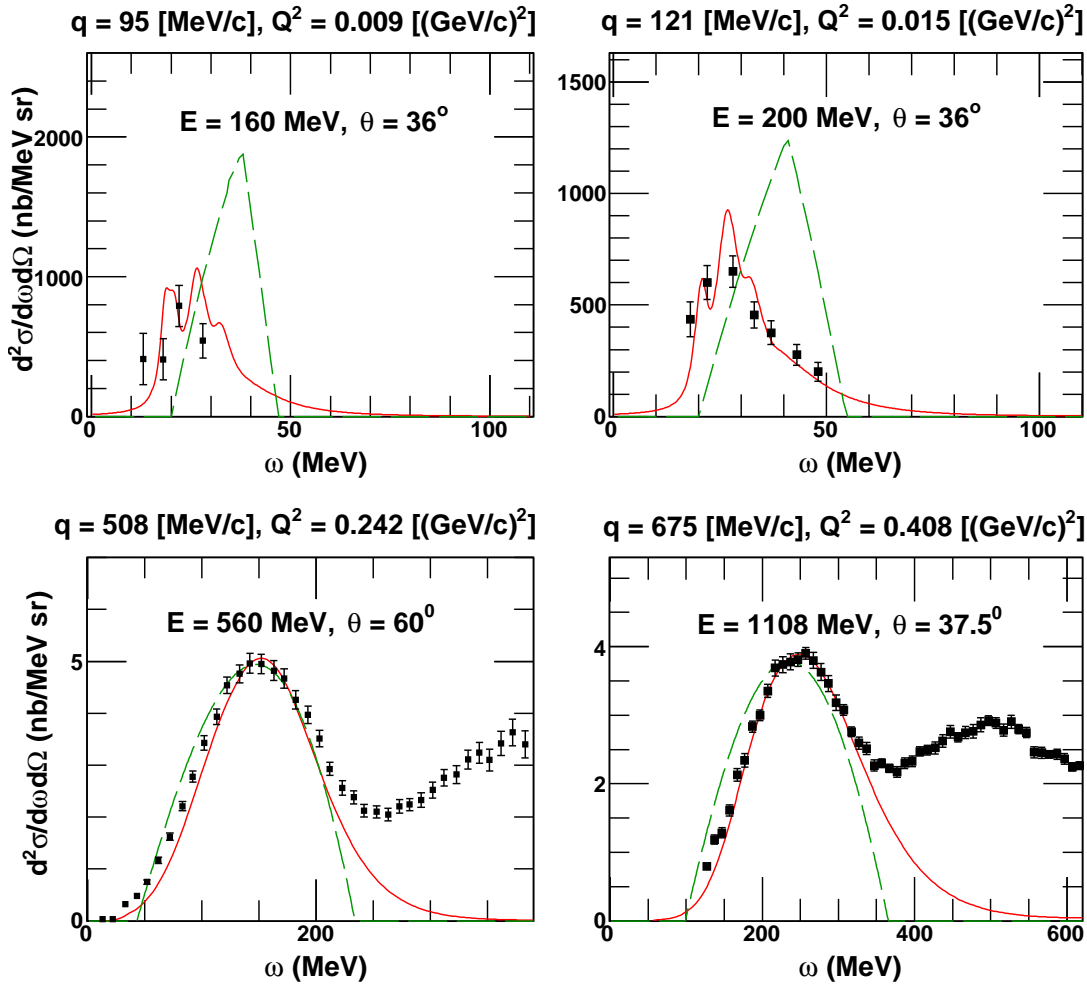
FIGURE 3.6: Comparison between relativistic global Fermi gas predictions [7] (dashed lines) and CRPA predictions (solid lines) for ^{12}C(e, e') double differential cross sections. Experimental data are taken from Refs. [1, 2]. The q and Q^2 values are evaluated at the quasielastic peak. E denotes the incident energy and θ the lepton scattering angle.

this, we introduced a dipole hadronic form factor at the nucleon-nucleon interaction vertices (Eq. 3.35), where we optimized the free parameter (of form factor) by a χ^2 test. In a χ^2 test, we compare the A(e, e') CRPA cross sections with almost all available experimental data in QE region and found a goodness of fit for Λ = 455 MeV. In Fig. 3.4, we show the effect of using this dipole form factor. The effects are negligible at lower energies but as one moves higher in energy the form factor controls the SkE2 force and improves the description of CRPA cross section with the data. As a result, as one move higher in energy the difference between HF and CRPA response disappear. The dipole form factor does not affect the HF cross section.

(d) Modified effective momentum approximation

At low energies, the effect of Coulomb potential on the outgoing charged lepton is generally taken into account by introducing a Fermi function. For higher energy, we implemented a modified effective momentum approximation where the effect of the Coulomb potential of the nucleus on

the lepton wave function is taken into account by replacing the phase factor in the cross section by an effective phase factor (Eq. 2.67). In Fig. 3.5, we show the effect of this approximation on our cross section results. The effect is visible at lower energies while at higher energies the effect almost becomes negligible.

RFG *vs* CRPA

The simulation codes used in the analysis of the experimental data are predominantly based on relativistic global Fermi gas (RFG) models. The RFG model provides a basic picture of the nucleus as a system of quasifree nucleons. The RFG can describe the QE cross-sections sufficiently accurately for medium momentum transfer ($q \approx 500$ MeV/c) reactions, but its description becomes poor for low momentum-transfer processes, where nuclear effects are prominent. In fact, the contribution from low-energy transfer processes, i.e., low-energy nuclear excitations and giant resonances, which can contribute even at higher energies and forward scatterings, as we will discuss in Section 3.2, are inaccessible in a RFG description. The inadequacy of RFG-based models to describe the nuclear effects contribute in the systematic uncertainties of the experimental analysis. For this reason, as an example in Fig. 3.6, we show a comparison of our CRPA predictions with RFG [7] ones. It is evident that the RFG model describes the cross sections at intermediate momentum transfers reasonably well (bottom panels) but fails to predict the low energy nuclear excitations (top panels), which contains rich nuclear structure information.

The rest of the chapter is organized as follows. In Sec. 3.1, we present our first CRPA calculations at intermediate energies. In this paper, we calculated flux-folded HF and CRPA cross sections for antineutrino scattering of ^{12}C and compare them with the MiniBooNE measurements. We discuss the role of an enhanced axial mass on flux-folded cross sections. In Sec. 3.2, we present our extended formalism by introducing the additional approximations and made a broad comparison of our QE cross sections with the available electron scattering data in order to test the reliability of the model. Our model describes the QE electron scattering cross sections reasonably well. The important feature of our model is in the description of low-energy nuclear excitations which are quite evident in the results of Sec. 3.2. We also paid special attention to the non-negligible contribution emerging from low-energy nuclear excitations in the signal of MiniBooNE and T2K like experiments.

We further made a full comparison of our flux-folded predictions with CCQE neutrino and antineutrino cross section measurements of MiniBooNE and with the inclusive QE and CCQE measurement performed by the T2K collaboration in Sec. 3.3. We discuss the role of low-energy nuclear excitations in the most forward bins of the MiniBooNE and T2K measurements. In Sec. 3.4, we present a comparison of the CRPA model with the RPA based model of Martini *et al* [8]. We analyse the similarities and differences in electron neutrino and muon neutrino induced cross sections on ^{12}C, which are relevant for neutrino-oscillation experiments looking for $\nu_\mu \rightarrow \nu_e$ oscillations.

Bibliography

[1] P. Barreau *et al.*, Nucl. Phys. A**402**, 515 (1983).

[2] R. M. Sealock *et al.*, Phys. Rev. Lett.**62**, 1350 (1989).

[3] R. D. Smith, J. Wambach, Phys. Rev. C**38**, 100 (1988).

[4] A. Botrugno, and G. Co', Nucl. Phys. **A761**, 200 (2005).

[5] A. De Pace, and M. Viviani, Phys. Rev. C**48**, 2931 (1993).

[6] J. E. Amaro, M. B. Barbaro, J. A. Caballero, T. W. Donnelly, and J. M. Udias, Phys. Rev. C**75**, 034613 (2007).

[7] W. M. Alberico, A. Molinari, T. W. Donnelly, E. L. Kronenberg, and J. W. Van Orden, Phys. Rev. C**38**, 1801 (1988).

[8] M. Martini, M. Ericson, G. Chanfray, J. Marteau, Phys. Rev. C**80**, 065501 (2009).

3.1 Quasielastic contribution to antineutrino-nucleus scattering [1]

V. Pandey, N. Jachowicz, J. Ryckebusch, T. Van Cuyck, W. Cosyn

Department of Physics and Astronomy, Ghent University,
Proeftuinstraat 86, B-9000 Gent, Belgium.

Abstract

We report on a calculation of cross sections for charged-current quasielastic antineutrino scattering off ^{12}C in the energy range of interest for the MiniBooNE experiment. We adopt the impulse approximation (IA) and use the nonrelativistic continuum random phase approximation (CRPA) to model the nuclear dynamics. An effective nucleon-nucleon interaction of the Skyrme type is used. We compare our results with the recent MiniBooNE antineutrino cross-section data and confront them with alternate calculations. The CRPA predictions reproduce the gross features of the shape of the measured double-differential cross sections. The CRPA cross sections are typically larger than those of other reported IA calculations but tend to underestimate the magnitude of the MiniBooNE data. We observe that an enhancement of the nucleon axial mass in CRPA calculations is an effective way of improving on the description of the shape and magnitude of the double-differential cross sections. The rescaling of M_A is illustrated to affect the shape of the double-differential cross sections differently than multinucleon effects beyond the IA.

I. Introduction

Recent times have been marked by a substantial increase in the amount of data for (anti)neutrino-nucleus interactions at intermediate energies. Recently, the MiniBooNE collaboration has published their first charged-current quasielastic (CCQE) antineutrino-nucleus scattering cross-section measurements [1]. The underlying reaction process of CCQE with antineutrino beams is $\bar{\nu}_\mu + p \rightarrow \mu^+ + n$ on bound protons. Antineutrino-nucleus ($\bar{\nu}A$) cross sections are less well measured than their neutrino counterparts, mainly because of higher background contributions and smaller statistics [2]. MiniBooNE has also published cross sections for CCQE neutrino ($\nu_\mu + n \rightarrow \mu^- + p$) [3] and neutral-current quasielastic (NCQE) neutrino ($\nu_\mu + N \rightarrow \nu_\mu + N$) [4] processes. Several other collaborations have been contributing to the increase of the neutrino-nucleus cross section database in recent times. For example, T2K has released inclusive CC neutrino [5] data, whereas MINERνA presented CC neutrino [6] and antineutrino [7] cross section results.

The modeling of νA and $\bar{\nu}A$ scattering data poses some real challenges. In contrast to electron-nucleus scattering data for which the initial electron energy is exactly known, the νA and $\bar{\nu}A$ data are ν ($\bar{\nu}$)-flux integrated [8]. Despite the enormous improvements in the experimental and

---

[1]This manuscript is published as Phys. Rev. C**89**, 024601 (2014). I performed the numerical calculations, made the figures and drafted the manuscript.

theoretical understanding of (anti)neutrino-nucleus interactions in the few GeV region, the current experimental precision is of the order of 20 – 30% and the underlying processes on bound nucleons are not fully understood [2, 8–10]. Theoretical predictions for MiniBooNE's $\bar{\nu}_\mu+^{12}$C measurements are reported in Refs. [11–15]. References [11, 12] adopt a rather basic nuclear-structure model which cannot be expected to capture the complexity of the nuclear dynamics at low nuclear excitation energies. Reference [13] starts from a relativistic mean-field model for the bound and scattering states. The approach in Ref. [14] is based on superscaling approximation and Ref. [15] adopts a relativistic Green's function model. Reference [11] computes nuclear response functions with a local Fermi gas model in the random phase approximation (RPA) and incorporates multinucleon effects exclusively in the spin-isospin channels. Reference [12] starts from a local Fermi gas description of the nucleus and includes RPA correlations and multinucleon effects. Both calculations for the $\bar{\nu}_\mu+^{12}$C responses stress the importance of multinucleon mechanisms at MiniBooNE kinematics, and adopt a value for the axial mass ($M_A \approx 1$ GeV) in a dipole parametrization of the axial form factor, which is consistent with the one used to model the QE contribution to $\nu_\mu+^{12}$C [16–19]. The multinucleon mechanisms account for mechanisms in the W-nucleus coupling beyond the impulse approximation (IA). In the IA, the W-nucleus coupling is approximated as a sum of one-body W-nucleon couplings. Effects beyond the IA introduce some uncertainties in the calculations, particularly for finite nuclei as a consistent treatment of the multinucleon electroweak currents is extremely challenging. According to a recent study of neutrino scattering off the deuteron the effect of two-body currents (excluding pion production channels) is smaller than 10% [20].

In this work, we adopt the IA for modeling the electroweak-nucleus coupling and use a more sophisticated model for describing the structure of the initial and final nuclei. In our approach to investigate MiniBooNE's CCQE $\bar{\nu}_\mu+^{12}$C results, we model the nuclear dynamics starting from the mean field (MF) description and introduce long-range correlations by means of a nonrelativistic continuum RPA (CRPA) framework. Thereby, we use Green's functions (or propagators) to solve the CRPA equations and an effective Skyrme nucleon-nucleon residual interaction. The model takes into account one-particle one-hole (1p-1h) excitations out of a correlated nuclear ground state. In the CRPA, the effects of final-state interactions of the ejected nucleons with the residual nucleus are implemented. Thereby, one accounts for both distortions on the ejected nucleon waves and rescatterings with the residual A-1 nucleons. For example, rescattering effects $\bar{\nu}_\mu + p + (A-1) \to \mu^+ + n + (A-1) \to \mu^+ + n' + (A-1)'$ are included. In CRPA the strength of the rescatterings is regulated with the residual nucleon-nucleon force. In the results section we focus on the influence of RPA correlations on the computed antineutrino responses for the MiniBooNE kinematics. The CRPA formalism does not contain relativistic corrections in its description of the nuclear dynamics. In Refs. [17, 21, 22] one proposes to correct the energy transfer ω to account for relativistic effects in non-relativistic Fermi-gas calculations. These methods, however, cannot be readily applied to the CRPA framework, as the computed response scales with the asymptotic nucleon kinetic energies in a complicated fashion. It is worth mentioning that MiniBooNE's antineutrino flux distribution is shifted to lower energies compared to the neutrino one. Therefore, it can be anticipated that the $\bar{\nu}_\mu+^{12}$C responses are subject to smaller relativistic corrections than the $\nu_\mu+^{12}$C ones.

The paper is organized as follows. In Sec. II, we briefly describe the CRPA framework of our cross-section calculations. In Sec. III, we present numerical results of $\bar{\nu}_\mu + {}^{12}\text{C}$ cross sections and compare them with the MiniBooNE data and with other theoretical models. The conclusions are given in Sec. IV.

II. Formalism

In this work, we focus on the inclusive CCQE antineutrino nuclear reaction

$$\bar{\nu}_\mu + {}^{12}\text{C} \rightarrow \mu^+ + X \ , \tag{3.1}$$

with no pion in the final state, a process which is referred to as QE-like [16, 17, 23]. We obtain nuclear responses with the CRPA method, which is described in details in Refs. [24, 25]. This formalism has been successfully used in the description of exclusive photo-induced and electro-induced QE processes [26, 27] and in inclusive neutrino scattering at supernova energies [24, 25, 28, 29]. Here, the CRPA method is applied to antineutrino-nucleus interactions at intermediate energies. The CRPA framework includes all single-nucleon knockout channels and is therefore well suited to compute the quasielastic contribution to the inclusive (anti)neutrino-nucleus responses. The CRPA framework is not suited to compute the contributions from alternate reaction mechanisms such as multinucleon knockout.

We summarize the basis ingredients of the model. An effective Skyrme two-body interaction (more specifically, the SkE2 parametrization [26]) is used to construct a mean-field (MF) potential. The bound and continuum single-nucleon wave functions can be obtained as the solutions to the corresponding Schrödinger equation. The long-range correlations between the nucleons are introduced through the RPA which describes an excited nuclear state with a nucleon in the energy continuum of the MF potential as the coherent superposition of particle-hole (ph^{-1}) and hole-particle (hp^{-1}) excitations out of a correlated ground state, which has 0p-0h and 2p-2h components

$$|\Psi_{RPA}^C\rangle = \sum_{C'} \left\{ X_{C,C'} \ |ph^{-1}\rangle - \ Y_{C,C'} \ |hp^{-1}\rangle \right\} \ . \tag{3.2}$$

Here, C' stands for a combination of all quantum numbers of a hole and particle state. Green's function theory allows one to treat the single-particle energy continuum exactly [26]. In computing the response of the nucleus to an external electroweak probe a key quantity is the RPA polarization propagator which can be obtained as a solution to the following iterative equation :

$$\Pi^{(RPA)}(x_1, x_2; E_x) = \Pi^{(0)}(x_1, x_2; E_x) + \frac{1}{\hbar} \int dx dx' \Pi^0(x_1, x; E_x) \tilde{V}(x, x') \Pi^{(RPA)}(x', x_2; E_x), \tag{3.3}$$

where E_x is the excitation energy of the target nucleus and x is a shorthand notation for the combination of the spatial, spin and isospin coordinates. Further, $\Pi^{(0)}$ denotes the MF contribution to the polarization propagator and $\tilde{V}$ is the antisymmetrized residual interaction. The MF responses can be computed by neglecting the second term in the above equation. The second term accounts for the multiple-scattering events after the initial electroweak excitation of a nucleon from a bound into a continuum state. In the MF approach, only direct nucleon knockout

is included and the sole implemented final-state interaction (FSI) effect is the distortion of the ejected-nucleon waves in the real MF potential of the residual nucleons.

In terms of the experimentally measured quantities (outgoing muon kinetic energy T_μ and cosine of the muon scattering angle $\cos\theta_\mu$), the twofold differential cross section for CC (anti)neutrino-nucleus scattering is given by :

$$\left(\frac{d^2\sigma}{dT_\mu d\cos\theta_\mu}\right)_{\nu,\bar\nu} = G_F^2 \ \cos^2\theta_c \ \left(\frac{2}{2J_i+1}\right) \ \varepsilon_\mu^2 \ \tilde{k}_\mu \ F\left(Z',\varepsilon_\mu\right) \left[\sum_{J=0}^\infty \sigma_{CL}^J + \sum_{J=1}^\infty \sigma_T^J\right], \qquad (3.4)$$

where G_F is the weak interaction coupling constant and θ_c is the Cabibbo angle. Further, $\tilde{k}_\mu = k_\mu/\varepsilon_\mu$ with k_μ (ε_μ) is the momentum (energy) of the final lepton. The Fermi function $F\left(Z',\varepsilon_\mu\right)$, is introduced in order to take into account the Coulomb interaction between the outgoing lepton and the residual nucleus which has a proton number Z'. In order to compute the differential cross sections we rely on a multipole expansion of the weak transition operators and in Eq. (3.4) the σ_{CL}^J and σ_T^J are the Coulomb longitudinal and the transverse contributions for a given multipolarity J :

$$\begin{aligned}
\sigma_{CL}^J &= v^{\mathcal{M}} \ |\langle J_f||\widehat{\mathcal{M}}_J(|\vec{q}|)||J_i\rangle|^2 + v^{\mathcal{L}} \ |\langle J_f||\widehat{\mathcal{L}}_J(|\vec{q}|)||J_i\rangle|^2 \\
&\quad + 2 \ v^{\mathcal{ML}} \ \mathcal{R}\left[\langle J_f||\widehat{\mathcal{L}}_J(|\vec{q}|)||J_i\rangle\langle J_f||\widehat{\mathcal{M}}_J(|\vec{q}|)||J_i\rangle^*\right],
\end{aligned}$$

$$(3.5)$$

with

$$v^{\mathcal{M}} = \left[1 + \tilde{k}_\mu\cos\theta_\mu\right],$$

$$v^{\mathcal{L}} = \left[1 + \tilde{k}_\mu\cos\theta_\mu - \frac{2\varepsilon_i\varepsilon_\mu}{|\vec{q}|^2}\tilde{k}_\mu^2\sin^2\theta_\mu\right],$$

$$v^{\mathcal{ML}} = \left[\frac{\omega}{|\vec{q}|}(1+\tilde{k}_\mu\cos\theta_\mu) + \frac{m_\mu^2}{\varepsilon_\mu|\vec{q}|}\right],$$

and

$$\begin{aligned}
\sigma_T^J &= v^T \left[|\langle J_f||\widehat{\mathcal{J}}_J^{mag}(|\vec{q}|)||J_i\rangle|^2 + |\langle J_f||\widehat{\mathcal{J}}_J^{el}(|\vec{q}|)||J_i\rangle|^2\right] \\
&\quad \mp 2 \ v^{TT} \ \mathcal{R}\left[\langle J_f||\widehat{\mathcal{J}}_J^{mag}(|\vec{q}|)||J_i\rangle\langle J_f||\widehat{\mathcal{J}}_J^{el}(|\vec{q}|)||J_i\rangle^*\right],
\end{aligned}$$

$$(3.6)$$

with

$$v^T = \left[1 - \tilde{k}_\mu\cos\theta_\mu + \frac{\varepsilon_i\varepsilon_\mu}{|\vec{q}|^2}\tilde{k}_\mu^2\sin^2\theta_\mu\right],$$
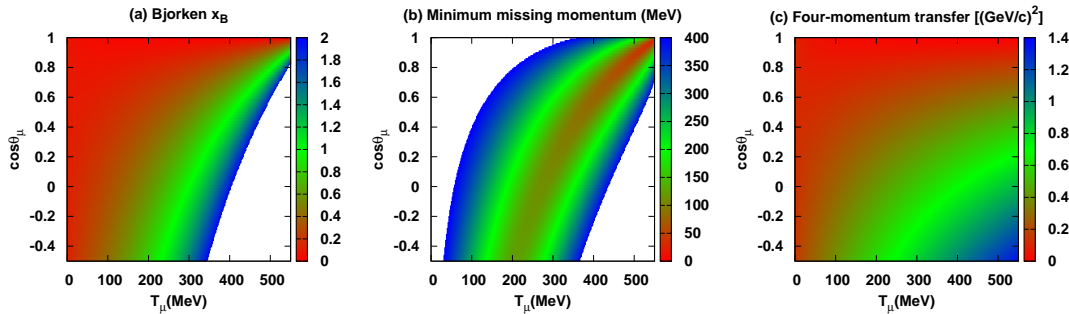
FIGURE 3.7: (Color online) The kinematic variables (a) Bjorken x_B, (b) minimum p_{mis}, and (c) Q^2 as a function of T_μ and $\cos\theta_\mu$ at $E_{\bar{\nu}_\mu}=700$ MeV. White regions correspond with values of the variables out of the specified ranges.

$$v^{TT} = \left[\frac{\varepsilon_i + \varepsilon_\mu}{|\vec{q}|}(1 - \tilde{k}_\mu \cos\theta_\mu) - \frac{m_\mu^2}{\varepsilon_\mu|\vec{q}|} \right].$$

Here, $Q^2 = -q^\mu q_\mu$, with $q^\mu\,(\omega, \vec{q})$ the transferred four-momentum carried by the W boson. ε_i is energy of the incoming neutrino and m_μ is the mass of the final lepton. The $\widehat{\mathcal{M}}_J$, $\widehat{\mathcal{L}}_J$, $\widehat{\mathcal{J}}_J^{el}$ and $\widehat{\mathcal{J}}_J^{mag}$ denote the Coulomb, longitudinal, transverse electric and transverse magnetic transition operators as defined in Refs. [24, 25]. The $|\vec{q}|$ is the magnitude of the transferred three-momentum and $J_i\,(J_f)$ represents the total angular momentum of the initial (final) state of the nucleus. The difference between the neutrino and antineutrino CC cross section stems from the sign assigned to the interference term in Eq. (3.6): positive for the neutrino and negative for the antineutrino beams.

As mentioned, in this work we adopt the IA. Now we introduce a number of variables which allow one to assess the validity of this approximation for given kinematic settings. The Bjorken x_B scaling variable is given by the invariant quantity

$$x_B \;=\; \frac{AQ^2}{2p_A^\mu q_\mu} \;, \tag{3.7}$$

where p_A^μ is the momentum of the target nucleus. Figure 3.7 displays x_B as a function of the experimentally measured quantities T_μ and $\cos\theta_\mu$ for $E_{\bar{\nu}_\mu} = 700$ MeV. As shown in Fig. 3.8, MiniBooNE's $\bar{\nu}_\mu$ energy spectrum reaches its mean near 700 MeV. For $x_B \approx 1$, QE single-nucleon knockout is expected to dominate and IA calculations are expected to perform best. From Fig. 3.7 it is clear that at very forward θ_μ one expects the bulk of the single-nucleon knockout strength at larger T_μ. With increasing θ_μ the QE single-nucleon knockout strength will shift to lower T_μ. At kinematic conditions corresponding with both low T_μ and forward muon scattering angles, one could expect major contributions beyond the IA.

The x_B is a model-independent kinematic variable. We now introduce a kinematic variable which is a highly relevant one for QE processes. In direct single-nucleon knockout reactions, the momentum of the initial bound nucleon (often referred as the missing momentum p_{mis}) is the scaling variable [30]. Indeed, in the plane-wave limit, the exclusive single-nucleon knockout cross sections are directly proportional to the momentum distribution of the bound nucleons in the target nucleus. Mean-field nucleons are characterized by a momentum distribution which
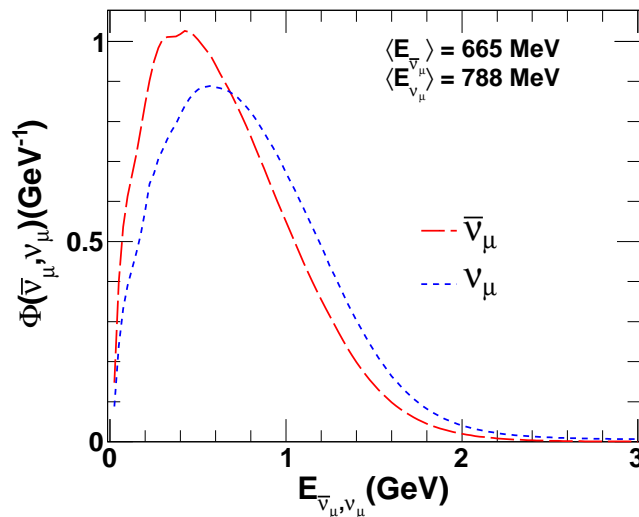
FIGURE 3.8: (Color online) The MiniBooNE antineutrino and neutrino flux [1, 3] normalized to 1.

is Gaussian-like and extends over a specific range ($0 \leq p_{mis} \lesssim 250$ MeV) [31]. Large missing momenta necessarily lead to small single-nucleon knockout cross sections and/or substantial contributions from competing multinucleon processes. Imposing a QE reaction process ($W^- + p$ with $A - 1$ spectators), energy and momentum conservation in the laboratory frame can be expressed as

$$M_A + \omega = E^\star_{A-1} + \sqrt{M_n^2 + p_n^2}, \quad \vec{p}_{mis} + \vec{q} = \vec{p}_n , \tag{3.8}$$

where $\vec{p}_n$ is the three-momentum of the ejected neutron in the laboratory frame, M_n is the neutron mass, and M_A the mass of the target nucleus. The $E^\star_{A-1}$ is the total energy of the residual nucleus and includes contributions from recoil and excitation energy $E^\star_{A-1} = M_{A-1} + T_{A-1} + E^\star_{exc}$. The p_{mis} depends on $\theta_{p_n q}$, the angle between $\vec{q}$ and $\vec{p}_n$. For inclusive reactions as those considered in this work, the relative importance of the quasielastic contribution can be estimated with the aid of the minimum missing momentum: the minimum value of p_{mis} as $\theta_{p_n q}$ varies between $0°$ and $180°$. In Fig. 3.7 we also display the minimum value of the missing momentum, denoted as p^{min}_{mis} for a given incoming neutrino energy and $T_{A-1} + E^\star_{exc} = 25$ MeV. As one moves along the $x_B \approx 1$ region, with increasing θ_μ a shift to larger p^{min}_{mis} is observed and larger multinucleon contributions can be expected [32]. The $(T_\mu, \cos\theta_\mu)$ kinematic settings with a minimum $p_{mis} \gtrsim 250$ MeV are prone to multinucleon corrections beyond the IA. For the sake of completeness, we also show a contour plot of the W boson's virtuality. Kinematic regions with the lowest Q^2 exhibit the strongest sensitivity to collective nuclear structure mechanisms.

The wide range of values of (x_B, p^{min}_{mis}, Q^2) probed in the MiniBooNE $\bar{\nu}_\mu + {}^{12}$C experiment, presents real challenges to the theoretical models. Accordingly, one can expect rather divergent views about the impact of various reaction mechanisms.
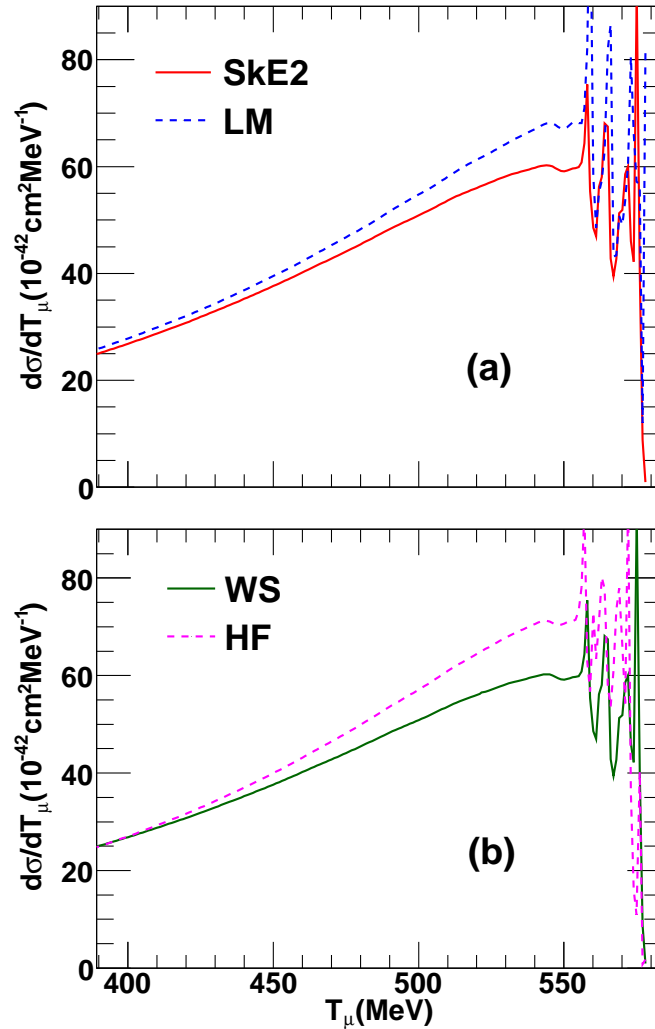
FIGURE 3.9: (Color online) The T_μ dependence of the QE antineutrino-^{12}C CRPA cross sections for $E_{\bar{\nu}_\mu} = 700$ MeV. (a) Curves obtained with the SkE2 and Landau-Migdal (LM) residual interaction with WS as single-particle wave functions. (b) Curves obtained with the WS and HF single-particle wave functions with SkE2 as residual interaction.

III. Results

Various studies have attempted to bring the predictions of (anti)neutrino-nucleus models in accordance with experimental data. Several modifications of the IA-based models have been considered, including the enhancement of the axial mass M_A and the introduction of multinucleon effects [16, 19]. These approaches have similar effects on neutrino scattering cross sections, bringing predictions closer to data. This impedes extraction of M_A directly from the data and makes it difficult to use data to constrain the importance of multinucleon effects. In the following, we seek to shed light on these issues by making an analysis of QE cross sections and the relative importance of different contributions to neutrino and antineutrino scattering processes. We will show that multinucleon contributions and an enhanced axial mass affect the shape of the cross section differently and alter neutrino and antineutrino cross sections in a different way.

In order to test the robustness of calculations, we first investigate their sensitivity to the nuclear

physics input. In computing the electroweak responses with the CRPA method, input is required with regard to the residual nucleon-nucleon interactions, the mean-field wave functions, and mean-field potential. In Fig. 3.9, the sensitivity of the computed cross sections to the nuclear-physics input is studied at $E_{\bar{\nu}_\mu}$ =700 MeV. In the top panel, we compare cross sections obtained with a Skyrme (SkE2) [27, 33] and a Landau-Migdal parametrization [34] for the residual effective nucleon-nucleon (NN) force. The sensitivity to the NN force is small for low outgoing muon energies but becomes substantial at higher T_μ, corresponding to lower nuclear excitation energies where differences amount to almost 15%. This is expected as it corresponds with a kinematic range most prone to nuclear collective effects. At low T_μ the cross sections are rather insensitive to the details of the residual NN force. A similar analysis is made for the use of different bound-state single-nucleon wave function Woods-Saxon (WS) [35] and Hartree-Fock (HF), in the bottom panel. Here again, significant differences up to 20% arise at higher T_μ. Similar effects arise for calculations at other incoming energies. The strongest sensitivity, both for the shape and the magnitude of the cross section, to the nuclear-structure input occurs at the high-T_μ edges (corresponding to low nuclear excitation energies) of the computed cross sections. Concluding, even within the same approach, there is some sensitivity of the cross sections to the nuclear-structure input. We would like to stress that the parametrizations used in our calculations are not tuned in any way to the MiniBooNE data.

The flux-integrated double-differential cross section for CCQE antineutrino-nucleus scattering, in terms of the measured quantities T_μ and $\cos\theta_\mu$ (hence free from the energy reconstruction issue [9, 23, 36]) can be written as

$$\left\langle \frac{d^2\sigma}{dT_\mu d\cos\theta_\mu} \right\rangle = \frac{1}{\int \Phi(E_{\bar{\nu}})dE_{\bar{\nu}}} \int \left[\frac{d^2\sigma}{dT_\mu d\cos\theta_\mu} \right]_{E_{\bar{\nu}}} \Phi(E_{\bar{\nu}})dE_{\bar{\nu}} \ , \qquad (3.9)$$

where the antineutrino flux $\Phi(E_{\bar{\nu}})$ is taken from [1]. The energy distribution of the MiniBooNE normalized antineutrino and neutrino flux is shown in Fig. 3.8. The neutrino flux peaks at higher energies than the antineutrino one.

In this work, incoming antineutrino energies up to $E_{\overline{\nu}_\mu} = 2$ GeV and multipoles up to $J = 12$, are included in the calculations. We have checked that under all considered kinematic conditions, the computed inclusive antineutrino cross sections do not receive sizable contributions from $J > 12$ multipoles. Unless specified otherwise, the used bound-state single-particle wave functions are solutions to the Schrödinger equation with a WS potential.

The double-differential $^{12}C(\bar{\nu}_\mu, \mu^+)X$ cross sections per target proton are displayed in Fig. 3.10. The CRPA and MF calculations are folded with the MiniBooNE $\bar{\nu}_\mu$ flux of Fig. 3.8. In the dipole axial form factor, we adopt $M_A = 1.03$ GeV which is essentially tuned to deuterium bubble chamber data. The uncertainties (both with regard to shape and to normalization) in the MiniBooNE data are not shown. Comparing the CRPA and MF results in Fig. 3.10, it is clear that the inclusion of RPA correlations reduces the cross sections, at the same time shifting the strength towards lower muon energies. Obviously, both the MF and CRPA calculations reproduce the major features of the measured $(\cos\theta_\mu, T_\mu)$ distributions: the largest cross sections are for forward θ_μ and the peaks shift to smaller T_μ with increasing θ_μ. This is completely in line with the expectations from the $(\cos\theta_\mu, T_\mu)$ dependence of the x_B and minimum p_{mis} of Fig. 3.7.
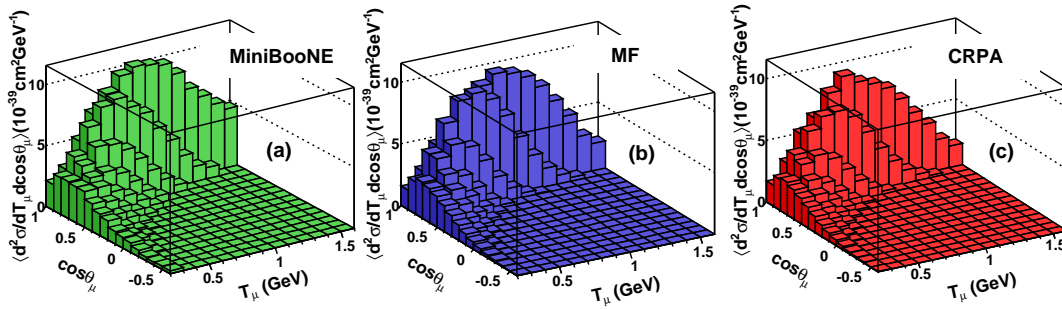
FIGURE 3.10: (Color online) Double-differential cross section per target proton for $^{12}C(\bar{\nu}_\mu, \mu^+)X$, as a function of T_μ and $\cos\theta_\mu$. The MiniBooNE data [1] are plotted without the shape uncertainty and also excludes the 17.2% normalization uncertainty. CRPA and MF calculations are folded with MiniBooNE $\bar{\nu}_\mu$ flux.
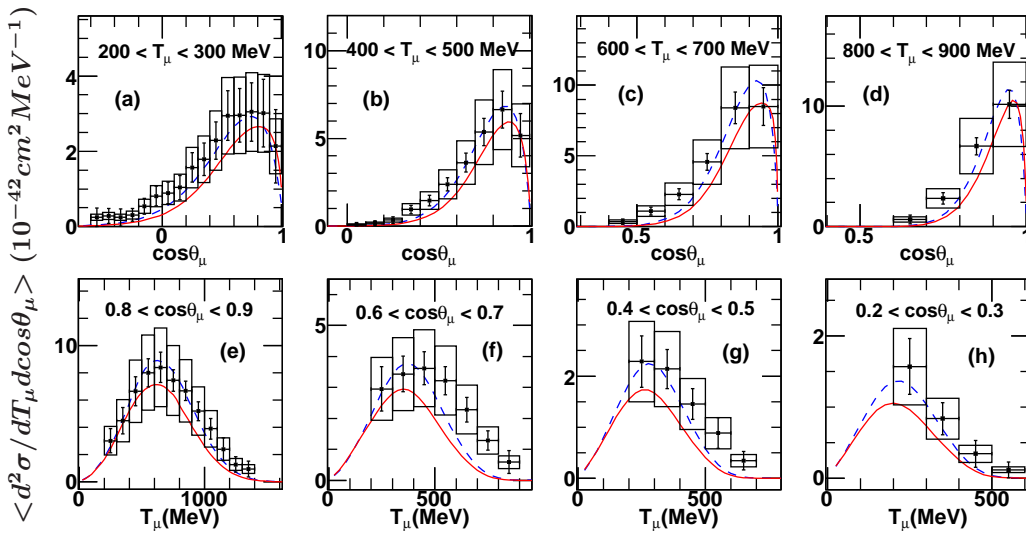

FIGURE 3.11: (Color online) MiniBooNE flux-folded double-differential cross section per target proton for $^{12}C(\bar{\nu}_\mu, \mu^+)X$ plotted as a function T_μ for different ranges of $\cos\theta_\mu$ (bottom), as a function of $\cos\theta_\mu$ for different T_μ values (top). Solid curves are CRPA and dashed curves are MF calculations. MiniBooNE data are filled squares, error bars represent the shape uncertainties and error boxes represent the 17.2% normalization uncertainty.

Figure 3.11 shows a more detailed picture, displaying double-differential cross sections as a function of T_μ ($\cos\theta_\mu$) for various bins in the other kinematic variable. The theoretical results are obtained by integrating the calculations over the corresponding bin width. The MiniBooNE data of Fig. 3.11 include the experimental uncertainties. Overall, the CRPA predictions are in satisfactory agreement with the data. The quality of agreement between the CRPA calculations and data is best at low and average muon kinetic energies and forward muon angles. At backward $\cos\theta_\mu$, the CRPA tends to underestimate the data for higher T_μ values. It has been suggested by several authors that multinucleon excitations are at the origin of the missing strength at higher T_μ and backward θ_μ, as that region corresponds with large values of x_B and minimum p_{mis}. The quenching due to RPA correlations is strongest at backward θ_μ and disappears at the T_μ edges of the distributions. In general the MF provides a better description of the data than CRPA both for the shape and magnitude of the cross section. A similar observation was made in Ref. [37], where two approaches are considered to compute the CCQE $\nu_\mu + {}^{12}C$ cross sections,
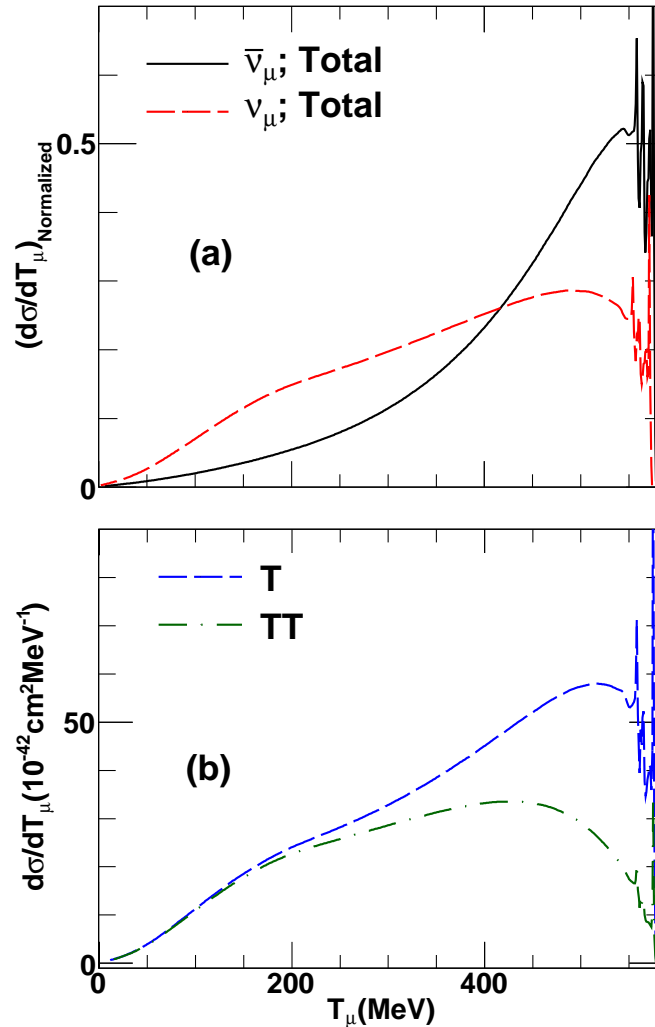
FIGURE 3.12: (Color online) The T_μ distribution of the CRPA ^{12}C$(\bar{\nu}_\mu, \mu^+)$ and ^{12}C(ν_μ, μ^-) cross sections at a (anti)neutrino energy of 700 MeV. (a) Total cross sections normalized to 1. (b) Transverse contribution excluding the interference part (T) and the transverse interference (TT) contribution.

superscaling and the relativistic mean-field (RMF) approach. Of these two, the RMF model was observed to provide the best description of the shape of the double-differential cross sections. Our calculations are in line with those of the RMF model of [13], yet slightly closer to the data.

Various studies have observed different contributions of RPA and multinucleon effects for neutrino and antineutrino cross sections. The top panel of Fig. 3.12 shows QE neutrino and antineutrino cross sections, both normalized to one. In absolute numbers, the neutrino cross section is always larger, but the normalized cross section shows that antineutrino processes exhibit a stronger sensitivity to contributions stemming from the high end of the T_μ spectrum. As illustrated in the bottom panel of Fig. 3.12, this difference can be explained by the sign of the transverse interference term in Eq. (3.6). For neutrinos, both transverse terms add constructively, while for antineutrinos they add destructively. The absolute value of the interference contribution to σ_T is relatively small. Still, for low T_μ, the comparable size of both transverse contributions results in a sizable gain of importance of the transverse interference term. Therefore, at low T_μ,
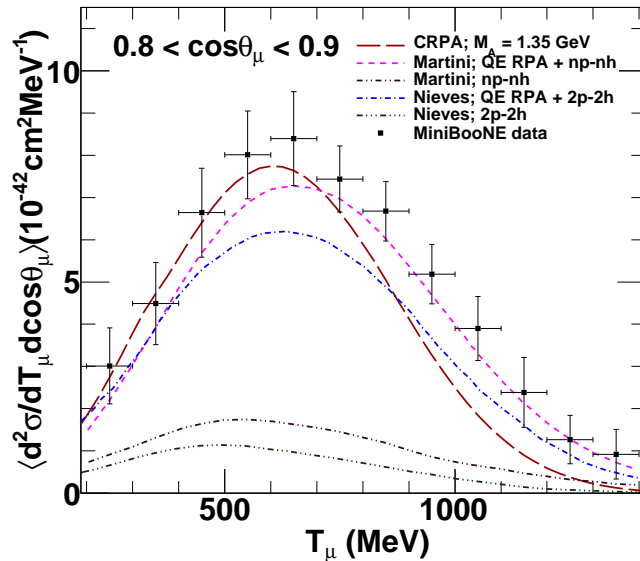
FIGURE 3.13: (Color online) MiniBooNE flux-folded cross section per target proton for $^{12}C(\bar{\nu}_\mu, \mu^+)X$ at $0.8 < \cos\theta_\mu < 0.9$. The CRPA predictions are compared with those of Refs. [11] and [12].

the difference between the ν_μ and $\bar{\nu}_\mu$ cross sections increases and the antineutrino ones become very small. Hence, the main contribution to antineutrino scattering comes from reactions at higher T_μ values and antineutrino-nucleus reactions are relatively more sensitive to low-energy nuclear dynamics than their neutrino counterparts. As can be appreciated from Fig. 3.12, low nuclear excitation energies represent a large share of the folded cross sections. Accordingly, one may expect that the effect of the RPA correlations is stronger for $\bar{\nu}_\mu A$ interactions.

As a consequence of these differences and the respective energy dependence of cross sections, one can also expect differing influences of multinucleon effects on neutrino and antineutrino cross sections. The effect of multinucleon contributions to the $\bar{\nu}_\mu$ double-differential cross sections is studied among others in Refs. [11, 12, 14] and to the ν_μ cross sections in Ref. [17, 37, 38]. From those studies, particularly from Figs. 1 and 4 in Ref. [37], it emerges that for the very forward-peaked neutrino scattering in MiniBooNE kinematics, multinucleon contributions are responsible for a significant fraction of the strength at low T_μ and are essential for reproducing the data. At backward θ_μ, where cross sections are very small anyway, the effect of the multinucleon contributions is rather modest. This can be understood by realizing that backward θ_μ corresponds with larger values of Q^2 (Fig. 3.7). With increasing values of the range parameter Q^2, multinucleon effects naturally lose in importance [39]. In the superscaling approach of Ref. [37], it is argued that the relative impact of np-nh contributions increases with growing energies of the incoming lepton. Moreover, pion-less intermediate Δ creation is a source of strength beyond the IA that gains in importance as one approaches the pole of the Δ propagator [39, 40]. From Fig. 3.12 it became obvious that the antineutrino-nucleus reaction has an enhanced sensitivity to the strength stemming from lower nuclear excitation energies. More specifically in the Mini-BooNE experiment, the antineutrino flux peaks at lower energies than the neutrino one as shown in Fig. 3.8. Under those kinematic circumstances, one might expect strong nuclear effects but reduced np-nh contributions through pionless Δ decay, for example.
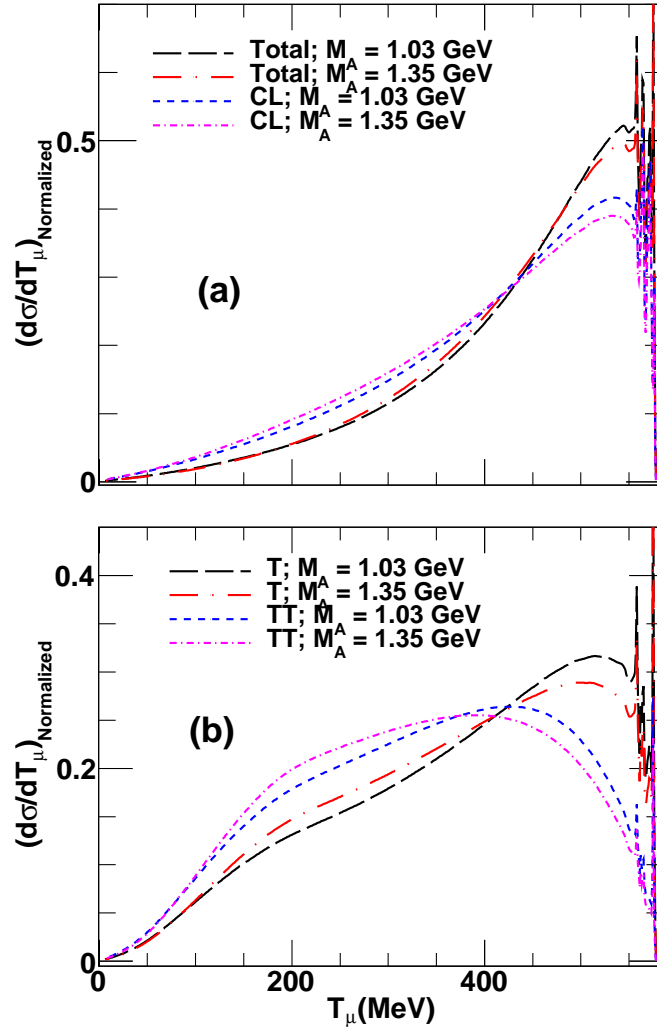
FIGURE 3.14: (Color online) Normalized Coulomb longitudinal (CL), transverse term without interference (T) and transverse interference (TT) contributions to $^{12}\text{C}(\bar{\nu}_\mu, \mu^+)X$ as a function of T_μ for two different values of M_A, at $E_{\bar{\nu}_\mu} = 700$ MeV.

Obviously, modeling the multitude of np-nh effects at various energies introduces uncertainties. Figure 3.13 shows the predicted contribution from np-nh to the $^{12}\text{C}(\bar{\nu}_\mu, \mu^+)X$ cross section for two models available in the literature. Whereas the shape of the energy-dependence of the multinucleon contribution is predicted slightly differently in these studies, its magnitudes differs considerably. In both studies, the shape of flux-averaged np-nh contributions is similar to that of the QE cross section. The divergent views about the role of the np-nh illustrate that the model dependencies are unavoidable given the extensive range of x_B, p_{mis}^{min}, Q^2 (Fig. 3.7) values covered in the experiments. The good general agreement of the calculations is mainly obtained by the combination of QE and multinucleon contributions, averaging out the most apparent discrepancies.

The (anti)neutrino-nucleus response calculations require input with regard to the two vector and the axial form factors. They are often parametrized as a dipole function of the range parameter Q^2. As a result, each form factor introduces at least two parameters, a cutoff mass, formally playing the role of a size parameter and the value at $Q^2 = 0$ that determines the coupling
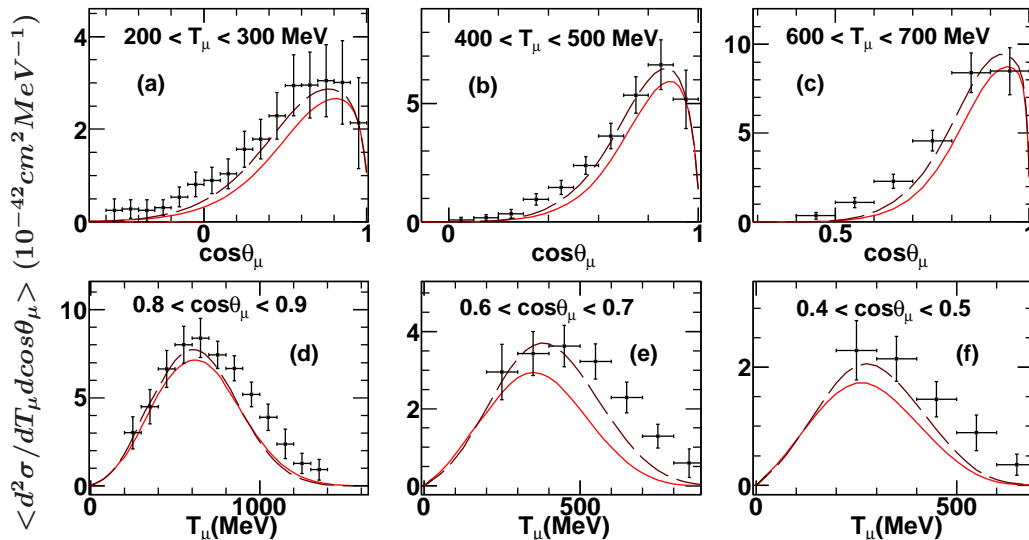
FIGURE 3.15: (Color online) MiniBooNE flux-folded double-differential cross section per target proton for ^{12}C$(\bar{\nu}_\mu, \mu^+)X$. Full (dashed) curves are CRPA with $M_A = 1.03$ GeV ($M_A = 1.35$ GeV). MiniBooNE data are filled squares shown with shape uncertainty which excludes an additional 17.2% normalization uncertainty. The top panels show the $\cos\theta_\mu$ dependence for different ranges of T_μ, while the lower panels give the T_μ dependence for different ranges of $\cos\theta_\mu$.

strength. The two vector form factors are well known from electron-scattering studies [41] and we use a standard dipole parametrization which is a good approximation for the Q^2 values probed in MiniBooNE (Fig. 3.7). The axial form factor, in the dipole form, reads as

$$G_A = \frac{g_A}{\left(1 + \frac{Q^2}{M_A^2}\right)^2} ,\tag{3.10}$$

where g_A is determined from nuclear β decay [42]. The value $M_A = 1.03 \pm 0.02$ GeV is regarded as the world's average value [43–45] emerging from bubble-chamber experiments. Tuning Eq. (3.10) to the shape of the Q^2 distribution of the MiniBooNE ν_μ data [1, 3] favors the value $M_A = 1.35 \pm 0.17$ GeV. In Fig. 3.14, we investigate the sensitivity of the computed CRPA cross sections to the adopted value of M_A. Changing M_A from 1.03 to 1.35 GeV, increases the cross sections by nearly 10%. Note that in Fig. 3.14 we present the normalized cross sections. From the figure, it can be appreciated that modification of M_A affects both the energy distribution and the σ_{CL}/σ_T ratio. Whereas the overall effect of enhancing M_A is a cross section increase, this figure shows that more subtle mechanisms are at play. Enhancing M_A shifts the strength to higher nuclear excitation energies, resulting in a larger impact on the MiniBooNE neutrino than antineutrino cross sections.

In Fig. 3.15, we study the sensitivity of the double-differential flux-folded CRPA cross section to the adopted value of M_A. It can be appreciated that enhancing M_A improves the overall agreement between the CRPA antineutrino cross sections and the data. The enhancement is most pronounced at backward muon scattering but still does not suffice to bring calculations in agreement with data, especially for higher T_μ. As becomes clear from Fig. 3.16, with $M_A = 1.35$ GeV the CRPA results reproduce the data for $T_\mu \leq 600$ MeV well. Under those kinematic
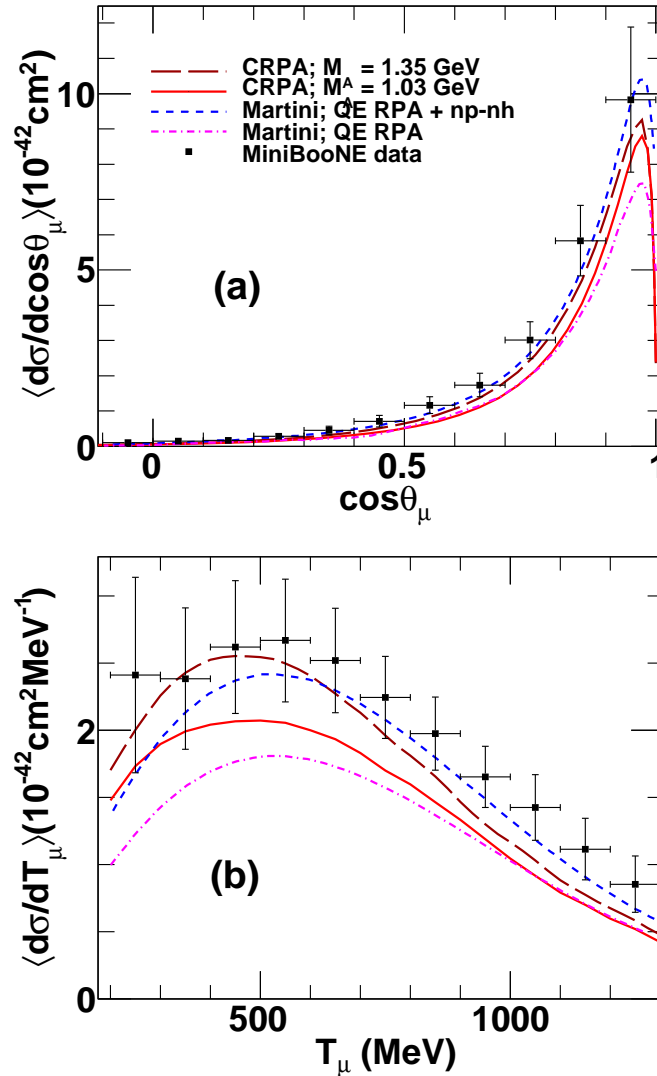
FIGURE 3.16: (Color online) MiniBooNE flux-folded cross section per target proton for ^{12}C$(\bar{\nu}_\mu, \mu^+)X$ as a function of $\cos\theta_\mu$ (a) and of T_μ (b). A comparison is made of the CRPA cross sections with those of Ref. [11] (Martini *et al.*). The MiniBooNE data are integrated over T_μ (a) and over $\cos\theta_\mu$ (b)

.

conditions, the calculations of Ref. [11] tend to underestimate the data. At higher values of T_μ the opposite situation occurs with CRPA underestimating the data. From the comparison in Fig. 3.16, we also find that our CRPA cross sections are larger than the QE RPA predictions from Ref. [11].

The analysis of the MINERνA antineutrino results [7] favors the transverse enhancement model (TEM). In TEM, the magnetic form factors of the bound nucleons are modified in order to account for the enhancement relative to IA predictions, observed in the transverse parts of the electron-nucleus cross sections [46]. We stress that in the analysis of Ref. [7], the TEM and $M_A = 1.35$ GeV models predict comparable cross sections at $Q^2 \lesssim 1$ GeV^2. Accordingly, one can anticipate that for the Q^2 region accessible at MiniBooNE energies (Fig. 3.7), it is difficult to discriminate between the two effective ways of enhancing the computed weak responses.

IV. Conclusions

We have calculated the MiniBooNE flux-folded QE contribution to the ^{12}C-antineutrino cross sections and present the results in terms of the experimentally measured quantities T_μ and $\cos\theta_\mu$. The predictions are made within a nonrelativistic CRPA. The overall agreement between our predictions for the QE contribution to antineutrino scattering cross sections and the MiniBooNE measurements is satisfactory. The best description is reached for lower T_μ. At higher muon kinetic energies and backward scattering angles, the CRPA results underestimate the data. At larger T_μ one observes a significant sensitivity to the choices made with regard to the nucleon-nucleon interaction and the single-particle wave-functions. We observe that the mean-field cross sections in our calculations are in line with the results of [13] and larger than those of Fermi-gas calculations.

As antineutrino cross sections are more sensitive to low-energy nuclear dynamics, an effect that becomes even more pronounced owing to energy distribution of the MiniBooNE antineutrino flux, the effect of RPA correlations is stronger for antineutrinos than for neutrinos. For the MiniBooNE kinematic regime and the very forward scattering dominated neutrino interactions, multinucleon mechanism can be expected to be most important for reactions with a low-energy outgoing lepton. Enhancing M_A enhances the cross sections mostly at higher T_μ and backward scattering angles. Altering M_A has a larger influence on neutrino than on antineutrino cross sections. Still, we observe that in case of antineutrino scattering at MiniBooNE energies, an enhancement in the nucleon axial mass seems to be an effective way of improving the quality of agreement between the CRPA calculations and the data, not only for the size but also for the shape of the double-differential cross section.

Acknowledgments

Bibliography

[1] A.A. Aguilar-Arevalo et al., (MiniBooNE Collaboration), Phys. Rev. D **88**, 032001 (2013).

[2] J.A. Formaggio, and G.P. Zeller, Rev. Mod. Phys. **84**, 1307 (2012).

[3] A.A. Aguilar-Arevalo et al., (MiniBooNE Collaboration), Phys. Rev. D **81**, 092005 (2010).

[4] A.A. Aguilar-Arevalo et al., (MiniBooNE Collaboration), Phys. Rev. D **82**, 092005 (2010).

[5] K. Abe et al., (T2K Collaboration), Phys. Rev. D **87**, 092003 (2013).

[6] G.A. Fiorentini et al., (MINERνA Collaboration), Phys. Rev. Lett. **111**, 022502 (2013).

[7] L. Fields et al., (MINERνA Collaboration), Phys. Rev. Lett. **111**, 022501 (2013).

[8] J.G. Morfin, J. Nieves, and J.T. Sobczyk, Adv. High Energy Phys. **2012**, 934597 (2012).

[9] O. Lalakulich, U. Mosel, and K. Gallmeister, Phys. Rev. C **86**, 054606 (2012).

[10] O. Benhar, P. Coletti, and D. Meloni, Phys. Rev. Lett. **105**, 132301 (2010).

[11] M. Martini, and M. Ericson, Phys. Rev. C **87**, 065501 (2013).

[12] J. Nieves, I. Ruiz Simo, and M.J. Vicente Vacas, Phys. Lett. B **721**, 90-93 (2013).

[13] M.V. Ivanov, R. González-Jiménez, J.A. Caballero, M.B. Barbaro, T.W. Donnelly, and J.M. Udías, Phys. Lett. B **727**, 265 (2013).

[14] J.E. Amaro, M.B. Barbaro, J.A. Caballero, and T.W. Donnelly, Phys. Rev. Lett. **108**, 152501 (2012).

[15] A. Meucci, and C. Giusti, Phys. Rev. D **85**, 093002 (2012).

[16] M. Martini, M. Ericson, G. Chanfray, and J. Marteau, Phys. Rev. C **80**, 065501 (2009).

[17] M. Martini, M. Ericson, and G. Chanfray, Phys. Rev. C **84**, 055502 (2011).

[18] M. Martini, M. Ericson, G. Chanfray, and J. Marteau, Phys. Rev. C **81**, 045502 (2010).

[19] J. Nieves, I. Ruiz Simo, and M.J. Vicente Vacas, Phys. Rev. C **83**, 045501 (2011).

[20] G. Shen, L.E. Marcucci, J. Carlson, S. Gandolfi, and R. Schiavilla, Phys. Rev. C **86**, 035503 (2012).

[21] J.E. Amaro, M.B. Barbaro, J.A. Caballero, T.W. Donnelly, and C. Maieron, Phys. Rev. C **71**, 065501 (2005).

[22] J.E. Amaro, M.B. Barbaro, J.A. Caballero, T.W. Donnelly, and J.M. Udias, Phys. Rev. C **75**, 034613 (2007).

[23] J. Nieves, F. Sánchez, I. Ruiz Simo, and M.J. Vicente Vacas, Phys. Rev. D **85**, 113008 (2012)

[24] N. Jachowicz, K. Heyde, J. Ryckebusch, and S. Rombouts, Phys. Rev. C **59**, 3246 (1999).

[25] N. Jachowicz, K. Heyde, J. Ryckebusch, and S. Rombouts, Phys. Rev. C **65**, 025501 (2002).

[26] J. Ryckebusch, M. Waroquier, K. Heyde, J. Moreau, and D. Ryckbosch, Nucl. Phys. A **476**, 237 (1988).

[27] J. Ryckebusch, K. Heyde, D. Van Neck, and M. Waroquier, Nucl. Phys. A **503**, 694 (1989).

[28] N. Jachowicz, C. Praet, and J. Ryckebusch, Acta Phys. Pol., B **40**, 2559 (2009).

[29] N. Jachowicz, and V. Pandey, proceedings NuInt12, to be published.

[30] J.E. Amaro, M.B. Barbaro, J.A. Caballero, and T.W. Donnelly, Phys. Rev. C **73**, 035503 (2006).

[31] M. Vanhalst, J. Ryckebusch, and W. Cosyn, Phys. Rev. C **86**, 044619 (2012).

[32] S. Janssen, J. Ryckebusch, W. Van Nespen, and D. Debruyne, Nucl. Phys. A **672**, 285 (2000).

[33] M. Waroquier, J. Ryckebusch, J. Moreau, K. Heyde, N. Blasi, S.Y. van de Werf, and G. Wenes, Phys. Rep. **148**, 249 (1987).

[34] G. Có, and S. Krewald, Nucl. Phys. A **433**, 392 (1985).

[35] G. Có, and S. Krewald, Phys. Lett. B **137**, 145 (1984).

[36] M. Martini, M. Ericson, and G. Chanfray, Phys. Rev. D **85**, 093012 (2012).

[37] J.E. Amaro, M.B. Barbaro, J.A. Caballero, T.W. Donnelly, and J.M. Udias, Phys. Rev. D **84**, 033004 (2011).

[38] J. Nieves, I. Ruiz Simo, and M.J. Vicente Vacas, Phys. Lett. B **707**, 72 (2012).

[39] J. Ryckebusch, D. Debruyne, W. Van Nespen, and S. Janssen, Phys. Rev. C **60**, 034604 (1999).

[40] J. Ryckebusch, Phys. Rev. C **64**, 044606 (2001).

[41] H. Budd, A. Bodek, and J. Arrington, Nucl. Phys. B **139**, 90 (2005).

[42] J. Beringer et al., (Particle Data Group), Phys. Rev. D **86**, 010001 (2012).

[43] C. Amsler et al., (Particle Data Group), Phys. Lett. B **667**, 1 (2008).

[44] V. Bernard, L. Elouadrhiri, and U.G. Meissner, J. Phys. G **28**, R1 (2002).

[45] V. Lyubushkin et al., (NOMAD Collaboration), Eur. Phys. J. C **63**, 355 (2009).

[46] A. Bodek, H.S. Budd, and M.E. Christy, Eur. Phys. J. C **71**, 1726 (2011).

3.2 Low-energy excitations and quasielastic contribution to electron-nucleus and neutrino-nucleus scattering in the continuum random phase approximation[2]

V. Pandey, N. Jachowicz, T. Van Cuyck, J. Ryckebusch, M. Martini

Department of Physics and Astronomy, Ghent University,
Proeftuinstraat 86, B-9000 Gent, Belgium.

Abstract

We present a detailed study of a continuum random phase approximation approach to quasielastic electron-nucleus and neutrino-nucleus scattering. We compare the (e, e') cross-section predictions with electron scattering data for the nuclear targets ^{12}C, ^{16}O, and ^{40}Ca, in the kinematic region where quasielastic scattering is expected to dominate. We examine the longitudinal and transverse contributions to ^{12}C(e, e') and compare them with the available data. We find an overall satisfactory description of the (e, e') data. Further, we study the ^{12}C(ν_μ, μ^-) cross sections relevant for accelerator-based neutrino-oscillation experiments. We pay special attention to low-energy excitations which can account for non-negligible contributions in measurements, and require a beyond-Fermi-gas formalism.

I. Introduction

The quest for a completion of our knowledge of neutrino-oscillation parameters has made tremendous progress in recent years. Still, neutrino-oscillation experiments face a number of challenges. Major issues are the identification of the basic processes contributing to the neutrino-nucleus signal in a detector and the reduction of the systematic uncertainties. A thorough understanding of the complexity of the nuclear environment and its electroweak response at low and intermediate energies is required. Charged-current quasielastic (CCQE) processes account for a large share of the detected signals in many experiments. Although several cross section measurements have been performed [1–7], uncertainties connected to the electroweak responses persist [8, 9].

Despite substantial progress in the understanding of the different processes involved in the signal of neutrino-oscillation experiments, the simulation codes are primarily based on a Fermi-gas description of the nucleus. Relativistic Fermi-gas (RFG) based models are employed in Monte Carlo event generators. The RFG model provides a basic picture of the nucleus as a system of quasifree nucleons and takes into account the Fermi motion and Pauli blocking effects. The analysis of electron-scattering data suggests that at momentum transfers $q \approx 500$ MeV/c, the RFG model describes the general behavior of the quasielastic (QE) cross section sufficiently accurately, but its description becomes poor for smaller momentum transfers, where nuclear effects are more prominent. Since the neutrino flux in the oscillation experiments is distributed over energies from very low to a few GeV, the cross section picks up contributions from all energies.

---

[2]This manuscript is published as Phys. Rev. C**92**, 024606 (2015). I performed the numerical calculations, made the figures and drafted the manuscript.

The low excitation-energy cross sections do not receive proper attention in an RFG description. Furthermore, even at higher incoming neutrino energy, the contributions stemming from low transferred energies are not negligible. At low energy transfers, the nuclear structure certainly needs a beyond RFG description. Several studies emphasizing the low energy excitation in the framework of neutrino-nuclear interactions [10–14] have been performed. Those studies, however, have not been explicitly extended to explore the kinematics of MiniBooNE [15], T2K [16], and other similar experiments.

In this paper, we present a continuum random phase approximation (CRPA) approach for the description of QE electroweak scattering off the nucleus, crucial for accelerator-based neutrino-oscillation experiments. We pay special attention to low-energy nuclear excitations. In this context, the availability of a large amount of high-precision electron-nucleus scattering data is of the utmost importance, as it allows one to test the reliability of the reaction model.

Several models have been developed to study electron-nucleus scattering and further generalized to describe neutrino-nucleus cross sections [17–34]. An extensive test against the inclusive quasielastic electron scattering is performed within an RFG and plane-wave impulse approximation approach in Ref. [30], while a spectral function based approach is assessed in Ref. [26]. The model we adopt takes a Hartree-Fock (HF) description of nuclear dynamics as a starting point and additionally implements long-range correlations through a CRPA framework with an effective Skyrme nucleon-nucleon two-body interaction. We solve the CRPA equations by a Green's function approach. Thereby, the polarization propagator is approximated by an iteration of its first-order contribution. In this way, the formalism implements the description of one-particle one-hole excitations out of the correlated nuclear ground state. To improve our description of the kinematics of the interaction at intermediate energies, we implemented an effective relativistic approach proposed in Refs. [27, 28, 35].

The article is organized as follows. In Sec. II, we outline the details of the QE electron and neutrino-nucleus cross-section formalism. We describe the CRPA framework for calculating nuclear responses. Sec. III is divided into two parts: In Sec. III A, we present numerical results of electron-scattering cross sections (on a variety of nuclear targets), and responses (on ^{12}C) and compare them with the available data. In Sec. III B, we discuss neutrino-scattering results in the context of accelerator-based neutrino-oscillation experiments. We pay special attention to low-energy neutrino-induced nuclear excitations. Conclusions can be found in Sec. IV.

II. Formalism

In this section, we describe our CRPA-based approach for the calculation of the nuclear response for inclusive electron and neutrino-nucleus scattering in the QE region. This approach was successful in describing exclusive photo-induced and electron-induced QE processes [36, 37], and inclusive neutrino scattering at supernova energies [38–43]. We have also used this approach to calculate the inclusive CCQE antineutrino-nucleus scattering cross sections at intermediate energies [44]. Here, we are using an updated version of the same formalism.
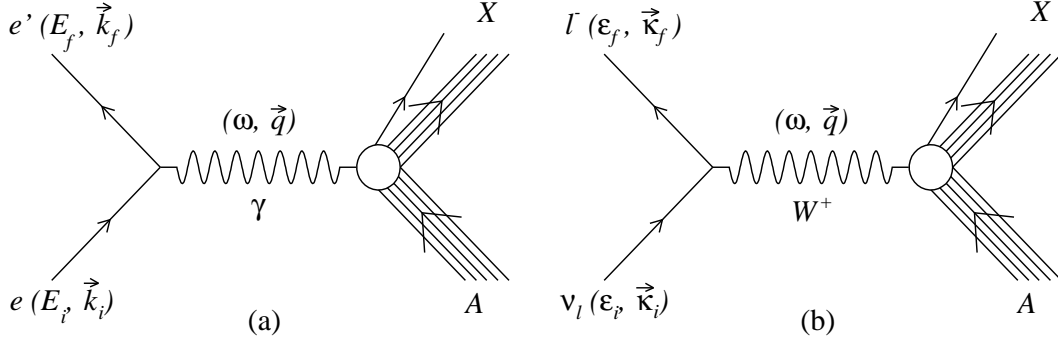
FIGURE 3.17: Inclusive processes considered in this paper: (a) QE electron-nucleus and (b) CCQE neutrino-nucleus ($l = e, \mu, \tau$), where X is the undetected hadronic final state.

We consider QE electron and CCQE neutrino scattering off a nucleus under conditions where the details of the final hadron state remain unobserved. As shown in Fig. 3.17, an incident electron (neutrino) with four-momentum $E_i, \vec{k}_i$ ($\varepsilon_i, \vec{\kappa}_i$) scatters off a nucleus via the exchange of a photon (W-boson) and only the outgoing charged lepton with four-momentum $E_f, \vec{k}_f$ ($\varepsilon_f, \vec{\kappa}_f$) is detected in the final state

$$e(E_i, \vec{k}_i) + A \rightarrow e'(E_f, \vec{k}_f) + X, \tag{3.11}$$

and

$$\nu_l(\varepsilon_i, \vec{\kappa}_i) + A \rightarrow l^-(\varepsilon_f, \vec{\kappa}_f) + X, \tag{3.12}$$

where l represents e, μ, or τ. Further, A is the nucleus in its ground state $|J_i, M_i\rangle$ and X is the unobserved hadronic final state.

The double differential cross section for electron and neutrino-nucleus scattering of Eqs. (3.11) and (3.12) can be expressed as

$$\left(\frac{d^2\sigma}{d\omega d\Omega}\right)_e = \frac{\alpha^2}{Q^4} \left(\frac{2}{2J_i + 1}\right) E_f k_f \cos^2(\theta/2)$$
$$\times \zeta^2\left(Z', E_f, q\right) \left[\sum_{J=0}^{\infty} \sigma_{L,e}^J + \sum_{J=1}^{\infty} \sigma_{T,e}^J\right], \tag{3.13}$$

and

$$\left(\frac{d^2\sigma}{d\omega d\Omega}\right)_\nu = \frac{G_F^2 \cos^2\theta_c}{(4\pi)^2} \left(\frac{2}{2J_i + 1}\right) \varepsilon_f \kappa_f$$
$$\times \zeta^2\left(Z', \varepsilon_f, q\right) \left[\sum_{J=0}^{\infty} \sigma_{CL,\nu}^J + \sum_{J=1}^{\infty} \sigma_{T,\nu}^J\right], \tag{3.14}$$

where α is the fine-structure constant, G_F is the Fermi coupling constant, and θ_c is the Cabibbo angle. The direction of the outgoing lepton is described by the solid angle Ω. The lepton-scattering angle is θ, the transferred four-momentum is $q^\mu(\omega, \vec{q})$ and $Q^2 = -q_\mu q^\mu$. Further, $\zeta(Z', E, q)$ is introduced in order to take into account the distortion of the lepton wave function in the Coulomb field generated by Z' protons, within a modified effective momentum approximation [45].
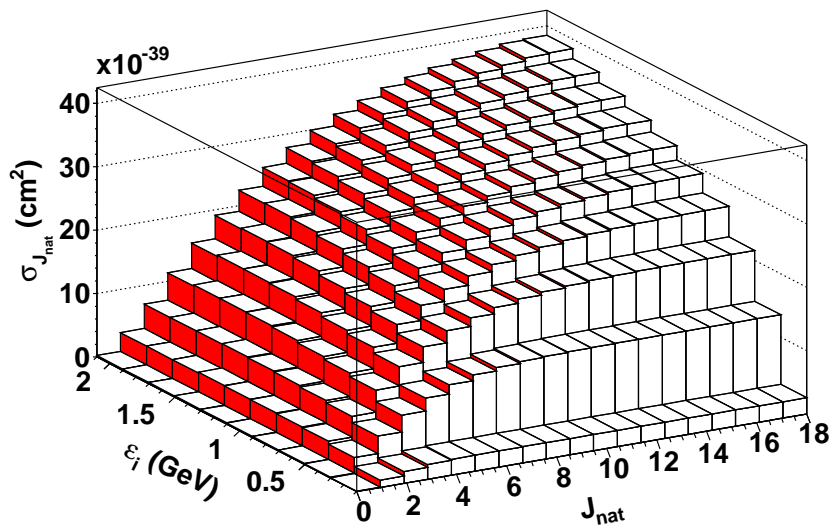
FIGURE 3.18: (Color online) Multipole contributions (for natural parity transitions) to the cross section, as a function of the incoming neutrino energy. The $\sigma_{J_{nat}}$ denotes the ^{12}C(ν_μ, μ^-) cross section including all multipoles of the natural parity excitations up to J_{nat}.

The $\sigma_{L,e}^J$ (J denotes the multipole number) and $\sigma_{T,e}^J$ are the longitudinal and transverse components of the electron-nucleus scattering cross section, while $\sigma_{CL,\nu}^J$ and $\sigma_{T,\nu}^J$ are the Coulomb-longitudinal and transverse contributions of the neutrino-nucleus scattering cross section. In Fig. 3.18, we plot the strength obtained by adding the different multipole contributions to the cross section for incident neutrino energies from 0.1 to 2.0 GeV. Naturally, the higher the energy of the incident particle, the more multipoles contribute to the cross section. From the figure, one observes that for energies as low as 200 MeV, multipoles up to $J = 4$ contribute. For energies as high as 2 GeV, multipoles up to $J =16$ need to be considered, and the relative weight of small J contributions diminishes.

The (Coulomb) longitudinal and transverse parts of the cross section both are composed of a kinematical factor (v) and a response function (R). The response function contains the full nuclear structure information. In the electron scattering case, the longitudinal ($\sigma_{L,e}$) and transverse ($\sigma_{T,e}$) components of the cross section can be expressed as follows

$$\sigma_{L,e} = v_e^L R_e^L, \quad \sigma_{T,e} = v_e^T R_e^T, \tag{3.15}$$

where the leptonic factors, v_e^L and v_e^T, are given by

$$v_e^L = \frac{Q^4}{|\vec{q}|^4}, \quad v_e^T = \left[\frac{Q^2}{2|\vec{q}|^2} + \tan^2(\theta/2) \right]. \tag{3.16}$$

Longitudinal R_e^L and transverse R_e^T response functions are defined as

$$R_e^L = |\langle J_f || \widehat{\mathcal{M}}_J^e(|\vec{q}|) || J_i \rangle|^2, \tag{3.17}$$

$$R_e^T = \left[|\langle J_f || \widehat{\mathcal{J}}_J^{mag,e}(|\vec{q}|)||J_i\rangle|^2 + |\langle J_f || \widehat{\mathcal{J}}_J^{el,e}(|\vec{q}|)||J_i\rangle|^2 \right].$$

(3.18)

Here $\widehat{\mathcal{M}}_J^e$, $\widehat{\mathcal{J}}_J^{mag,e}$ and $\widehat{\mathcal{J}}_J^{el,e}$ are the longitudinal, transverse magnetic and transverse electric operators, respectively [46, 47]. The $|J_i\rangle$ and $|J_f\rangle$ denote the initial and final state of the nucleus.

Similarly for neutrino-scattering processes, we express the Coulomb-longitudinal ($\sigma_{CL,\nu}$) and transverse ($\sigma_{T,\nu}$) parts of the cross section as follows:

$$\sigma_{CL,\nu} = \left[v_\nu^{\mathcal{M}} R_\nu^{\mathcal{M}} + v_\nu^{\mathcal{L}} R_\nu^{\mathcal{L}} + 2 v_\nu^{\mathcal{ML}} R_\nu^{\mathcal{ML}} \right],$$

(3.19)

$$\sigma_{T,\nu} = \left[v_\nu^T R_\nu^T + 2 v_\nu^{TT} R_\nu^{TT} \right],$$

(3.20)

where leptonic coefficients $v_\nu^{\mathcal{M}}$, $v_\nu^{\mathcal{L}}$, $v_\nu^{\mathcal{ML}}$, v_ν^T, and v_ν^{TT} are given as

$$v_\nu^{\mathcal{M}} = \left[1 + \frac{\kappa_f}{\varepsilon_f} \cos\theta \right],$$

(3.21)

$$v_\nu^{\mathcal{L}} = \left[1 + \frac{\kappa_f}{\varepsilon_f} \cos\theta - \frac{2\varepsilon_i \varepsilon_f}{|\vec{q}|^2} \left(\frac{\kappa_f}{\varepsilon_f} \right)^2 \sin^2\theta \right],$$

(3.22)

$$v_\nu^{\mathcal{ML}} = \left[\frac{\omega}{|\vec{q}|} \left(1 + \frac{\kappa_f}{\varepsilon_f} \cos\theta \right) + \frac{m_l^2}{\varepsilon_f |\vec{q}|} \right],$$

(3.23)

$$v_\nu^T = \left[1 - \frac{\kappa_f}{\varepsilon_f} \cos\theta + \frac{\varepsilon_i \varepsilon_f}{|\vec{q}|^2} \left(\frac{\kappa_f}{\varepsilon_f} \right)^2 \sin^2\theta \right],$$

(3.24)

$$v_\nu^{TT} = \left[\frac{\varepsilon_i + \varepsilon_f}{|\vec{q}|} \left(1 - \frac{\kappa_f}{\varepsilon_f} \cos\theta \right) - \frac{m_l^2}{\varepsilon_f |\vec{q}|} \right],$$

(3.25)

and response functions $R_\nu^{\mathcal{M}}$, $R_\nu^{\mathcal{L}}$, $R_\nu^{\mathcal{ML}}$, R_ν^T, and R_ν^{TT} are defined as

$$R_\nu^{\mathcal{M}} = |\langle J_f || \widehat{\mathcal{M}}_J^\nu(|\vec{q}|)||J_i\rangle|^2,$$

(3.26)

$$R_\nu^{\mathcal{L}} = |\langle J_f || \widehat{\mathcal{L}}_J^\nu(|\vec{q}|)||J_i\rangle|^2,$$

(3.27)

$$R_\nu^{\mathcal{ML}} = \mathcal{R} \left[\langle J_f || \widehat{\mathcal{L}}_J^\nu(|\vec{q}|)||J_i\rangle \langle J_f || \widehat{\mathcal{M}}_J^\nu(|\vec{q}|)||J_i\rangle^* \right],$$

(3.28)

$$R_\nu^T = \left[|\langle J_f || \widehat{\mathcal{J}}_J^{mag,\nu}(|\vec{q}|)||J_i\rangle|^2 + |\langle J_f || \widehat{\mathcal{J}}_J^{el,\nu}(|\vec{q}|)||J_i\rangle|^2 \right],$$
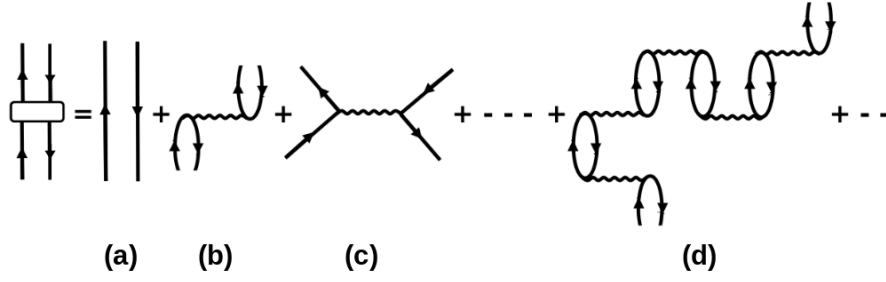
(3.29)

FIGURE 3.19: Diagrammatic representation of the polarization propagator $\Pi^{(RPA)}$ for particle-hole states. Panel (a) corresponds to the unperturbed polarization propagator $\Pi^{(0)}$, (b) and (c) are the first-order direct and exchange RPA diagrams, and (d) represents a typical higher-order RPA diagram.

$$R_\nu^{TT} = \mathcal{R} \left[\langle J_f || \widehat{\mathcal{J}}_J^{mag,\nu}(|\vec{q}|) || J_i \rangle \langle J_f || \widehat{\mathcal{J}}_J^{el,\nu}(|\vec{q}|) || J_i \rangle^* \right] .$$

(3.30)

Here $\widehat{\mathcal{M}}_J^\nu$, $\widehat{\mathcal{L}}_J^\nu$, $\widehat{\mathcal{J}}_J^{mag,\nu}$ and $\widehat{\mathcal{J}}_J^{el,\nu}$ are the Coulomb, longitudinal, transverse magnetic, and transverse electric operators, respectively [46, 47].

To calculate the nuclear response functions, we use the CRPA approach which is described in detail in Refs. [36–39]. Here we will briefly present the essence of our model. We start by describing the nucleus within a mean-field (MF) approximation. The MF potential is obtained by solving the Hartree-Fock (HF) equations with a Skyrme (SkE2) two-body interaction [36, 37]. The sequential filling of the single-nucleon orbits automatically introduces Pauli-blocking. The continuum wave functions are obtained by integrating the positive-energy Schrödinger equation with appropriate boundary conditions. In this manner, we account for the final-state interactions of the outgoing nucleon. Once we have bound and continuum single-nucleon wave functions, we introduce the long-range correlations through a CRPA approach. We solve the CRPA equations with a Green's function formalism. The RPA describes a nuclear excited state as the linear combination of particle-hole (ph^{-1}) and hole-particle (hp^{-1}) excitations out of a correlated ground state

$$|\Psi_{RPA}^C\rangle = \sum_{C'} \left[X_{C,C'} \ |p'h'^{-1}\rangle - \ Y_{C,C'} \ |h'p'^{-1}\rangle \right] ,$$

(3.31)

where C denotes the full set of quantum numbers representing an accessible channel. The Green's function approach allows one to treat the single-particle energy continuum exactly by treating the RPA equations in coordinate space. The RPA polarization propagator, obtained by the iteration of the first-order contributions to the particle-hole Green's function, is written as

$$\Pi^{(RPA)}(x_1, x_2; E_x) = \Pi^{(0)}(x_1, x_2; E_x)$$
$$+\frac{1}{\hbar} \int dx dx' \Pi^0(x_1, x; E_x) \tilde{V}(x, x') \Pi^{(RPA)}(x', x_2; E_x),$$

(3.32)

where E_x is the excitation energy of the target nucleus and x is a shorthand notation for the combination of the spatial, spin and isospin coordinates. The $\Pi^{(0)}$ in Eq. (3.32) corresponds to
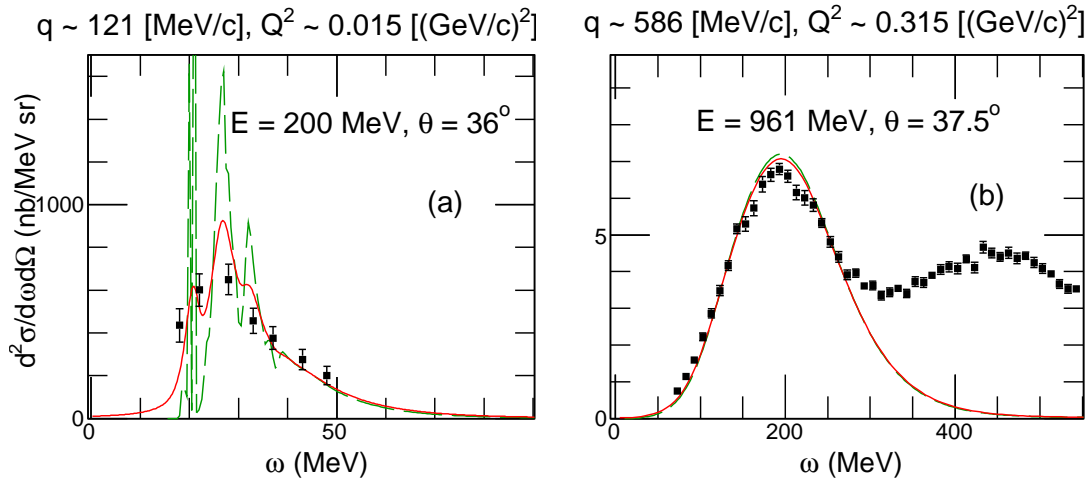
FIGURE 3.20: (Color online) Comparison of ^{12}C(e, e') cross sections obtained with (full line) and without (dashed lines) the folding method. The experimental data are from (a) [51] and (b) [53].

the HF contribution to the polarization propagator and $\tilde{V}$ denotes the antisymmetrized nucleon-nucleon interaction. The HF responses can be retrieved by switching off the second term in the above equation. Fig. 3.19 shows different components contributing to the polarization propagator.

A limitation of the RPA formalism is that the configuration space is restricted to 1p-1h excitations. As a result only the escape-width contribution to the final-state interaction is accounted for and the spreading width of the particle states is neglected. This affects the description of giant resonances in the CRPA formalism. The energy location of the giant resonance is generally well predicted but the width is underestimated and the height of the response in the peak is overestimated. In order to remedy this, several methods have been proposed such as the folding procedure of Refs. [12, 28, 48, 49]. Here, we use a simplified phenomenological approach where the modified response functions $R'(q, \omega')$ are obtained after folding the HF and CRPA response functions $R(q, \omega)$:

$$R'(q, \omega') = \int_{-\infty}^{\infty} d\omega \; R(q, \omega) \; L(\omega, \omega'), \tag{3.33}$$

with (L) a Lorentzian

$$L(\omega, \omega') = \frac{1}{2\pi} \left[\frac{\Gamma}{(\omega - \omega')^2 + (\Gamma/2)^2} \right]. \tag{3.34}$$

We use an effective value of $\Gamma = 3$ MeV which complies well with the predicted energy width in the giant-resonance region [48], where one expects the effect of the folding to be most important. The overall effect of folding is a redistribution of strength from peak to the tails. In line with the conclusions drawn in Refs. [12, 20], the energy integrated response functions are not much affected by the folding procedure of Eq. (3.33). In Fig. 3.20, we compare the (e, e') cross sections obtained with and without folding. Figure 3.20 (a) clearly shows that in the giant-resonance region, the adopted folding procedure spreads the strength over a wider ω range, thereby considerably improving the quality of agreement with the data. At higher ω (Fig. 3.20 (b)) the effect of the folding is marginal. All computed cross-section results shown in the paper adopt the folding procedure of Eq. (3.33).
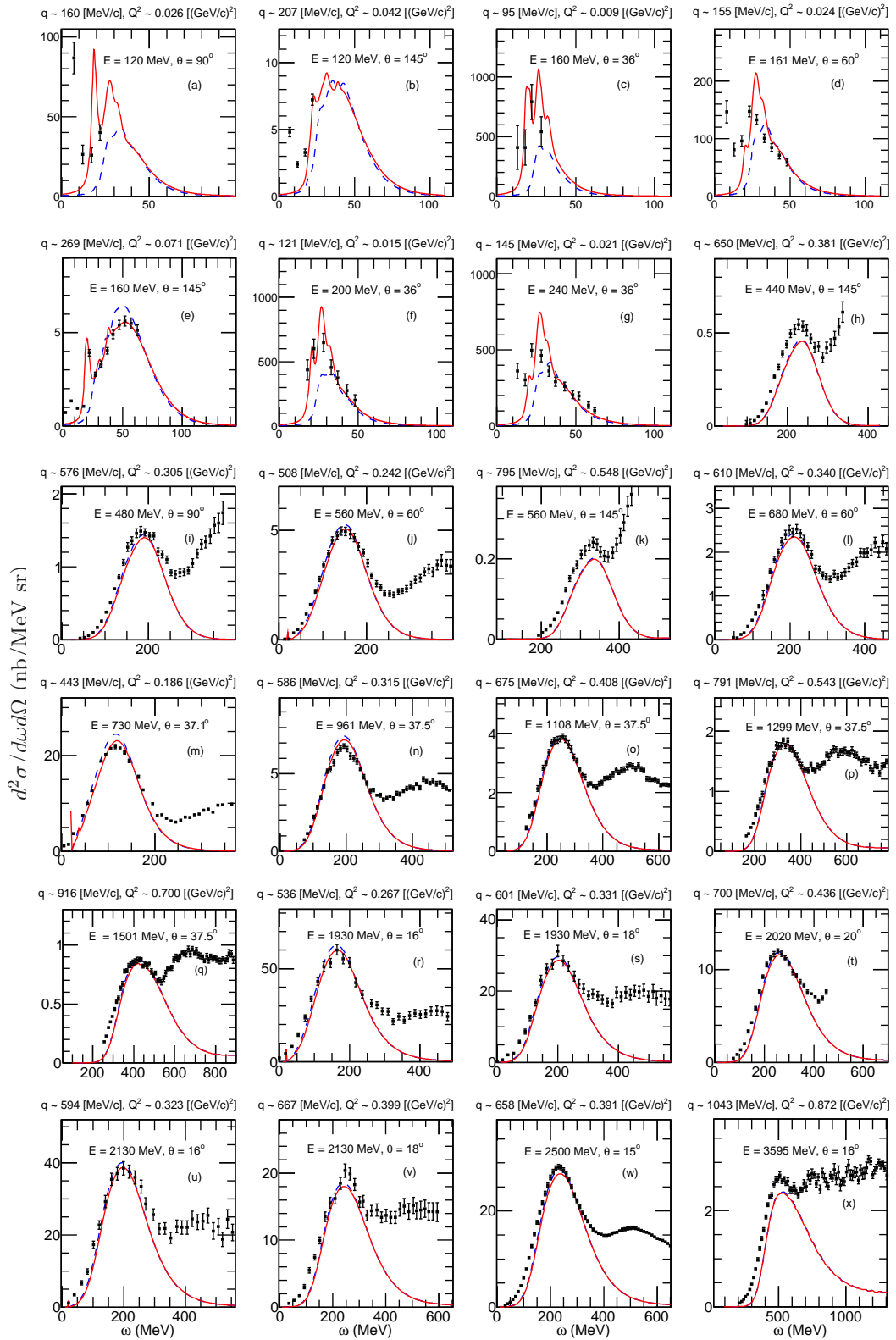
FIGURE 3.21: (Color online) The double differential cross section for ^{12}C(e,e'). CRPA (solid lines) and HF (dashed-lines) cross sections are compared with the data of Refs. [51–56]. The q and Q^2 values, on top of each panel, are calculated at quasielastic conditions $Q^2/(2M_N\omega) = 1$, with M_N the nucleon mass.

Our approach is self-consistent because we use the same SkE2 interaction in both the HF and CRPA equations. The parameters of the momentum-dependent SkE2 force are optimized against ground-state and low-excitation energy properties [50]. Under those conditions the virtuality Q^2 of the nucleon-nucleon vertices is small. At high virtualities Q^2, the SkE2 force tends to be unrealistically strong. We remedy this by introducing a dipole hadronic form factor at the nucleon-nucleon interaction vertices

$$V(Q^2) \rightarrow V(Q^2 = 0) \frac{1}{(1 + \frac{Q^2}{\Lambda^2})^2} \tag{3.35}$$

where we introduced the free cut-off parameter Λ. We adopt Λ = 455 MeV, a value which is optimized in a χ^2 test of the comparison of $A(e, e')$ CRPA cross sections with the experimental data of Refs. [51–58]. In the χ^2 test, we consider the theory-experiment comparison from low values of omega up to the maximum of the quasielastic peak. We have restricted our fit to the low-ω side of the quasielastic peak, because the high-ω side is subject to corrections stemming from intermediate Δ excitation, which is not included in our model.

The influence of the nuclear Coulomb field on the lepton is taken into account by means of an effective momentum approximation (EMA) [45]. In order to take into account the reduced lepton wavelength, the three-momentum transfer is enhanced in an effective way

$$q_{eff} = q + 1.5 \left(\frac{Z' \alpha \hbar c}{R} \right), \tag{3.36}$$

where $R = 1.24 \ A^{1/3}$ fm. The lepton wave functions are modified accordingly

$$\Psi_l^{eff} = \zeta(Z', E, q) \ \Psi_l \tag{3.37}$$

with

$$\zeta(Z', E, q) = \sqrt{\frac{q_{eff} E_{eff}}{qE}}, \tag{3.38}$$

where E (E_{eff}) is the energy (effective energy) of the outgoing lepton.

Our description of the nuclear dynamics is based on a nonrelativistic framework. For $q > 500$ MeV/c, the momentum of the emitted nucleon is comparable with its rest mass, and relativistic effects become important. We have implemented relativistic corrections in an effective fashion, as suggested in Refs. [27, 28, 35]. Those references show that a satisfactory description of relativistic effects can be achieved by following kinematic substitution in the nuclear response

$$\lambda \rightarrow \lambda (1 + \lambda), \tag{3.39}$$

where $\lambda = \omega/2M_N$ and M_N is the nucleon mass. The above substitution produces a reduction of the width of the one-body responses and a shift in the peak towards smaller values of ω. The correction becomes sizable for $q \gtrsim 500$ MeV/c.

III. Results

To test our model, we start with the calculation of (e, e') cross sections on different nuclei and the response functions for electron scattering off ^{12}C, in subsection III A. We confront our numerical results with the data of Refs. [51–59]. We discuss the neutrino-scattering results in subsection III B.

A. Electron scattering

In this subsection, we present our results for the QE $A(e, e')$ cross sections. For any given E_i, the nuclear response depends on q^μ. Energy transfers below the particle knockout threshold result in nuclear excitations in discrete states. At slightly higher energies, the giant dipole resonance (GDR) shows up. Only at substantially higher energy one can distinguish the peak corresponding to QE one-nucleon knockout. In an ideal case, if an electron scatters from a free nucleon, one would expect a narrow peak at $\omega = Q^2/2M_N$. Deviations from that peak are due to the nuclear dynamics. The heavier the target nucleus, the wider the peak. The shift of the peak is due to nuclear binding and correlations.

For the two vector form factors entering in the responses, we use the standard dipole parametrization of Ref. [60]. In Fig. 3.21 we present results of our numerical calculations for ^{12}C(e, e'). We compare CRPA and HF predictions with the measurements performed at the Saclay Linear Accelerator [51], Bates Linear Accelerator Center [52], Stanford Linear Accelerator Center [53, 55], Yerevan electron synchrotron [54], and DESY [56]. The comparison is performed over a broad range of three- and four-momentum transfers: $95 \lesssim q \lesssim 1050$ MeV/c, and $0.009 \lesssim Q^2 \lesssim 0.900$ (GeV/c)^2. Our predictions are reasonably successful in describing the data over the broad kinematical range considered here. Moreover, they compare favorably with the cross-section results of Refs. [26, 30]. The interesting feature of our results is the prediction of the nuclear excitations at small energy ($\omega < 50$ MeV) and momentum transfers ($q < 300$ MeV/c), well below the QE peak. This feature can be appreciated in Figs. 3.21(a)-3.21(g). The HF and CRPA $A(e, e')$ cross sections are identical for $Q^2 \gtrsim 0.25$ (GeV/c)^2. The cross section drops by two orders of magnitude with the shift in scattering angle from $36°$ to $145°$, for a fixed energy, as evident from Figs. 3.21(c)-3.21(e) for an incoming energy of 160 MeV. Even for higher incoming electron energies the cross-section measurements at smaller scattering angles are still dominated by QE processes. Obviously, the measured cross sections include contributions from channels beyond QE, like Δ-excitations, evident as the second peak in the data, and 2p-2h contributions. Our description is restricted to QE processes and further work is in progress on the role of processes beyond QE ones [61].

The double differential ^{16}O(e, e') cross sections are shown in Fig. 3.22. Our numerical calculations reasonably describe the QE parts of the measurements performed at ADONE [57] and at the Bates Linear Accelerator Center [52]. Further, the calculations for the heavier target ^{40}Ca are presented in Fig. 3.23. Again, the comparison with the experimental data taken at Bates Linear Accelerator Center [58] is fair.
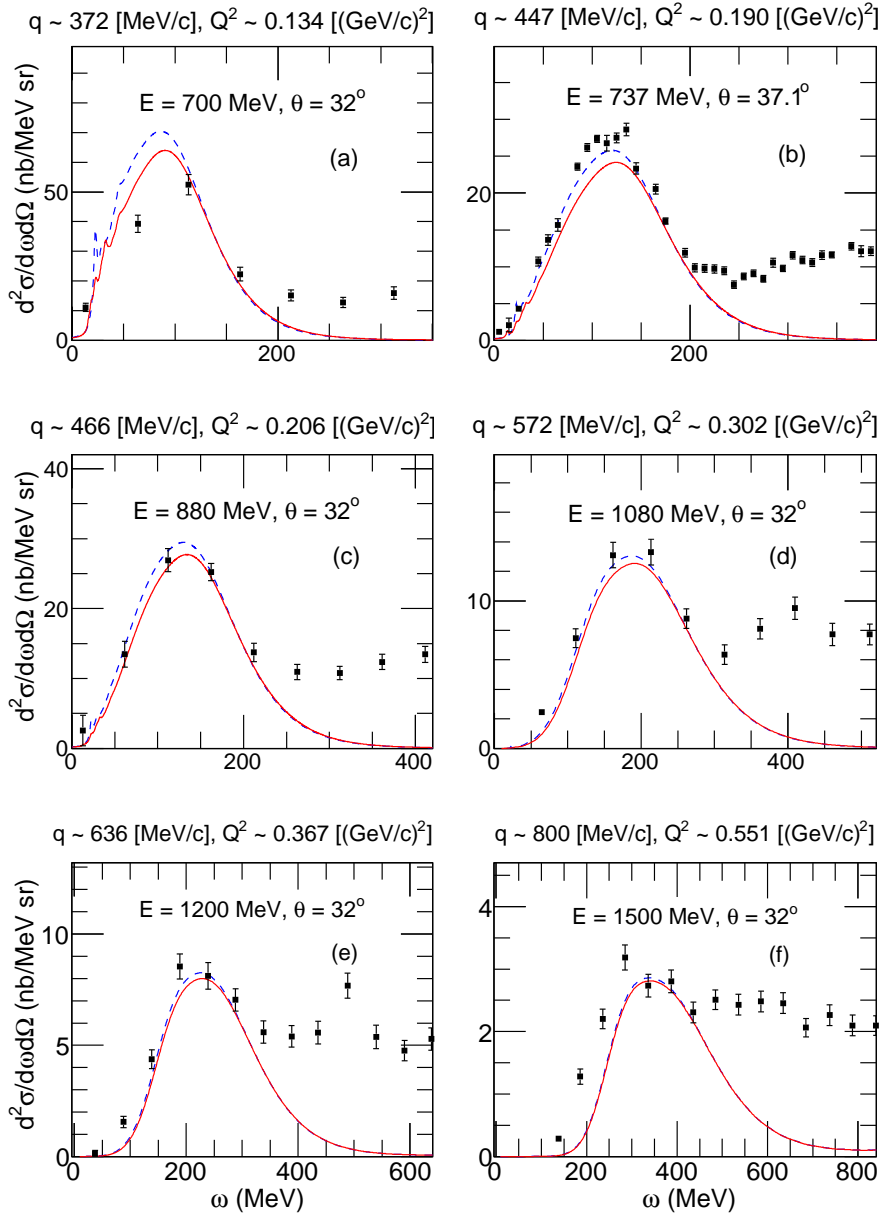
FIGURE 3.22: (Color online) As in Fig. 3.21 but for ^{16}O(e, e'). The data are from Refs. [52, 57].
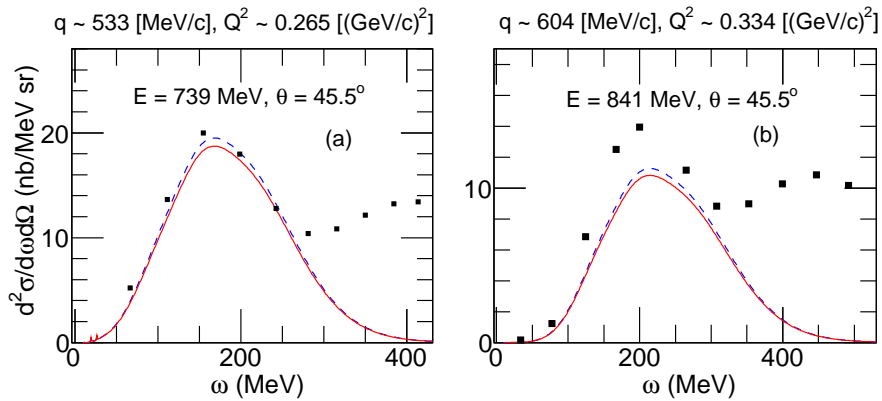

FIGURE 3.23: (Color online) Same as Figs. 3.21 and 3.22 but on a ^{40}Ca target, the measurements are from Ref. [58].
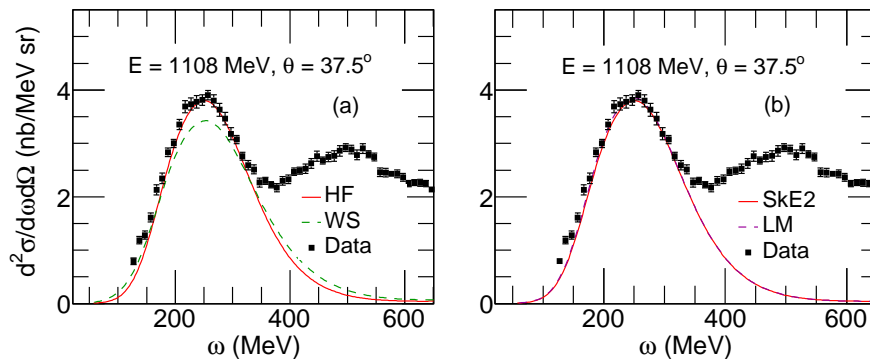
FIGURE 3.24: (Color online) Comparison of cross sections obtained (on ^{12}C) (a) with the HF and WS single-particle wave functions with SKE2 as residual interaction and (b) with the SKE2 and LM residual interaction with HF as single-particle wave functions.

In Fig. 3.24 we compare cross sections obtained with two different parametrizations of the single-nucleon wave functions and nucleon-nucleon residual interactions. The Landau Migdal (LM) [62] and SKE2 [37, 50] yield similar cross sections while the use of the Woods-Saxon (WS) [34] wave function slightly shifts and reduces the strength of the cross section. This can be attributed to the fact that the HF wave functions have larger high-momentum components than the WS ones.

The (e, e') cross section receives contributions from the longitudinal and transverse components, as can be seen in Eq. (3.13). A separation of these two response functions provides further detail about the target dynamics. It is worth mentioning that the experimental values of responses are extracted from a set of cross-section measurements using a Rosenbluth separation [63]. The data of Ref. [59] is determined by a reanalysis of the world data on (e, e') cross sections. Interestingly, that resulted in a significant difference from the measurements of Ref. [51], as can be seen in Fig. 3.25(b). The comparison between our predictions on ^{12}C with the experimental data of Refs. [51, 59] is quite satisfactory. The longitudinal responses are overestimated and the transverse responses are usually underestimated. Our predictions are in line with those predicted in Ref. [59] and with the continuum shell model predictions of Ref. [64]. It is long known, that the inclusion of processes involving meson exchange current (MEC) are needed to account for the transverse strength of the electromagnetic response [65, 66]. The calculations carried out on light nuclei overwhelmingly suggest that single-nucleon knockout processes, such as in this work, are dominant in the longitudinal channel while in the transverse channel two-nucleon processes provide substantial contributions.

B. Neutrino scattering

The calculation of ^{12}C(ν_l, l^-) response functions involve two vector form factors and one axial form factor. We use the BBBA05 parametrization of Ref. [67] for the two vector form factors, and the standard dipole parametrization of the axial form factor with $M_A = 1.03 \pm 0.02$ GeV [68–70].

In Fig. 3.26 we display different contributions to the total ^{12}C(ν_μ, μ^-) cross section, as a function of the incoming neutrino energy. The axial contribution is larger than the vector one. Related to this, neutrino cross sections are dominated by the transverse current.
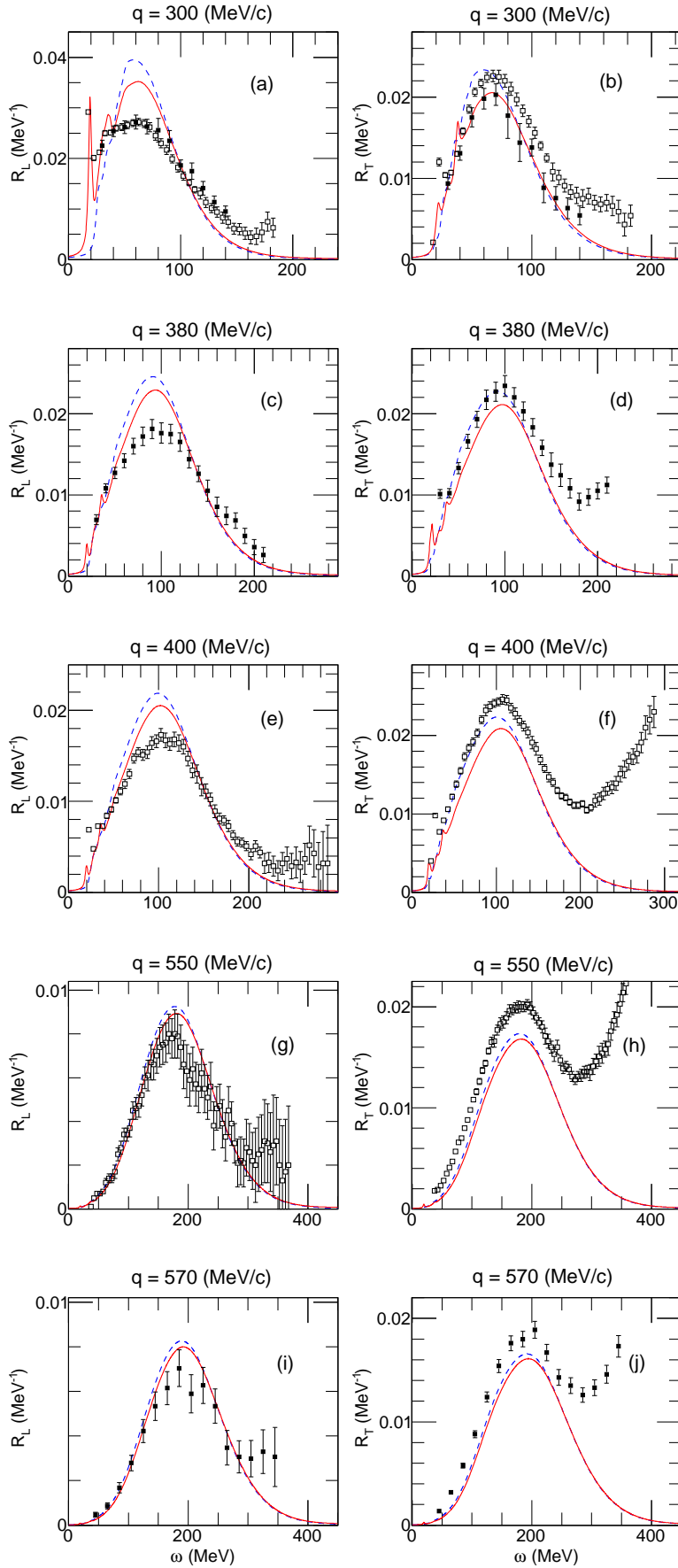
FIGURE 3.25: (Color online) Longitudinal and transverse responses for $^{12}C(e, e')$, for different values of q. Solid lines are CRPA predictions and dashed lines are HF predictions. Experimental data are from Ref. [59] (filled squares) and Ref. [51] (open squares).
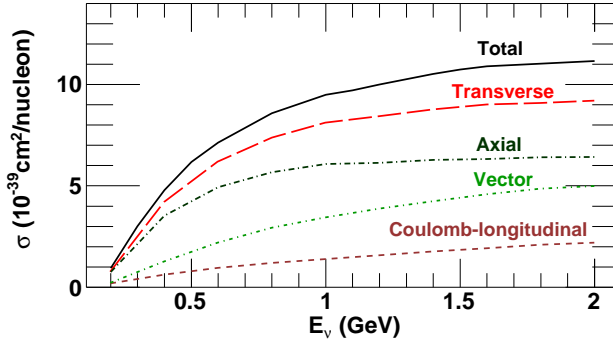
FIGURE 3.26: (Color online) Different contributions to the total ^{12}C(ν_μ, μ^-) cross section (per neutron) as a function of incoming neutrino energy. The sum of transverse and Coulomb-longitudinal (axial and vector) is the total cross section.
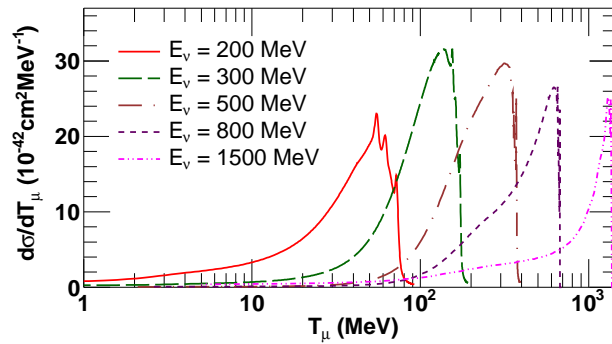
FIGURE 3.27: (Color online) Cross section for ^{12}C(ν_μ, μ^-) as a function of outgoing muon kinetic energy T_μ, for different incoming neutrino energies. Note the log scale on the horizontal axis.
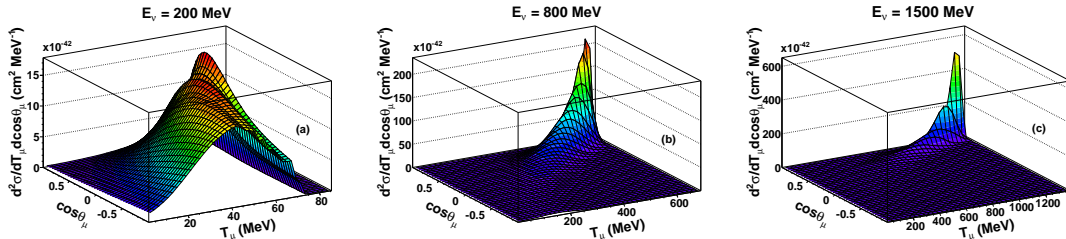

FIGURE 3.28: (Color online) Double differential ^{12}C(ν_μ, μ^-) cross sections plotted as a function of T_μ and $\cos\theta_\mu$, for three neutrino energies.

Electron-scattering cross-section measurements are typically performed for a fixed incoming electron energy and scattering angle. As neutrinos are produced as the secondary products of a decaying primary beam, the interacting neutrino's energy is not sharply defined. The initial neutrino energy is reconstructed using the kinematics of the final outgoing lepton. This is a major source of uncertainty whereby nuclear structure can have an important influence.

The neutrino flux in oscillation experiments typically covers a wide energy range from about 100 MeV to a few GeV. The cross section measured at a single energy and scattering angle of the outgoing lepton picks up contributions from scattering processes at different energies, with varying weights. In Fig. 3.27, we show the differential cross section (in outgoing muon energy) for $200 \lesssim E_\nu \lesssim 1500$ MeV. It is evident from the figure that with increasing E_ν the strengths of
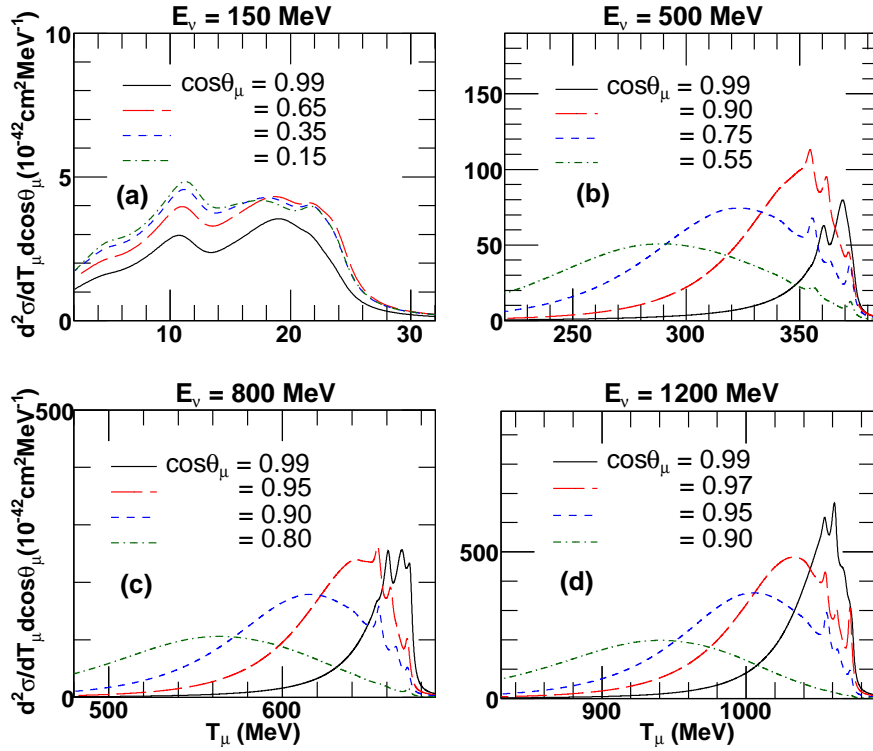
FIGURE 3.29: (Color online) Low-energy excitations in double differential cross sections for ^{12}C(ν_μ, μ^-) plotted as a function of T_μ, for different $\cos\theta_\mu$ values.
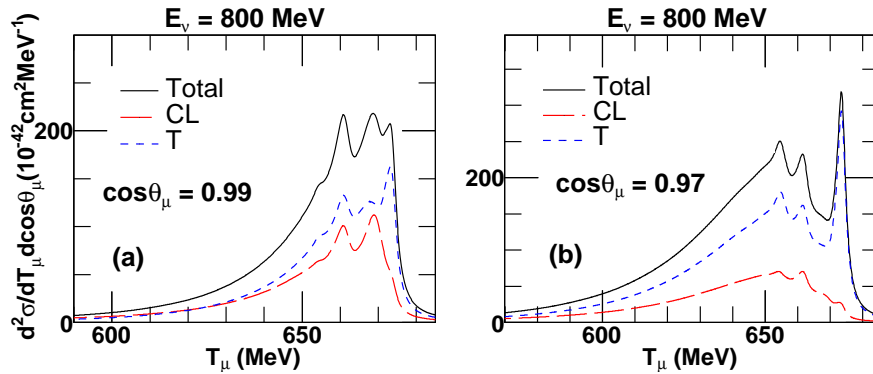

FIGURE 3.30: (Color online) Coulomb-longitudinal (CL) and transverse (T) contributions to the double differential cross sections, at $E_\nu = 800$ MeV and two values of $\cos\theta_\mu$.

the cross sections shift in muon energy. Also, there is a clear signature of the low-ω excitations even at neutrino energies around the peak of the MiniBooNE and T2K ν_μ spectra.

The measured cross sections are flux-folded double differential in outgoing muon kinetic energy T_μ and scattering angle $\cos\theta_\mu$. To illustrate the low-energy excitations and general behavior of double differential ^{12}C(ν_μ, μ^-) cross sections at fixed energies, we display in Fig. 3.28 the double differential cross sections for $E_\nu = 200$, 800, and 1500 MeV. With the increase in incoming neutrino energy, the strength shifts in the forward direction and the width of giant resonances reduces. In Fig. 3.29, we plot the double differential cross section at different fixed values of $\cos\theta_\mu$. For $E_\nu = 150$ MeV, the double differential cross section is dominated by low-lying nuclear excitations, as evident from Fig. 3.29(a). For neutrino energies around the mean energy

of the MiniBooNE [1] and T2K [6] fluxes, $E_\nu = 800$ MeV [Fig. 3.29(c)], the nuclear collective excitations are still sizable at forward muon scattering angles. The same feature is still visible for very forward scattering off neutrinos with an energy of 1200 MeV [Fig. 3.29(d)]. The contribution of collective excitations to neutrino-nucleus responses can not be accounted for within the RFG-based simulation codes. As evident from the results presented here, they can account for non-negligible contributions to the signal even at higher neutrino energies.

In Fig. 3.30, we show the transverse and Coulomb-longitudinal contribution to the double differential cross sections. For $\cos\theta_\mu = 0.99$, the Coulomb-longitudinal contribution of the quasielastic cross section is comparable to the transverse one. The transverse contribution dominates the cross section as soon as one moves away from the very forward direction. This feature along with the giant-resonance contribution to forward-scattering cross sections accounts for most of the strength at very small momentum transfers. Theoretical models, which do not predict this behavior, tend to underestimate the cross section for forward-scattering angles, as discussed in Ref. [71].

IV. Conclusions

We presented a detailed discussion of CRPA predictions for quasielastic electron-nucleus and neutrino-nucleus responses.

We assessed inclusive quasielastic electron-nucleus cross sections on ^{12}C, ^{16}O, and ^{40}Ca. We consider momentum transfers over the broad range $95 \lesssim q \lesssim 1050$ MeV/c in combination with energy transfers which favor the quasielastic nucleon-knockout reaction process. We confronted our predictions with high-precision electron-scattering data. We separated the longitudinal and transverse responses on ^{12}C, for $300 \lesssim q \lesssim 570$ MeV/c, and compared them with the data. A reasonable overall description of the data, especially those corresponding with low-energy nuclear excitations, is reached.

We calculated ^{12}C(ν_μ, μ^-) cross sections, relevant for accelerator-based neutrino-oscillation experiments. We illustrated how low-energy nuclear excitations are induced by neutrinos. We paid special attention to contributions where nuclear-structure details become important, but remain unobserved in RFG-based models. We show that low-energy excitations can account for non-negligible contributions to the signal of accelerator-based neutrino-oscillation experiments, especially at forward neutrino-nucleus scattering.

Acknowledgments

Bibliography

[1] A. A. Aguilar-Arevalo et al., (MiniBooNE Collaboration), Phys. Rev. D**81**, 092005 (2010).

[2] A. A. Aguilar-Arevalo et al., (MiniBooNE Collaboration), Phys. Rev. D**88**, 032001 (2013).

[3] A. A. Aguilar-Arevalo et al., (MiniBooNE Collaboration), Phys. Rev. D**82**, 092005 (2010).

[4] G. A. Fiorentini et al., (MINERvA Collaboration), Phys. Rev. Lett. **111**, 022502 (2013).

[5] L. Fields et al., (MINERvA Collaboration), Phys. Rev. Lett. **111**, 022501 (2013).

[6] K. Abe et al., (T2K Collaboration), Phys. Rev. D**87**, 092003 (2013).

[7] K. Abe et al., (T2K Collaboration), arXiv:1407.4256[hep-ex].

[8] J. G. Morfin, J. Nieves, and J. T. Sobczyk, Adv. High Energy Phys. **2012**, 934597 (2012).

[9] L. Alvarez-Ruso, Y. Hayato, J. Nieves, New J. Phys. **16**, 075015 (2014).

[10] E. Kolbe, K. Langanke, F. K. Thielemann, and P. Vogel, Phys. Rev. C **52**, 3437 (1995).

[11] C. Volpe, N. Auerbach, G. Colo, T. Suzuki, and N. Van Giai, Phys. Rev. C **62**, 015501 (2000).

[12] A. Botrugno, and G. Co', Nucl. Phys. **A761**, 200 (2005).

[13] M. Martini, G. Co', M. Anguiano, and A. M. Lallena, Phys. Rev. C **75**, 034604 (2007).

[14] A. R. Samana, F. Krmpotic, N. Paar, C. A. Bertulani, Phys. Rev. C **83**, 024303 (2011).

[15] http://www-boone.fnal.gov/

[16] http://t2k-experiment.org/

[17] W. M. Alberico, M. Ericson, and A. Molinari, Nucl. Phys. A **379**, 429 (1982).

[18] M. Martini, M. Ericson, G. Chanfray, and J. Marteau, Phys. Rev. C **80**, 065501 (2009).

[19] M. Martini, J. Phys. Conf. Ser. **408**, 012041 (2013).

[20] A. Gil, J. Nieves, and E. Oset, Nucl. Phys. A **627**, 543 (1997).

[21] J. Nieves, J. E. Amaro, and M. Valverde, Phys. Rev. C **70**, 055503 (2004).

[22] J. Nieves, M. Valverde, and M. J. Vicente Vacas, Phys. Rev. C **73**, 025504 (2006).

[23] O. Benhar, A. Fabrocini, S. Fantoni, and I. Sick, Nucl. Phys. A **579**, 493 (1994).

[24] O. Benhar, N. Farina, H. Nakamura, M. Sakuda, and R. Seki, Phys. Rev. D **72**, 053005 (2005).

[25] H. Nakamura, T. Nasu, M. Sakuda, and O. Benhar, Phys. Rev. C **76**, 065208 (2007).

[26] A. M. Ankowski, O. Benhar, and M. Sakuda, Phys. Rev. D **91**, 033005 (2015).

[27] J. E. Amaro, M. B. Barbaro, J. A. Caballero, T. W. Donnelly, and C. Maieron, Phys. Rev. C**71**, 065501 (2005).

[28] J. E. Amaro, M. B. Barbaro, J. A. Caballero, T. W. Donnelly, and J. M. Udias, Phys. Rev. C**75**, 034613 (2007).

[29] T. Leitner, O. Buss, L. Alvarez-Ruso, and U. Mosel, Phys. Rev. C **79**, 034601 (2009).

[30] A. V. Butkevich, and S. P. Mikheyev, Phys. Rev. C **72**, 025501 (2005).

[31] A. V. Butkevich, and S. A. Kulagin, Phys. Rev. C **76**, 045502 (2007).

[32] A. Meucci, F. Capuzzi, C. Giusti, and F. D. Pacati, Phys. Rev. C **67**, 054601 (2003).

[33] A. Meucci, C. Giusti, and F. D. Pacati, Nucl. Phys. A **739**, 277 (2004).

[34] G. Co', and S. Krewald, Phys. Lett. B**137**, 145 (1984).

[35] S. Jeschonnek, T. W. Donnelly, Phys. Rev. C**57**, 2438 (1998).

[36] J. Ryckebusch, M. Waroquier, K. Heyde, J. Moreau, and D. Ryckbosch, Nucl. Phys. A**476**, 237 (1988).

[37] J. Ryckebusch, K. Heyde, D. Van Neck, and M. Waroquier, Nucl. Phys. A**503**, 694 (1989).

[38] N. Jachowicz, S. Rombouts, K. Heyde, and J. Ryckebusch, Phys. Rev. C**59**, 3246 (1999).

[39] N. Jachowicz, K. Heyde, J. Ryckebusch, and S. Rombouts, Phys. Rev. C**65**, 025501 (2002).

[40] N. Jachowicz, K. Vantournhout, J. Ryckebusch, and K. Heyde, Phys. Rev. Lett. **93**, 082501 (2004).

[41] N. Jachowicz, G. C. McLaughlin, Phys. Rev. Lett. **96**, 172301 (2006).

[42] N. Jachowicz, C. Praet, and J. Ryckebusch, Acta Physica Polonica B **40**, 2559 (2009).

[43] N. Jachowicz, and V. Pandey, AIP Conf. Proc. **1663**, 050003 (2015).

[44] V. Pandey, N. Jachowicz, J. Ryckebusch, T. Van Cuyck, and W. Cosyn, Phys. Rev. C**89**, 024601 (2014).

[45] J. Engel, Phys. Rev. C**57**, 2004 (1998).

[46] J. S. O'Connell, T. W. Donnelly, and J. D. Walecka, Phys. Rev. C**6**, 719 (1972).

[47] J. D. Walecka, *Theoretical Nuclear and Subnuclear Physics* (Oxford University Press, New York, 1995).

[48] R. D. Smith, J. Wambach, Phys. Rev. C**38**, 100 (1988).

[49] A. De Pace, and M. Viviani, Phys. Rev. C**48**, 2931 (1993).

[50] M. Waroquier, J. Ryckebusch, J. Moreau, K. Heyde, N. Blasi, S. .Y. Van de Werf and G. Wenes, Phys. Rept. 148, 249 (1987).

[51] P. Barreau *et al.*, Nucl. Phys. A**402**, 515 (1983).

[52] J. S. O'Connell *et al.*, Phys. Rev. C**35**, 1063 (1987).

[53] R. M. Sealock *et al.*, Phys. Rev. Lett.**62**, 1350 (1989).

[54] D. S. Bagdasaryan *et al.*, YERPHI-1077-40-88 (1988).

[55] D. B. Day *et al.*, Phys. Rev. C **48**, 1849 (1993).

[56] D. Zeller, DESY-F23-73-2 (1973).

[57] M. Anghinolfi *et al.*, Nucl. Phys. A**602**, 405 (1996).

[58] C. F. Williamson*et al.*, Phys. Rev. C**56**, 3152 (1997).

[59] J. Jourdan, Nucl. Phys. A**603**, 117 (1996).

[60] E. J. Beise, and R. D. McKeown, Comments Nucl. Part. Phys., **20**, 105 (1991).

[61] T. Van Cuyck, N. Jachowicz, M. Martini, V. Pandey, J. Ryckebusch, in preparation.

[62] G. Có, and S. Krewald, Nucl. Phys. A **433**, 392 (1985).

[63] M. N. Rosenbluth, Phys. Rev. **79**, 615 (1950).

[64] J. E. Amaro, G. Co', A. .M. Lallena, arXiv:9902072 [nucl-th].

[65] T. W. Donnelly, J. W. Van Orden, T. De Forest, Jr., and W. C. Hermans, Phys. Lett. B **76**, 393 (1978).

[66] W. M. Alberico, M. Ericson, and A. Molinari, Ann. Phys. **154**, 356 (1984).

[67] R. Bradford, A. Bodek, H. Budd, and J. Arrington, Nucl. Phys. Proc. Suppl. **159**, 127 (2006).

[68] J. Beringer et al., (Particle Data Group), Phys. Rev. D **86**, 010001 (2012).

[69] C. Amsler et al., (Particle Data Group), Phys. Lett. **667B**, 1 (2008).

[70] V. Bernard, L. Elouadrhiri, and U. G. Meissner, J. Phys. G **28**, R1 (2002).

[71] M. Martini, M. Ericson, Phys. Rev. C **90**, 025501 (2014).

3.3 CRPA approach to charged-current quasielastic neutrino-nucleus scatterings at MiniBooNE and T2K kinematics [3]

V. Pandey[1], N. Jachowicz[1], M. Martini[1,2], R. González-Jiménez[1], J. Ryckebusch[1],
T. Van Cuyck[1], N. Van Dessel[1]

[1]Department of Physics and Astronomy, Ghent University,
Proeftuinstraat 86, B-9000 Gent, Belgium.

[2]ESNT, CEA-Saclay, DSM, IRFU, Service de Physique Nucléaire,
F-91191 Gif-sur-Yvette Cedex, France.

Abstract

We present continuum random phase approximation (CRPA) results for charged-current quasielastic (CCQE) neutrino-nucleus scattering at kinematics relevant for the MiniBooNE and T2K experiments. We calculate flux-folded double differential cross sections off ^{12}C and compare them with MiniBooNE and with the off-axis T2K measurements. The CRPA predictions describe the gross features of the measured cross sections. They slightly underpredict the data because of the absence of processes beyond pure quasielastic scattering in our model. With the CRPA model's ability to describe the low-energy nuclear excitations, we particularly analyze the flux-folded double-differential cross sections for the most forward muon scattering angular bins. At these kinematics, the flux-folded cross sections receive non-negligible contributions from low-energy nuclear excitations.

I. Introduction

The study of neutrino oscillations is moving into an era of precision with an intense enhancement in the activities of accelerator-based neutrino-oscillation experiments. Substantial progress is made in the determination of the mass-squared differences and mixing angles in $\nu_\mu \to \nu_e$ measurements. However, in order to improve the precision of the analysis, a rigorous description of neutrino-nucleus cross sections is required. The progress and issues related to the cross sections in this context was recently reviewed in Refs. [1, 2].

In recent years, the MiniBooNE collaboration has presented an extensive set of cross-section measurements [3–9], while T2K reported on cross sections measured with the off-axis near detector (ND280) [10, 11]. The primary objective of both experiments is to make precise oscillation measurements in the ν_μ disappearance and ν_e appearance channel. The challenges faced in these efforts, and especially those related to the neutrino-nucleus signal in the detector, need detailed microscopic neutrino-interaction models that can describe the variety of nuclear effects over the broad kinematical range probed. A thorough comparison of the cross-section measurements with

---

[3]This manuscript is in progress. I performed numerical calculations, made figures and drafted the manuscript.

theoretical predictions is crucial to asses the role of nuclear effects in the target's response and to reduce the systematic uncertainties in the extraction of the oscillation parameters.

In this work, we aim at discussing the results of calculations for the charged-current (CC) neutrino scattering on ^{12}C, at the kinematics of the MiniBooNE and T2K experiments. One of the major objectives of this work is the investigation of the role of neutrino-induced low-energy nuclear collective excitations in MiniBooNE and T2K's signal. To this end we adapt a continuum random phase approximation (CRPA) model.

The CRPA model was originally developed to describe exclusive electron- and photo-induced nucleon knockout reactions [12, 13]. The model was later used to predict neutrino scattering at supernova energies both in charged-current (CC) and neutral-current (NC) reactions [14–17]. The formalism was further extended to the QE reaction region [18, 19] and successfully tested against electron scattering data for a variety of nuclear targets [20]. Here, we briefly summarize the essence of our model. The starting point of the description of the nuclear dynamics is a mean field (MF) approximation. We solve the Hartree-Fock (HF) equations using a Skyrme (SkE2) nucleon-nucleon interaction [13, 21]. Once the bound and continuum single-nucleon wave functions are determined, long-range correlation are introduced by means of a CRPA approach based on a Green's function formalism. The CRPA describes an excited state as a linear combination of particle-hole (ph^{-1}) and hole-particle (hp^{-1}) excitations out of a correlated nuclear ground state

$$|\Psi_{RPA}^C\rangle = \sum_{C'} \left[X_{C,C'} \ |p'h'^{-1}\rangle - \ Y_{C,C'} \ |h'p'^{-1}\rangle \right] \ , \tag{3.40}$$

where C represents the full set of quantum numbers of an accessible single-nucleon knockout channel. The RPA polarization propagator $\Pi^{(RPA)}$ is obtained by the iteration of the first order contributions to the particle-hole Green's function $\Pi^{(0)}$ and is obtained as the solution to the equation

$$\Pi^{(RPA)}(x_1, x_2; E_x) = \Pi^{(0)}(x_1, x_2; E_x)$$
$$+ \frac{1}{\hbar} \int dx dx' \Pi^0(x_1, x; E_x) \tilde{V}(x, x') \Pi^{(RPA)}(x', x_2; E_x), \tag{3.41}$$

where E_x is the excitation energy of the target nucleus and x is a shorthand notation for the combination of the spatial, spin and isospin coordinates. The $\Pi^{(0)}$ in Eq. (3.41) corresponds to the HF contribution to the polarization propagator and $\tilde{V}$ denotes the antisymmetrized nucleon-nucleon SkE2 interaction.

The SkE2 interaction was optimized against ground state and low-excitation properties of spherical nuclei. Its strength is in its ability to describe nuclear excitation in the few 10s of MeV energy range. In order to restrain the SkE2 force from becoming unrealistically strong at high virtuality Q^2, a dipole hadronic form factor is introduced at the nucleon-nucleon interaction vertices [20]. The same SkE2 two-body interaction, that is used to solve the HF equations, is used to calculate the CRPA polarization propagator. The continuum wave functions are obtained by solving
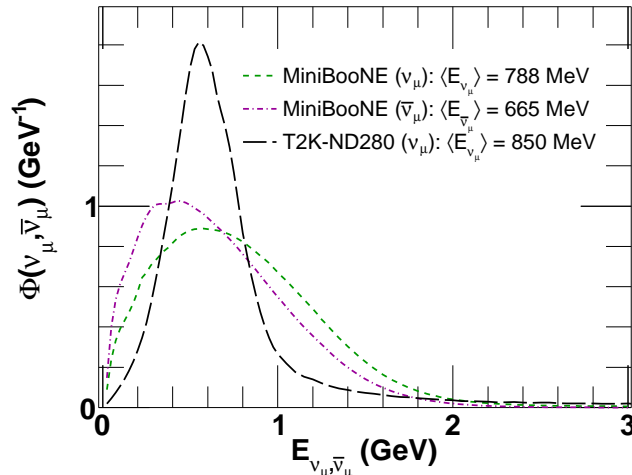
FIGURE 3.31: (Color online) Normalized MiniBooNE ν_μ [3], $\bar{\nu}_\mu$ [8] and T2K [10] (off-axis ND280) ν_μ fluxes.

the positive-energy Schrödinger equation with appropriate boundary conditions. Hence, the distortion effects (escape width) from the residual nucleons on the outgoing nucleon is taken into account. A folding procedure is used to take into account also the spreading width of the particles states [20], which makes the description of giant resonances more realistic within the CRPA approach. In order to consider the influence of the nuclear Coulomb field on the outgoing lepton, a modified effective momentum approximation (MEMA) [22] is used. Further, to improve our description at higher momentum transfers, we have implemented relativistic kinematic corrections [24]. The world-averaged axial mass value $M_A = 1.03$ GeV was used for all the calculations in this paper.

The article is organized as follows. Sec. II is divided in three parts: We compare the flux-folded double-differential CRPA cross sections with the measurements of MiniBooNE and T2K in Sec. II A. In order to asses the contributions stemming from low-energy nuclear excitations, we discuss the specific case of forward muon scattering bins in Sec. II B. In Sec. II C, we show flux-unfolded total cross section. The conclusions are presented in Sec. III.

II. Cross section analysis

Both MiniBooNE and T2K use a target rich in ^{12}C. Their fluxes [3, 8, 10] are slightly different, as shown in Fig 3.31. Both ν_μ beams have average energies around 800 MeV while the $\bar{\nu}_\mu$ MiniBooNE beam has a slightly lower average energy. The T2K beam, however, is definitely sharper peaked, and receives less contributions beyond 1 GeV than the MiniBooNE one.

A. Flux-folded double differential cross section

We present CC pure QE neutrino cross sections folded with MiniBooNE flux in Fig. 3.32. The top panels are plotted as a function of the muon scattering angle $\cos\theta_\mu$ for several bins of muon
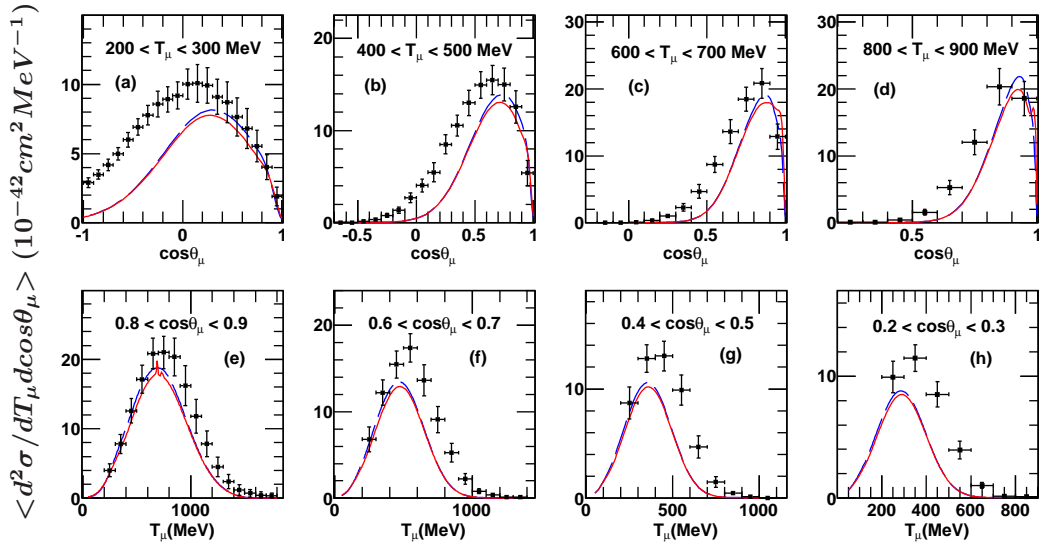
FIGURE 3.32: (Color online) MiniBooNE flux-folded double-differential cross sections per target neutron for ^{12}C$(\nu_\mu, \mu^-)X$, plotted as a function of $\cos\theta_\mu$ for different T_μ values (top) and as a function of T_μ for different ranges of $\cos\theta_\mu$ (bottom). Solid curves are CRPA and dashed curves are HF results. MiniBooNE data with shape uncertainties are taken from Ref. [3]. The data contain an additional normalization uncertainty of 10.7%, not included here.
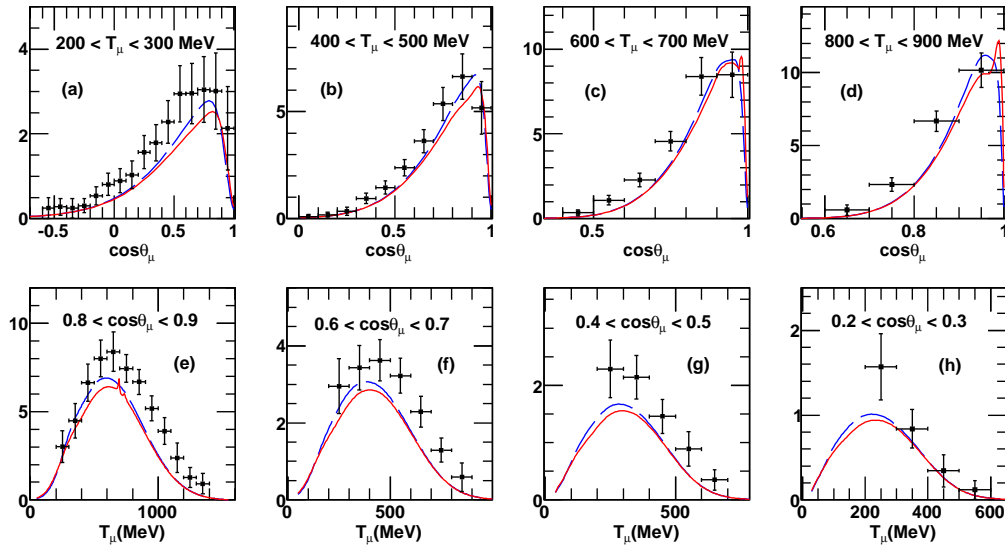

FIGURE 3.33: (Color online) Same as Fig. 3.32 but for the process ^{12}C$(\bar{\nu}_\mu, \mu^+)X$. Solid curves are CRPA and dashed curves are HF calculations. MiniBooNE data with shape uncertainties are taken from Ref. [8]. The data contain an additional normalization uncertainty of 17.4%, not included here.
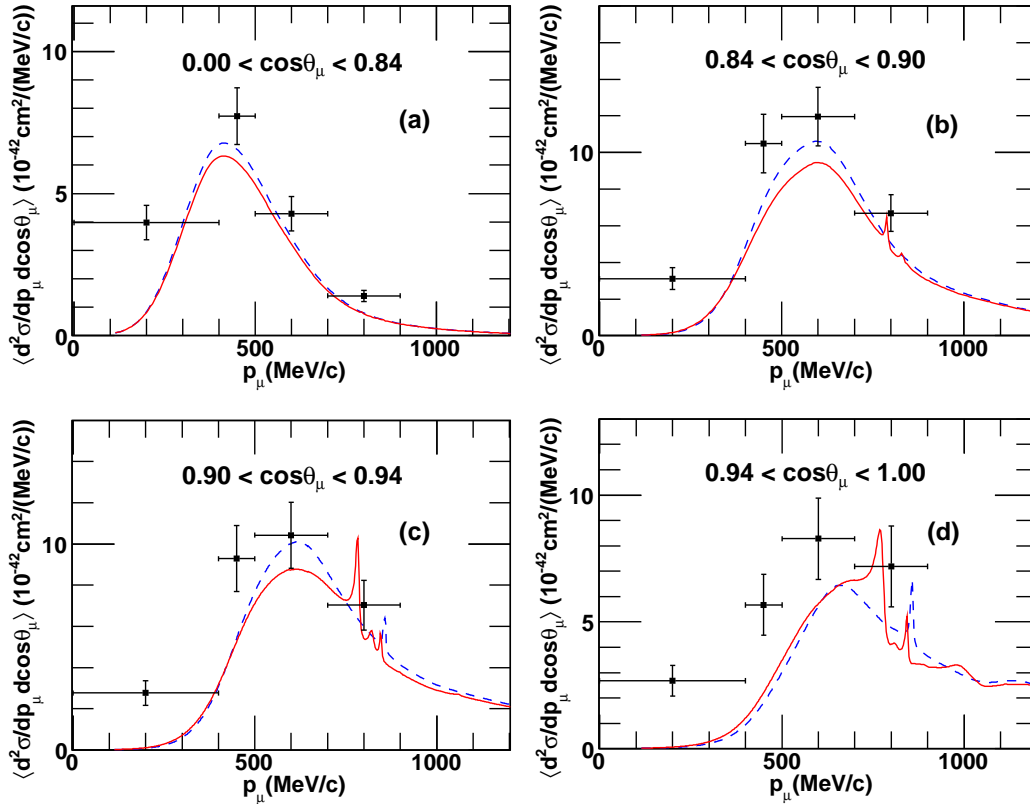
FIGURE 3.34: (Color online) T2K flux-folded inclusive CC double-differential cross sections per target nucleon on ^{12}C plotted as a function of muon momentum p_μ, for different bins of $\cos\theta_\mu$. CRPA (solid curves) and HF (dashed-curves) are compared with T2K measurements of [10].

kinetic energies T_μ and the bottom panels are plotted as function of T_μ for different ranges for $\cos\theta_\mu$. The calculated cross sections are averaged over the T_μ and $\cos\theta_\mu$ ranges. We compare HF and CRPA calculations with the experimental data of MiniBooNE [3]. The HF and CRPA cross sections reproduce the shape of the cross sections. In the top panels, the CRPA cross sections are slightly higher than the HF ones for $\cos\theta_\mu$ approaching 1, indicating the extra contributions stemming from low-energy excitations. The agreement between CRPA and data is reasonably sound for forward scattering but underestimates the data for more backward (and suppressed) scattering cross sections. The measurement of CCQE neutrino [3] and antineutrino [8] cross sections by the MiniBooNE collaboration sparked off discussions about the nuclear effects active in the broad energy range covered by the flux. Note that the CCQE(-like) cross section in MiniBooNE is defined as the process where one muon and no pions are observed in the final state. Corrections to genuine QE processes stem from multinucleon correlations in the target nuclei. Those multinucleon processes (like meson-exchange currents (MEC), Δ-isobar currents and short-range correlations) give rise to additional sources of strength in the nuclear response. First, correction to the single-nucleon knockout channel, and second non-vanishing strength in multinucleon knockout [23]. The necessity to include multinucleon effects to successfully describe the CCQE MiniBooNE data, has been confirmed by several independent models [25–36]. As expected, the fact that multinucleon channels are not included in the current work, results in an underestimation of the data. In Fig. 3.33, we compare our flux-folded predictions for antineutrino
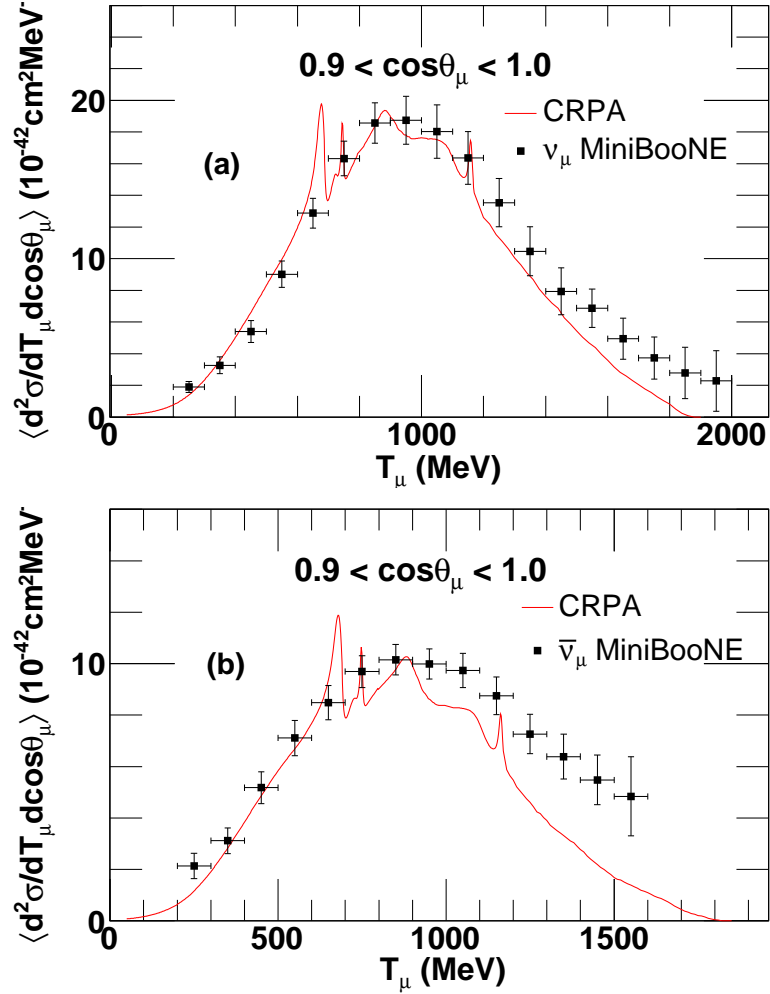
FIGURE 3.35: (Color online) CCQE double-differential cross sections per target neutron folded with MiniBooNE flux, for the bin $0.9 < \cos\theta_\mu < 1.0$ plotted as a function of T_μ. CRPA calculations are compared with MiniBooNE data of Ref. [3, 8]. Experimental error bars represent the shape uncertainties.

cross sections with the MiniBooNE measurements of Ref. [8]. In this case, the CRPA predictions are closer to the MiniBooNE data than those for the neutrino calculations. This again confirms that the role of multinucleon excitations is more important for neutrino than for antineutrino case.

The T2K collaboration reported on CC-inclusive double-differential cross sections as a function of muon momentum p_μ and scattering angle $\cos\theta_\mu$ [10], and CCQE total cross sections as a function of incident neutrino energies [11]. So far, the published T2K inclusive CC cross section do not separate different reaction channels. As a consequence, the inelastic processes beyond QE such as multinucleon excitations, pion production and absorption channels are contributing to the signal. Ref. [38] finds a satisfactory agreement with the T2K data, after inclusion of multinucleon and single-pion production channels. On the other hand, the relativistic Green's functions (RGF) approach of Ref. [39], which successfully describes the MiniBooNE data, underestimates the T2K results. Another comparison is presented in the superscaling approach of Ref. [40].
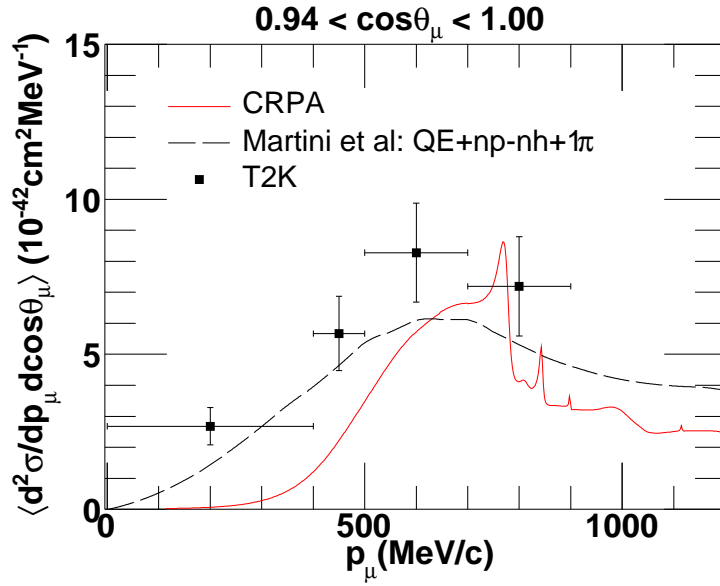
FIGURE 3.36: (Color online) The most forward bin, $0.94 < \cos\theta_\mu < 1.0$, of Fig 3.34, where CRPA cross sections are compared with the calculations of Martini *et al* [38]. T2K data are taken from Ref. [10].
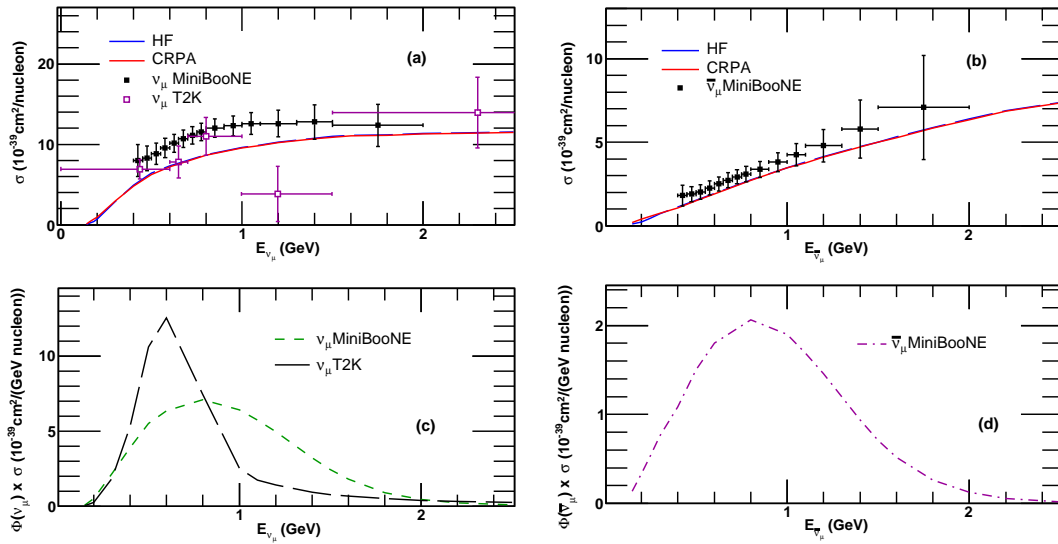

FIGURE 3.37: (Color online) Total CCQE (a) $^{12}C(\nu_\mu, \mu^-)X$ ((b)$^{12}C(\bar{\nu}_\mu, \mu^+)X)$ cross sections per target neutron plotted as a function of (anti)neutrino energy. The experimental data are taken from MiniBooNE neutrino [3], T2K neutrino [11] and MiniBooNE antineutrino [8]. Panel (c) and (d) represents the total neutrino and antineutrino cross sections multiplied by MiniBooNE and T2K fluxes of Fig. 3.31.

We have computed the T2K ν_μ flux-folded QE double-differential cross sections. The HF and CRPA results are confronted with the data in Fig. 3.34. The cross sections are averaged over each $\cos\theta_\mu$ bin. CRPA cross sections reproduce the gross feature of the T2K data, but underestimate the data, as can be expected in absence of effects beyond QE. The underestimation is more pronounced for smaller value of p_μ, which corresponds to the higher excitation energies where the inelastic channels beyond QE can be expected to have substantial contributions. The interesting feature of our results is the extra strength stemming from the presence of the low-energy nuclear collective excitations, specially in panel (c) and (d), corresponding to more forward scattering directions.

B. Forward scattering cross section

In Ref. [20], we stressed the importance of low-energy nuclear excitations for the forward muon scattering events in MiniBooNE and T2K ν_μ. Here we compare the most forward bin of the MiniBooNE and T2K data sets to explore the contributions emerging from the low-energy excitations in these experiments. The majority of the cross section strength in this kinematic region, where excitation energy of the nucleus is $\lesssim 50$ MeV, arises from the collective nuclear excitation effects. Thereby, the longitudinal response is the major source of strength while the transverse contributions are suppressed. Models that do not include collective effects can be expected to underestimate the data at small scattering angles. The most forward angular bin, $0.94 < \cos\theta_\mu < 1$, in the RGF predictions of T2K in Ref. [39] significantly underestimates the data compared to the other energy bins. The same bin in Ref. [38], even after the inclusion of multinucleon and one pion production channels, which predicts the data successfully in other angular bins, lacks strength specially for $600 < p_\mu < 800$ (MeV/c).

In Fig. 3.35 we compare our results for $0.90 < \cos\theta_\mu < 1$ with the MiniBooNE measurements. The cross section is averaged over the bin range. The flux-folded cross section retains signatures of low-energy nuclear excitations. In Fig. 3.36, we compare CRPA calculations for the most forward bin ($0.94 < \cos\theta_\mu < 1$) with the experimental data of T2K [10] and with the calculations of Ref. [38]. For $0 < p_\mu < 600$ (MeV/c), the calculations of Ref. [38] that include the contribution of np-nh and the one-pion production channel are reasonably well in agreement with the data and the CRPA calculations underestimate the data. But for $600 < p_\mu < 800$ (MeV/c), the CRPA calculations provide the strength missing in the calculations of Ref. [38]. This hints at the importance of the low-energy nuclear excitations in the most forward MiniBooNE and T2K measurements.

C. Total QE cross section

In Fig 3.37, we compare the computed CCQE $^{12}C(\nu_\mu, \mu^-)X$ and $^{12}C(\bar\nu_\mu, \mu^+)X$ total cross-section with the data of MiniBooNE [3, 8] and T2K [11]. Unlike the double-differential ones, the total experimental cross sections are model dependent. The experimental data are shown as a function of reconstructed energy while the theoretical results as a function of true energy. On average, in panel (a), the strength of MiniBooNE measurements is higher than the T2K 'QE-like' one. The measurement of these two data sets are quite comparable except the neutrino energy bin of 1

- 1.5 GeV. The CRPA calculations are within the error bar of the T2K data, but underpredict the MiniBooNE ones. The CRPA results agree much better with antineutrino measurement of MiniBooNE, in panel (b), where the CRPA predictions are within the error bars of the data. The HF and CRPA cross sections in both, neutrino and antineutrino, case are almost coinciding with each other except for E < 250 MeV.

III. Conclusions

We have calculated ν_μ-^{12}C and $\bar{\nu}_\mu$-^{12}C responses in kinematics corresponding with the Mini-BooNE and T2K experiments. The CRPA cross sections compare favorable to the shape but underestimate the MiniBooNE data for backward muon scattering angles. The missing strength can be associated with the contribution emerging from multinucleon knockout processes that are not included in CRPA here. However, for the most forward bin of MiniBooNE, $0.90 < \cos\theta_\mu < 1.0$, the CRPA cross section reproduces the data reasonably well, due to the extra strength arising from low-energy nuclear excitations. CRPA also predicts the gross features of the inclusive CC data of T2K. The inclusion of multinucleon and single-pion production processes is essential to produce the full strength of the data. However, for the most forward bin, $0.94 < \cos\theta_\mu < 1.0$ the nuclear excitations seem to have a non-negligible contribution in the cross sections. We also compared the MiniBooNE and T2K flux-folded double-differential cross sections for fixed forward scatterings.

Acknowledgments

Bibliography

[1] J. G. Morfin, J. Nieves, and J. T. Sobczyk, Adv. High Energy Phys. **2012**, 934597 (2012).

[2] L. Alvarez-Ruso, Y. Hayato, and J. Nieves, New J. Phys. **16**, 075015 (2014).

[3] A. A. Aguilar-Arevalo et al. (MiniBooNE Collaboration), Phys. Rev. D **81**, 092005 (2010).

[4] A. A. Aguilar-Arevalo et al. (MiniBooNE Collaboration), Phys. Rev. D **81**, 013005 (2010).

[5] A. A. Aguilar-Arevalo et al. (MiniBooNE Collaboration), Phys. Rev. D **82**, 092005 (2010).

[6] A. A. Aguilar-Arevalo et al. (MiniBooNE Collaboration), Phys. Rev. D **83**, 052007 (2011).

[7] A. A. Aguilar-Arevalo et al. (MiniBooNE Collaboration), Phys. Rev. D **83**, 052009 (2011).

[8] A. A. Aguilar-Arevalo et al. (MiniBooNE Collaboration), Phys. Rev. D **88**, 032001 (2013).

[9] A. A. Aguilar-Arevalo et al. (MiniBooNE Collaboration), Phys. Rev. D **91**, 012004 (2015).

[10] K. Abe et al., (T2K Collaboration), Phys. Rev. D**87**, 092003 (2013).

[11] K. Abe et al., (T2K Collaboration), Phys. Rev. D**92**, 112003 (2015).

[12] J. Ryckebusch, M. Waroquier, K. Heyde, J. Moreau, and D. Ryckbosch, Nucl. Phys. A**476**, 237 (1988).

[13] J. Ryckebusch, K. Heyde, D. Van Neck, and M. Waroquier, Nucl. Phys. A**503**, 694 (1989).

[14] N. Jachowicz, S. Rombouts, K. Heyde, and J. Ryckebusch, Phys. Rev. C**59**, 3246 (1999).

[15] N. Jachowicz, K. Heyde, J. Ryckebusch, and S. Rombouts, Phys. Rev. C**65**, 025501 (2002).

[16] N. Jachowicz, K. Vantournhout, J. Ryckebusch, and K. Heyde, Phys. Rev. Lett. **93**, 082501 (2004).

[17] N. Jachowicz, G. C. McLaughlin, Phys. Rev. Lett. **96**, 172301 (2006).

[18] V. Pandey, N. Jachowicz, J. Ryckebusch, T. Van Cuyck, and W. Cosyn, Phys. Rev. C**89**, 024601 (2014).

[19] V. Pandey, N. Jachowicz, T. Van Cuyck, J. Ryckebusch, and M. Martini, PoS NUFACT2014, 055 (2015).

[20] V. Pandey, N. Jachowicz, T. Van Cuyck, J. Ryckebusch, and M. Martini, Phys. Rev. C**92** (2), 024606 (2015) .

[21] M. Waroquier, J. Ryckebusch, J. Moreau, K. Heyde, N. Blasi, S.Y. van de Werf, and G. Wenes, Phys. Rep. **148**, 249 (1987).

[22] J. Engel, Phys. Rev. C**57**, 2004 (1998).

[23] J. Ryckebusch, D. Debruyne, W. Van Nespen, and S. Janssen, Phys. Rev. C **60**, 034604 (1999).

[24] S. Jeschonnek, T. W. Donnelly, Phys. Rev. C**57**, 2438 (1998).

[25] M. Martini, M. Ericson, G. Chanfray, J. Marteau, Phys. Rev. C **80**, 065501 (2009).

[26] M. Martini, M. Ericson, G. Chanfray, J. Marteau, Phys. Rev. C **81**, 045502 (2010).

[27] J. E. Amaro et al., Phys. Lett. B696, 151-155 (2011).

[28] J. Nieves, I. Ruiz Simo, M. J. Vicente Vacas, Phys. Rev. C **83**, 045501 (2011).

[29] A. Bodek, H. Budd, M. E. Christy, Eur. Phys. J. C71, 1726 (2011).

[30] M. Martini, M. Ericson and G. Chanfray, Phys. Rev. C **84**, 055502 (2011).

[31] J. Nieves, I. Ruiz Simo and M. J. Vicente Vacas, Phys. Lett. B 707, 72 (2012).

[32] J. E. Amaro et al., Phys. Rev. Lett. 108, 152501 (2012).

[33] O. Lalakulich, K. Gallmeister and U. Mosel, Phys. Rev. C **86**, 014614 (2012).

[34] J. Nieves, I. Ruiz Simo and M. J. Vicente Vacas, Phys. Lett. B **721**, 90 (2013).

[35] M. Martini and M. Ericson, Phys. Rev. C **87**, 065501 (2013).

[36] G. D. Megias et al., Phys. Rev. D **91**, no. 7, 073004 (2015).

[37] T. Van Cuyck, N. Jachowicz, M. Martini, V. Pandey, J. Ryckebusch, in preparation.

[38] M. Martini, M. Ericson, Phys. Rev. C **90**, 025501 (2014).

[39] A. Meucci, C. Giusti, arXiv:1501.03213 [nucl-th].

[40] M. V. Ivanov, G. D. Megias, R. González-Jiménez, O. Moreno, M. B. Barbaro, J. A. Caballero, and T. W. Donnelly, arXiv:1506.00801 [nucl-th].

3.4 Electron-neutrino scattering off nuclei from two different theoretical perspectives [4]

M. Martini[1,2], N. Jachowicz[1], M. Ericson[3,4], V. Pandey[1], T. Van Cuyck[1], N. Van Dessel[1]

[1]Department of Physics and Astronomy, Ghent University,
Proeftuinstraat 86, B-9000 Gent, Belgium.

[2]ESNT, CEA-Saclay, IRFU, Service de Physique Nucléaire,
F-91191 Gif-sur-Yvette Cedex, France.

[3]Université de Lyon, Univ. Lyon 1, CNRS/IN2P3, IPN Lyon,
F-69622 Villeurbanne Cedex, France

[4]Physics Department, Theory Unit, CERN, CH-1211 Geneva, Switzerland

Abstract

We analyze charged-current electron-neutrino cross sections on Carbon. We consider two different theoretical approaches, on one hand the Continuum Random Phase Approximation (CRPA) which allows a description of giant resonances and quasielastic excitations, on the other hand the RPA-based calculations which are able to describe multinucleon emission and coherent and incoherent pion production as well as quasielastic excitations. We compare the two approaches in the genuine quasielastic channel, and find a satisfactory agreement between them at large energies while at low energies the collective giant resonances show up only in the CRPA approach. We also compare electron-neutrino cross sections with the corresponding muon-neutrino ones in order to investigate the impact of the different charged-lepton masses. Finally, restricting to the RPA-based approach we compare the sum of quasielastic, multinucleon emission, coherent and incoherent one-pion production cross sections (folded with the electron-neutrino T2K flux) with the charged-current inclusive electron-neutrino differential cross sections on Carbon measured by T2K. We find a good agreement with the data. The multinucleon component is needed in order to reproduce the T2K electron-neutrino inclusive cross sections.

I. Introduction

Recent years have seen an accumulation of data on muon-neutrino cross sections on nuclei at intermediate energies [1–19]. These measurements have revealed interesting features in different reaction channels. For example, the charged-current quasielastic (CCQE) measurement performed by MiniBooNE [1] has attracted a lot of attention due to its unexpected behavior, reproducible with an unphysical value of the axial mass. This axial mass anomaly is now explained by the inclusion of events in which several nucleons are ejected in the CCQE cross section [20–33]. In the one-pion production channel some questions are still open. For instance, various theoretical

---

[4]This manuscript is submitted for publication in Phys. Rev. C (arXiv:1602.00230 [nucl-th]). I performed part of the CRPA calculations and made figures 3.44, 3.45 and 3.46.

models [34, 35] cannot simultaneously reproduce the MiniBooNE [2, 5] and the MINERvA [15] results.

The wealth of experimental and theoretical results on muon-neutrino cross sections contrasts with the few published results on electron-neutrino cross sections. After the inclusive ν_e CC total cross sections measured by the Gargamelle bubble chamber in 1978 [36], the first measurement of inclusive ν_e CC differential cross sections on Carbon was performed by T2K [37]. Recently the measurement performed by MINERvA of quasielastic and quasielastic-like differential cross sections on Carbon also appeared [38]. A precise knowledge of ν_μ and ν_e cross sections is important in connection to the $\nu_\mu \to \nu_e$ oscillation experiments which aim at the determination of the neutrino mass hierarchy and the search for CP violation in the lepton sector. A theoretical comparison of the ν_μ and ν_e cross sections was performed by Day and McFarland [39] who analyzed the influence of the final lepton-mass difference on the cross sections as a function of the neutrino energy and of Q^2. Here we study these differences focusing on the ν_μ and ν_e differential cross sections. In a first part we consider the electron-neutrino cross sections on Carbon using two different theoretical models. The first one is the one of Martini *et al.* [20] which is based on nuclear response functions, treated in the random phase approximation (RPA) on top of a local relativistic Fermi gas (LRFG) calculation. It includes the quasielastic cross section, multinucleon emission and coherent and incoherent single pion production. The second model is the one of Jachowicz *et al.* [40] which is based on the continuum random phase approximation (CRPA) on top of Hartree-Fock (HF) calculations. It was originally developed to study electroweak reactions in the giant resonance region and then extended by Pandey *et al.* [41, 42] to the quasielastic regime. The common channel where the two approaches can be compared is hence the quasielastic one. After a brief description of the two theoretical models, we confront their results in the quasielastic channel, first for fixed kinematics, then folding them with the T2K and the MiniBooNE ν_e fluxes. We also illustrate in both models the differences between ν_μ and ν_e cross sections. Finally, we compare the predictions in the approach of Martini *et al.*, with the inclusive ν_e CC differential cross sections on Carbon recently measured by T2K [37]. We postpone the comparison with the very recent MINERvA results [38] to a future paper.

II. Theoretical models

We summarize here the basic ingredients of the two models. Both approaches calculate the polarization propagator Π in the random phase approximation (RPA) which allows the inclusion of long-range nucleon-nucleon correlations. This amounts to solving integral equations which have the generic form

$$\Pi = \Pi^0 + \Pi^0 V \Pi, \tag{3.42}$$

where Π^0 is the bare polarization propagator and V denotes the effective particle-hole interaction. However, the bare polarization propagator and the residual interaction differ in the two approaches. For Martini *et al.* [20] the bare polarization propagator is evaluated in momentum space. In a finite system it is non-diagonal and writes $\Pi^0(\omega, \mathbf{q}, \mathbf{q}')$. In order to account for the finite-size effects, it is evaluated in a semi-classical approximation [43, 44] where it can be cast

in the form

$$\Pi^0(\omega, \mathbf{q}, \mathbf{q}') = \int d\mathbf{r} \, e^{-i(\mathbf{q}-\mathbf{q}')\cdot\mathbf{r}} \, \Pi^0\left(\omega, \frac{\mathbf{q}+\mathbf{q}'}{2}, \mathbf{r}\right). \tag{3.43}$$

To obtain this quantity, a local density approximation is used which relates the final result to the relativistic Fermi gas polarization propagator according to

$$\Pi^0\left(\omega, \frac{\mathbf{q}+\mathbf{q}'}{2}, \mathbf{r}\right) = \Pi^0_{k_F(r)}\left(\omega, \frac{\mathbf{q}+\mathbf{q}'}{2}\right). \tag{3.44}$$

The local Fermi momentum $k_F(r)$ is related to the experimental nuclear density through : $k_F(r) = (3/2\,\pi^2\,\rho(r))^{1/3}$. The density profiles of ^{12}C are taken from the Sum-of-Gaussians nuclear charge density distribution parameters according to Ref. [45]. In the approach of Jachowicz *et al.* [40], the starting point is the continuum Hartree-Fock model which evaluates the bound and the continuum single-nucleon wave functions through the solution of the Schrödinger equation with a mean field potential. The bare polarization propagator, in this case the HF one, is then calculated in coordinate space.

The particle-hole residual interaction differs as well in the two approaches. In the Martini *et al.* one, a parameterization in terms of pion exchange, rho exchange and contact Landau-Migdal parameters is used while in the Jachowicz *et al.* model, the same Skyrme-type interaction which enters in the mean field calculation is employed to generate the continuum RPA (CRPA) solution. In this way, this calculation becomes self-consistent with respect to the interaction used. In Ref. [42] this residual Skyrme-type interaction is multiplied by a dipole form factor which controls the influence of the residual interaction at high Q^2 values.

Concerning the RPA differences, an important point should be mentioned. The possibility of Δ excitation is included explicitly in the case of Martini *et al.* This is reflected in the appearance, in certain kinematical regions, of a sizeable quenching of the RPA results, due to the mixing of nucleon-hole states with Δ-hole ones, the Ericson-Ericson–Lorentz-Lorenz (EELL) effect [47]. This quenching has been introduced and established in pion scattering [47]. It has been discussed also in relation with electron [46] and neutrino [20, 25, 48] scattering.

III. Comparison between theoretical calculations

A. LRFG+RPA *vs* HF+CRPA

In this Subsection, we compare the theoretical results in the one nucleon-one hole sector obtained in the two different approaches. We consider the ν_e-^{12}C double differential cross sections for different values of the neutrino energy and of the lepton scattering angle. These cross sections are purely theoretical quantities since the experimental ones depend on the neutrino fluxes and hence are specific for each experiment. In Fig.3.38 we display the results of the two approaches by switching on and off the residual particle-hole interaction. We keep the same notations as in the previous papers of the groups. Namely we call "bare-LRFG" the results of Martini *et al.* when the particle-hole interaction is switched off (these are Relativistic Fermi Gas results in the local density approximation) and "RPA" the results obtained by switching on the particle-hole interaction. The corresponding results in the case of Jachowicz *et al.* are called "HF" and
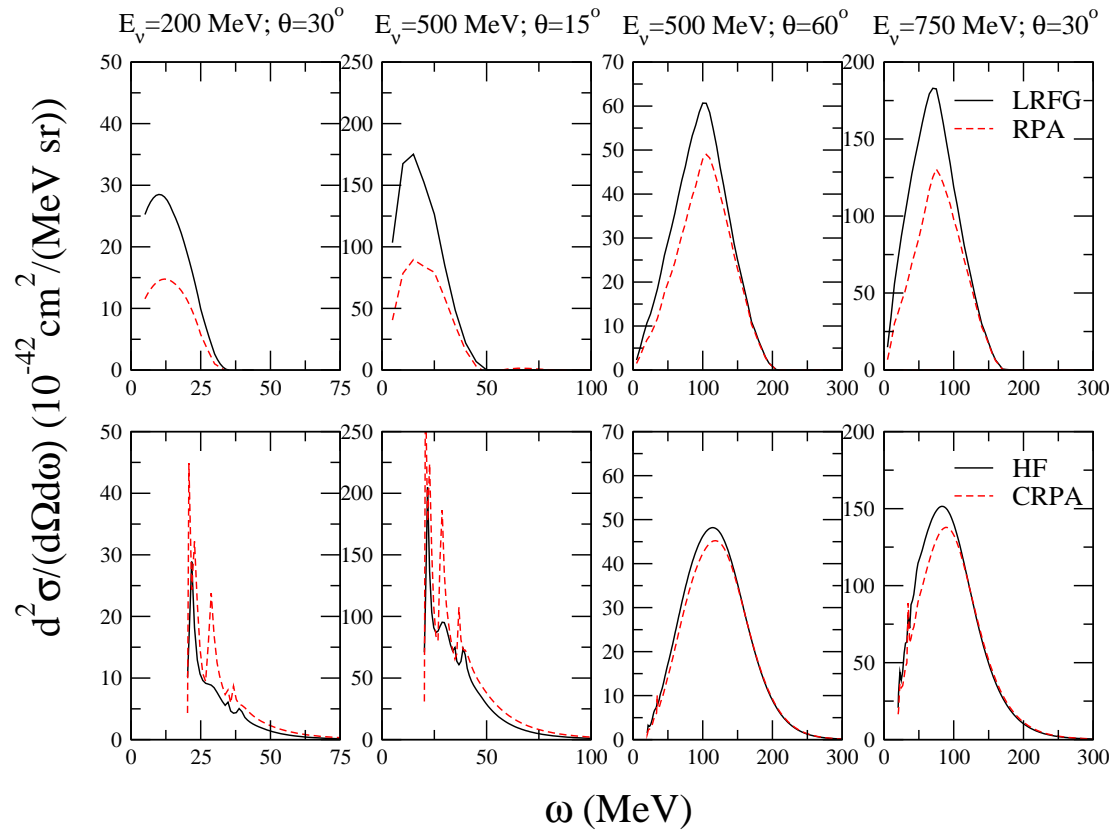
FIGURE 3.38: (Color online) Electron-neutrino CC double differential cross section on Carbon for fixed values of scattering angles and incident neutrino energies as a function of the energy transferred to the nucleus. In the upper (lower) panels the results obtained in the bare-LRFG (HF) and RPA (CRPA) approaches are displayed. Only genuine quasielastic and giant resonance excitations (given by the CRPA) are considered.

"CRPA". Some important differences between the two approaches appear. The most striking feature is the appearance of giant resonance peaks in the CRPA of Jachowicz *et al.* They vanish for large neutrino energy or larger scattering angle. The second comment concerns the threshold energy in the HF+CRPA approach, about $\simeq 18$ MeV, which reflects the nucleon separation energy, ignored in the semi-classical approximation of Martini *et al.* The HF+CRPA results also display the shell structure, which is not present in the semiclassical description. It disappears at large angles or energies, where the two approaches become more similar. Howewer the quasielastic peak is somewhat quenched in the mean field HF case when compared to the semiclassical LRFG results and the high transferred-energy tail is more important in the HF case. This is a consequence of the non-locality of the mean field which quenches and hardens the responses.

In this Subsection, we compare the theoretical results in the one nucleon-one hole sector obtained in the two different approaches. We consider the ν_e-^{12}C double differential cross sections for different values of the neutrino energy and lepton scattering angle. These cross sections are purely theoretical quantities since the experimental ones depend on the neutrino fluxes and hence are specific for each experiment. In Fig.3.38 we display the results of the two approaches by switching on and off the residual particle-hole interaction. We keep the same notations as
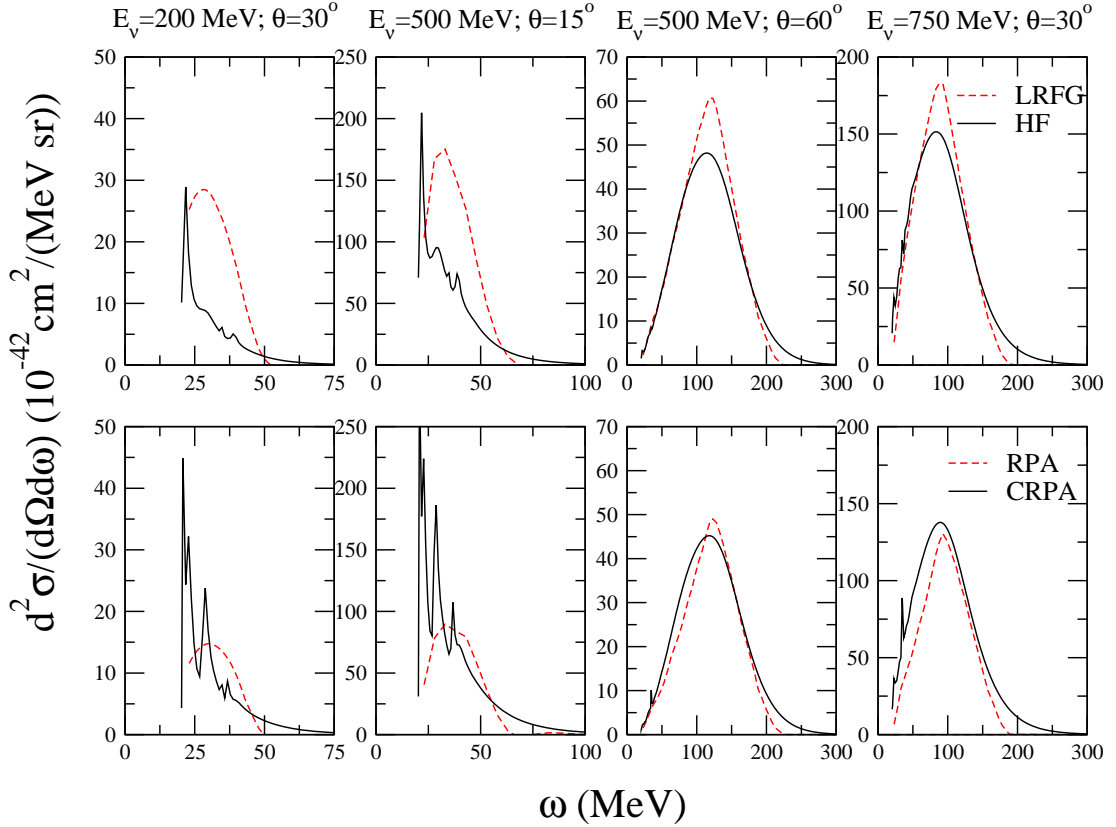
FIGURE 3.39: (Color online) Electron-neutrino CC double differential cross section on Carbon for fixed values of scattering angles and incident neutrino energies as a function of the energy transferred to the nucleus. In the upper (lower) panels the results obtained in the bare-LRFG (RPA) and HF (CRPA) approaches are displayed. Only genuine quasielastic and giant resonances excitations (given by the CRPA) are considered. Continuous lines: HF and CRPA results; dashed lines: LRFG and RPA results shifted by 18 MeV.

in the previous papers of the groups. Namely we call "bare-LRFG" the results of Martini *et al.* when the particle-hole interaction is switched off (these are relativistic Fermi gas results in the local density approximation) and "RPA" the results obtained by switching on the particle-hole interaction. The corresponding results in the case of Jachowicz *et al.* are called "HF" and "CRPA". Some important differences between the two approaches appear. The most striking feature is the appearance of giant resonance peaks in the CRPA results of Jachowicz *et al.* They vanish for large neutrino energy or larger scattering angle. The second comment concerns the threshold energy in the HF+CRPA approach, about $\simeq 18$ MeV, which reflects the nucleon separation energy, ignored in the semi-classical approximation of Martini *et al.* The HF+CRPA results also display the shell structure, which is not present in the semiclassical description. It disappears at large angles or energies, where the two approaches become more similar. However, when compared to the semiclassical LRFG results, in the mean field HF case the quasielastic peak is somewhat quenched and the high transferred-energy tail is more important. This is a consequence of the non-locality of the mean field which quenches and hardens the responses.

Turning to RPA effects, the important difference is the large RPA quenching in the Martini *et al.* approach, due to the mixing with Δ-hole states that we have commented before, not explicitly present in the CRPA results of Jachowicz *et al.*
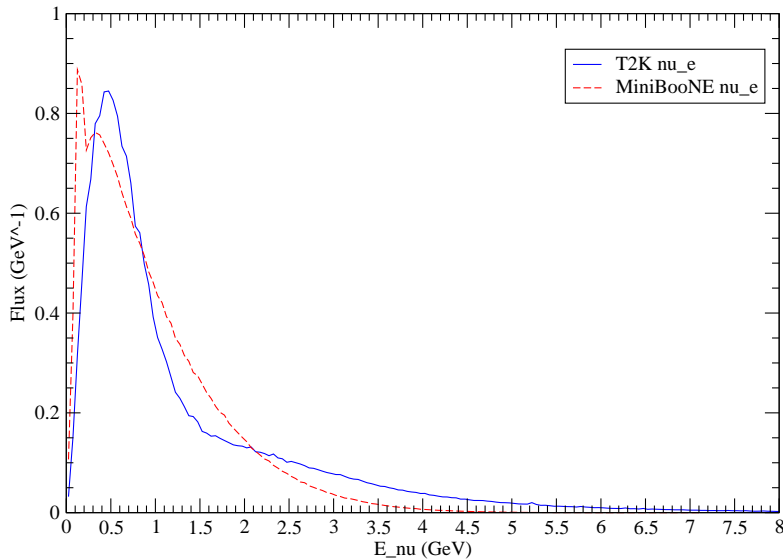
FIGURE 3.40: (Color online) Normalized electron-neutrino T2K [49] and MiniBooNE [50] fluxes.

In order to better illustrate the comparison between the two approaches, we show in Fig. 3.39 the LRFG and RPA results shifted by 18 MeV, an average value of the separation energy, and we compare them with the HF and CRPA results respectively. For the structureless part of the cross sections, *i.e.* for the kinematical conditions dominated by the quasielastic excitations (*e.g.* $\theta = 60^o$ and $E_{\nu_e} = 500$ MeV or $\theta = 30^o$ and $E_{\nu_e} = 750$ MeV), the two approaches are essentially in agreement. Furthermore the HF and CRPA cross sections are characterized by stronger tails at high transferred energies. In the low-energy part, the RPA results (which do not show giant resonance peaks) represent the average of the CRPA calculations relatively well.

Turning to the flux folded cross sections we consider the T2K [49] and MiniBooNE [50] ν_e normalized fluxes, which are shown in Fig. 3.40. We discuss single-differential cross sections, $\frac{d\sigma}{dp_e}$ and $\frac{d\sigma}{d\cos\theta_e}$, their theoretical evaluation is displayed in Fig. 3.41. One observes that the giant resonance effects are no longer apparent and that in general the differences between HF and CRPA calculations are largely washed out by the flux folding, except maybe for very forward scattering. Moreover in the case of MiniBooNE fluxes the HF or CRPA results are very similar to the LRFG ones while the RPA curves, which are somewhat below, display the usual EELL quenching. In the T2K case instead some small differences appear: the HF and CRPA results are above the corresponding LRFG cross section. This difference, which did not show with the MiniBooNE flux, is the effect of the larger T2K high energy tail. The differences between the two different theoretical models are weighted in different ways by the different flux profiles. But apart from the RPA quenching the differences are small.

B. ν_e *vs* ν_μ cross sections

After the discussion of the differences between the two approaches for the ν_e case, we turn to a comparison between the charged current ν_e and ν_μ cross sections. In order to show some theoretical results in touch with the experimental situation, we present in Fig. 3.42 the double
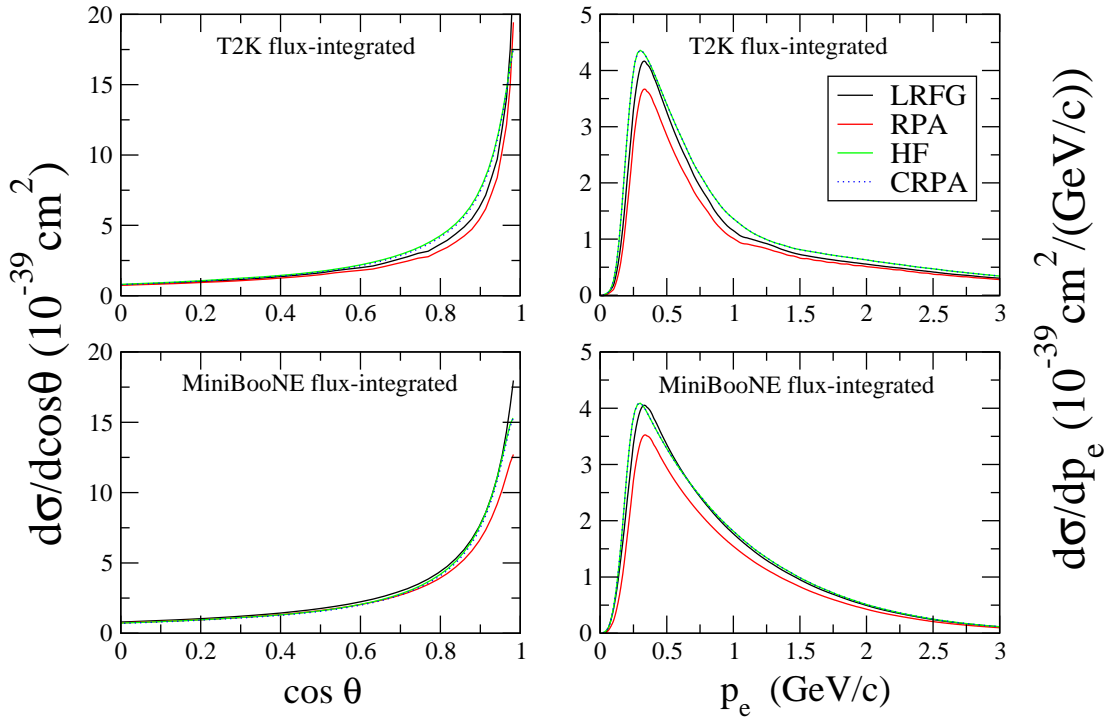
FIGURE 3.41: (Color online) Electron-neutrino T2K and MiniBooNE flux-folded CC single differential cross sections on Carbon per nucleon.
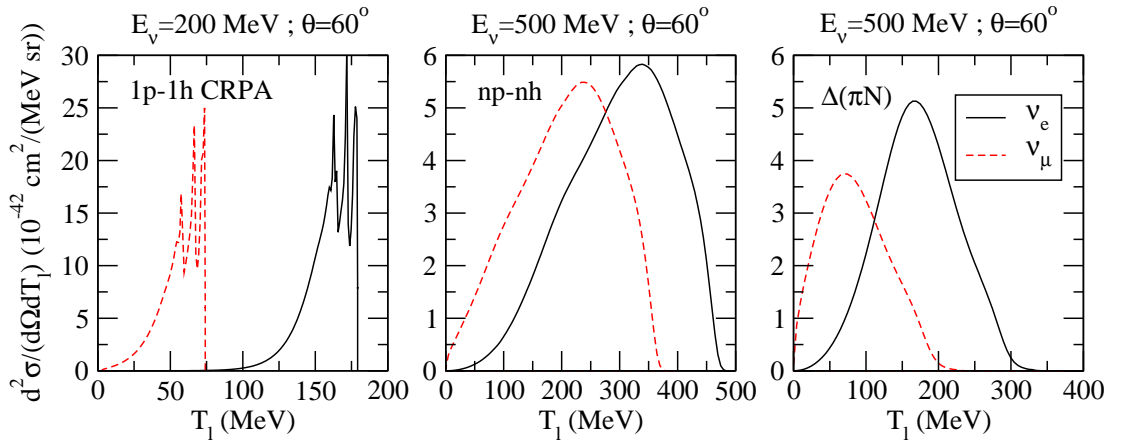

FIGURE 3.42: (Color online) Electron- and muon-neutrino CC double differential cross section on Carbon for fixed values of scattering angles and incident neutrino energies as a function of the charged lepton kinetic energy. Left panel: 1p-1h excitations in CRPA; middle panel: np-nh excitations; right panel: incoherent one pion production contribution.
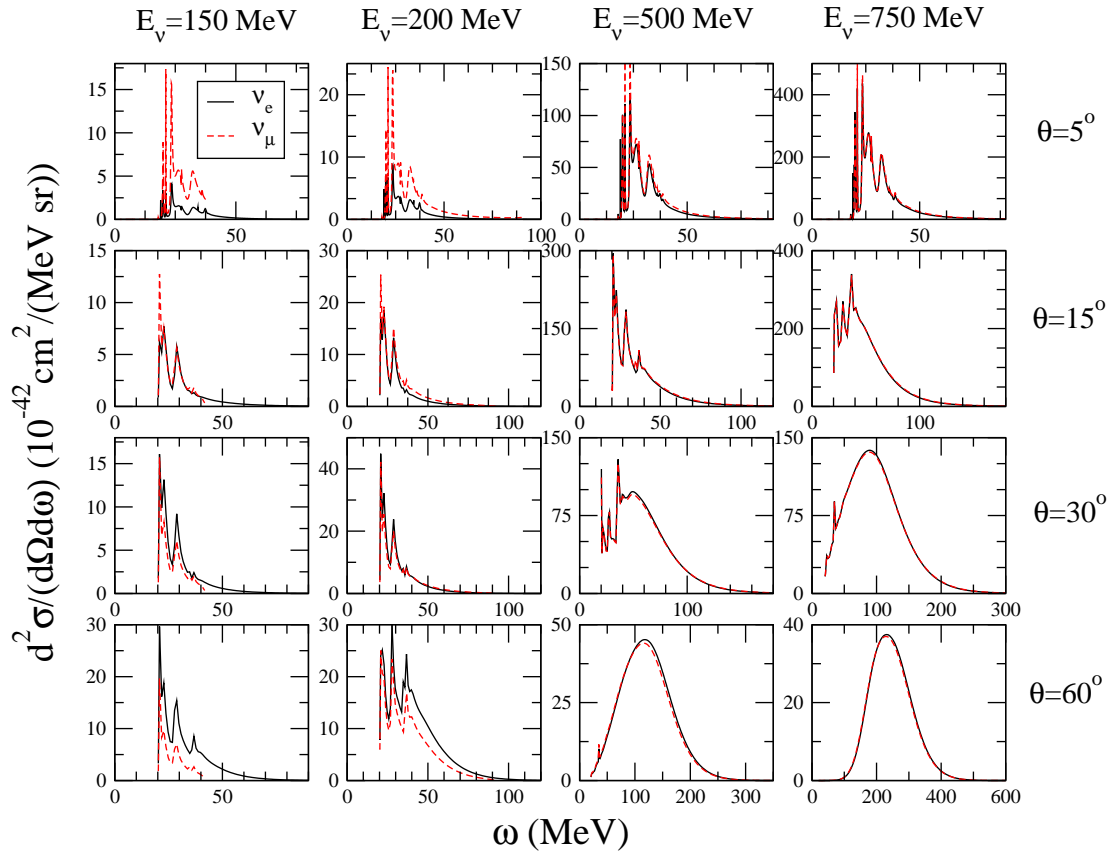
FIGURE 3.43: (Color online) Electron- and muon-neutrino CC double differential cross section on Carbon calculated in the CRPA approach for fixed values of scattering angles and incident neutrino energies as a function of the energy transferred to the nucleus.
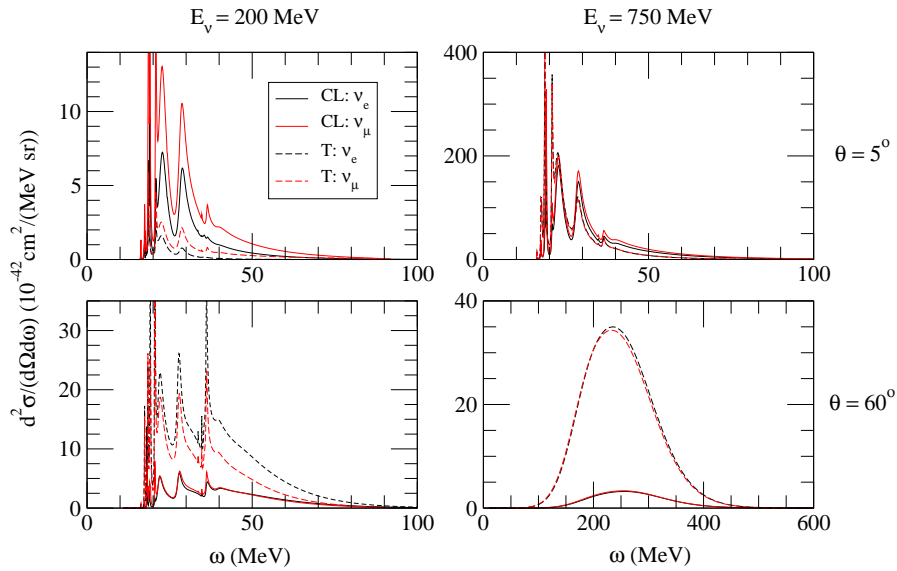

FIGURE 3.44: (Color online) Coulomb-longitudinal (CL) and transverse (T) contributions to electron- and muon-neutrino CC double differential cross section on Carbon calculated in the CRPA approach for incident neutrino energies of 200 MeV and 750 MeV and two fixed values of scattering angles as a function of the transferred energy to the nucleus.
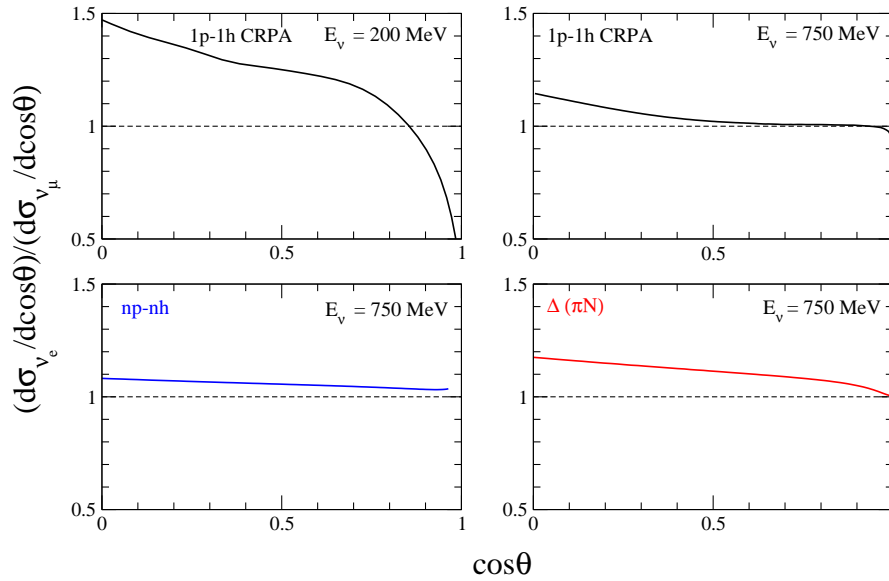
FIGURE 3.45: (Color online) Ratio of the ν_e over ν_μ differential cross section on Carbon calculated in the CRPA approach for two fixed values of incident neutrino energies as a function of the cosine of the lepton scattering angle. The 1p-1h results in the CRPA approach are shown for E_ν=200 MeV and E_ν=750 MeV. The np-nh excitations and the pion production (via Δ excitation) results are shown for E_ν=750 MeV.

differential cross sections in the different channels for fixed values of the scattering angle and neutrino energy (hence not flux-folded) as a function of the lepton kinetic energy T_l, a measured quantity. The role of the different charged lepton masses appears not only in the trivial relative shift between the ν_e and ν_μ CC cross sections, according to the identities

$$T_l = E_l - m_{\text{lepton}} = E_\nu - \omega - m_{\text{lepton}} = \omega_{max} - \omega, \qquad (3.45)$$

but also in the strength and in the shape of the cross sections. In order to better illustrate these differences, we plot in the following figures (Figs. 3.43, 3.44 and 3.46) the differential cross sections not as a function of the lepton kinetic energy but as a function of the energy transfer $\omega = E_\nu - m_{\text{lepton}} - T_l$.

We start with the CRPA case which allows a simultaneous treatment of giant resonances and quasielastic excitations. In Fig. 3.43, we display the double-differential cross sections for different values of incoming neutrino energy and lepton scattering angle, both for ν_e and ν_μ. In most cases the ν_e and ν_μ results are quite similar, sometimes practically indistinguishable. However, in some cases interesting differences appear. The first one is a consequence of the stringent limit on the maximum transferred energy $\omega_{max} = E_\nu - m_{\text{lepton}}$ which has smaller values in the muon case. This threshold effect can be observed in Fig. 3.43 for E_ν=150 MeV and for E_ν=200 MeV in the case of 60 degrees. Other differences can be appreciated by observing the evolution with the scattering angle of the cross sections at small neutrino energies such as E_ν=150 MeV or E_ν=200 MeV. For small scattering angles such as 5 degrees, ν_μ cross sections are higher than the ν_e ones, while for larger scattering angles, for example 60 degrees this behaviour is opposite. At intermediate angles the two cross sections are closer to each other. This angular behavior

weakly survives at E_ν=500 MeV while for E_ν=750 MeV the ν_e and ν_μ cross sections practically coincide for all the scattering angles.

It is also interesting to illustrate the behavior of ν_e and ν_μ cross sections by separating their contribution, as shown in Fig.3.44 for incoming neutrino energies of E_ν=200 MeV and E_ν=750 MeV. According to the notation of Ref. [41], the global contribution related to the Coulomb and longitudinal multipole excitation operators (containing vector and axial components) is labeled as CL. In the language of Refs. [20, 21] it represents the sum of isovector and isospin spin-longitudinal response contributions. The sum of transverse contributions, including the vector-axial interference term, is labeled as T. These are the terms containing the isospin spin-transverse reponse in the language of Refs. [20, 21]. As one can observe in Fig.3.44, for E_ν=200 MeV and θ=5 degrees (and in general for very forward scattering) the neutrino cross section is dominated by the CL contribution while for larger angles, such as 60 degrees, the transverse contribution T is dominant. At larger energies the transverse part dominates everywhere except for very small scattering angles. At E_ν=200 MeV and $\theta = 5$ degrees the dominant CL contribution to the cross sections, as well as the smaller T one, are larger for ν_μ than for ν_e, hence the larger ν_μ cross sections for this case. The relative weight of CL and T contributions is the result of a subtle interplay between lepton kinematic factors and response functions. The competition for dominance of the cross section between both, is very sensitive to energy and momentum transfer. The surprising dominance of ν_μ over ν_e cross sections for small scattering angles is related to this and dictated by the non-trivial dependence of momentum transfer on lepton mass and scattering angle for forward scattering.

The non-trivial behaviour of the ν_e cross sections with respect to the ν_μ ones is also illustrated in Fig. 3.45 where the ratio of the single differential cross section $\frac{d\sigma_{\nu_e}}{d\cos\theta}/\frac{d\sigma_{\nu_\mu}}{d\cos\theta}$ is shown. For the 1p-1h channel in the CRPA approach, this ratio varies from ~ 1.5 to 0.3 by increasing $\cos\theta$ from 0 to 1 for a fixed neutrino of E_ν=200 MeV. At larger neutrino energies, such as E_ν=750 MeV, this ratio remains closer to 1 for the 1p-1h sector in CRPA. In Fig. 3.45 this quantity $\frac{d\sigma_{\nu_e}}{d\cos\theta}/\frac{d\sigma_{\nu_\mu}}{d\cos\theta}$ at E_ν=750 MeV is given also for two other channels, the pion production and multinucleon excitations. For these channels we restrict the ν_e/ν_μ comparison to the Martini *et al.* approach since they are not available in the Jachowicz *et al.* one. This $\frac{d\sigma_{\nu_e}}{d\cos\theta}/\frac{d\sigma_{\nu_\mu}}{d\cos\theta}$ ratio, always larger than 1, is characterized by a smooth decreasing behavior. For the pion emission channel (via Δ excitation) this ratio is larger than the one for the np-nh and 1p-1h excitations. For all the 3 channels the deviation from unity of the ratio is small at E_ν=750 MeV if compared to the E_ν=200 MeV 1p-1h CRPA result.

Concerning the pion production and multinucleon excitations, we display for completeness in Fig. 3.46 the ν_e and ν_μ results obtained for these channels (as well as for the QE one) in the approach of Martini *et al.* for the double differential cross sections at incoming neutrino energies of $E_\nu = 500$ MeV and $E_\nu = 750$ MeV and scattering angles of 30 and 60 degrees. One observes the clear energy separation between the three channels, the highest energy transfer occurring for pion emission. Ignoring Fermi momentum and RPA reshaping effects, the quasi elastic peak occurs for an energy transfer $\omega = Q^2/(2M_N)$ where $Q^2 = q^2 - \omega^2 = 2E_\nu E_l(1 - \cos\theta) - m_l^2 + 2E_\nu(E_l - P_l)\cos\theta$. In the electron case where $m_l = 0$ it leads to $\omega = E_\nu^2(1 - \cos\theta)/(M_N + E_\nu(1 - \cos\theta))$. As for pion emission, in our model it occurs via Δ excitation. In the same
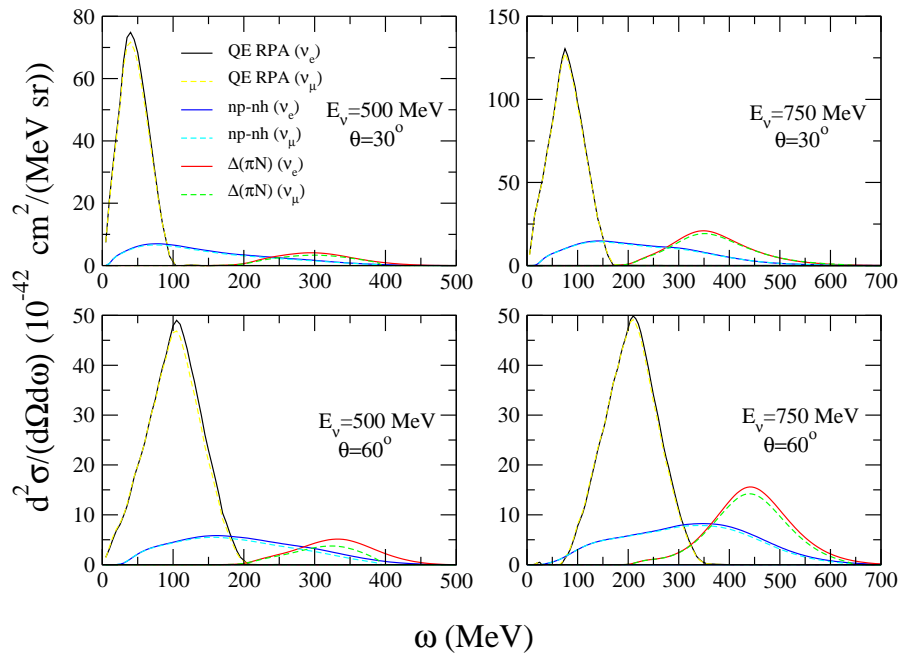
FIGURE 3.46: (Color online) Electron- and muon-neutrino CC double differential cross section on Carbon calculated in the RPA approach for fixed values of scattering angles and incident neutrino energies as a function of the transferred energy to the nucleus. The genuine quasielastic (QE), multinucleon (np-nh), and incoherent one-pion production excitations are plotted separately.

(nucleons at rest) approximation the pion emission peak is shifted towards large energy transfer, with the condition $\omega = Q^2/(2M_N) + \Delta M$ with $\Delta M = (M_\Delta^2 - M_N^2)/2M_N = 338$ MeV. This leads for ν_e to $\omega = (M_N \Delta M + E_\nu^2(1 - \cos\theta))/(M_N + E_\nu(1 - \cos\theta))$. These formulas explain the positions of the quasielastic and Δ peaks. As for the multinucleon excitations they lie between the two. The difference between the ν_e and ν_μ cross sections mostly shows up in the energy transfer limit which is $\omega_{max} \simeq E_\nu$ for electrons and $\omega_{max} = E_\nu - m_\mu$ for muons. Hence it shows up mostly for pion production and it is more pronouced at low neutrino energies. It is also more pronounced at large scattering angles since the double differential cross sections move towards larger ω when the scattering angle increases. This behavior with the scattering angle appears also in the previous Fig. 3.45.

IV. Comparison with the T2K ν_e inclusive cross sections

The T2K collaboration published the first results for ν_e charged-current inclusive differential cross sections on Carbon [37]. In this section we compare these experimental results with our predictions, restricting to the Martini *et al.* [20] RPA approach. We compute the ν_e T2K flux averaged differential cross sections $\frac{d\sigma}{dp_e}$ and $\frac{d\sigma}{d\cos\theta_e}$ in the different excitation channels, namely quasielastic, multinucleon excitations (np-nh) and one-pion (coherent and incoherent) production. In Figs. 3.47 and 3.48 we plot the different exclusive channel contributions separately, as well as their sum. This sum is in a good agreement with the experiment. Notice that this agreement needs the presence of the np-nh contribution (which even dominates the genuine QE one for small p_e values, $p_e \lesssim 0.2$ GeV), a conclusion already reached by Martini and Ericson [31]
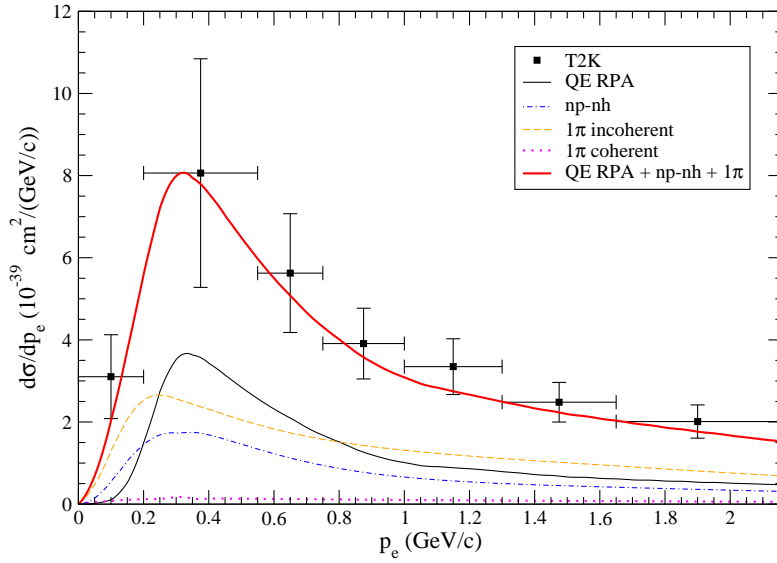
FIGURE 3.47: (color online). T2K flux-integrated inclusive ν_e CC differential cross section on Carbon per nucleon as a function of the electron momentum. The different contributions to this inclusive cross section obtained in the model of Ref. [20] are shown. The experimental T2K points are taken from Ref. [37].

FIGURE 3.48: (color online). T2K flux-integrated inclusive ν_e CC differential cross section on Carbon per nucleon as a function of the cosine of the lepton scattering angle. The different contributions to this inclusive cross section obtained in the model of Ref. [20] are shown. The experimental T2K points are taken from Ref. [37].
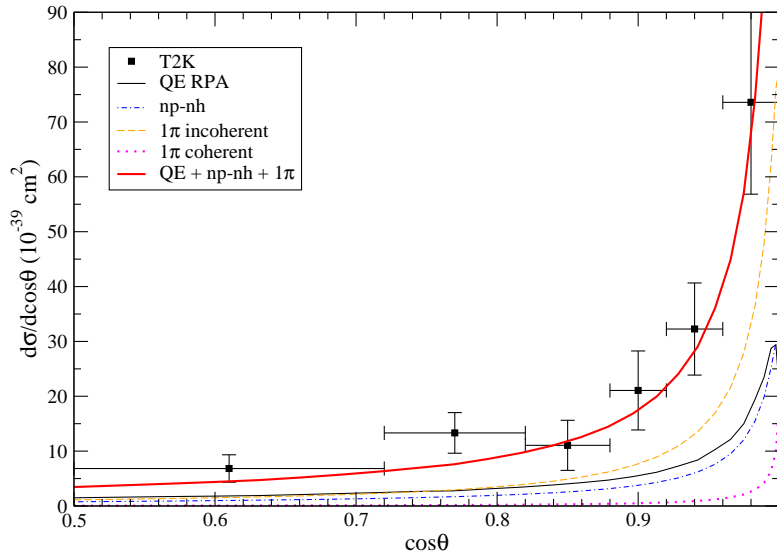
in connection with the T2K inclusive ν_μ double differential cross sections [9]. This agreement with both ν_μ and ν_e CC inclusive T2K flux folded differential cross sections is not systematically obtained in other approaches. For instance the SuSAv2 model by Ivanov *et al.* [51] reproduces well the CC inclusive T2K flux folded ν_μ double differential cross section but underestimates the CC inclusive T2K flux folded ν_e single differential cross section. A comparison with these quantities has also been performed by Meucci and Giusti using the Relativistic Green's function model which turned to underestimate the ν_μ and ν_e CC inclusive T2K data [52].

V. Summary and Conclusions

In conclusion, our study has dealt with several facets of the neutrino interaction with nuclei. A large part is devoted to the comparison between two different approaches to describe the interaction of neutrinos with nuclei. Both go beyond the impulse approximation and take into account, albeit in different ways, the interaction between nucleons. The CRPA approach of Jachowicz *et al.* starts from a continuum Hartree Fock description with Skyrme type interactions. The shell structure of the nucleus is present in this approach. The RPA-based approach of Martini *et al.* instead starts from a semiclassical description of the bare polarization propagator with a realistic nuclear density distribution. The shell structure is ignored in this description. The RPA effects also differ in the two approaches. For the residual interaction the first method uses the same Skyrme interaction as for the mean field, while in the approach of Martini *et al.*, it is parametrized in terms of pion and rho exchange and a contact Landau Migdal interaction. But the main difference is the possibility of mixing of Δ-hole states in the second approach. It produces a general quenching of the responses which shows up in most kinematical conditions that we have explored. The CRPA of Jachowicz *et al.* allows a description of giant resonances and quasielastic excitations while the RPA evaluations of Martini *et al.* includes quasielastic but also coherent and incoherent pion production, and multinucleon excitations.

We have compared the two approaches for the one nucleon - one hole excitations finding a reasonable agreement between them in the quasielastic peak region, with a trend for the RPA approach to lead to lower cross sections than the CRPA presumably due to the mixing with Δ excitations. Other general trends are related to the more important high transferred-energy tail in the CRPA results and to a relative shift of the cross sections of $\omega \simeq 18$ MeV, reflecting the presence of the nucleon separation energy in the CRPA calculations. The most striking difference is the appearence of giant resonance peaks in the CRPA results. The comparison of the two approaches has been performed for fixed values of the incoming neutrino energy as well as for the ν_e T2K and MiniBooNE flux-folded cross sections.

We have also compared the ν_e cross sections with the corresponding ν_μ ones for fixed values of the neutrino energy in order to investigate the impact of different charged lepton masses. We have found some non trivial behaviour, in particular for the 1p-1h excitations at low neutrino energies, such as an inversion with the scattering angle of the relative strength of ν_e and ν_μ cross sections. Due to the different kinematical limits, the ν_e cross sections are in general expected to be larger than the ν_μ ones, however for forward scattering angles this hierarchy is opposite. In the precision era of neutrino oscillation physics the ν_e cross sections should be known with the

same accurancy as the ν_μ ones. Trying to deduce the ν_e cross sections from the experimental ν_μ ones can be considered only as a first approximation in the study of the ν_e interactions.

Concerning the comparison with experiment, we have considered the inclusive ν_e T2K flux-folded single-differential cross sections on Carbon and we have compared the data with the RPA-based approach. We have found a good agreement by adding the genuine quasielastic, the multinucleon and the one-pion production channels. This success obtained with a new flux, such as the ν_e T2K one, complements those already reached with the three different fluxes, such as the MiniBooNE ν_μ and $\bar{\nu}_\mu$, and T2K ν_μ ones.

Acknowledgments

Bibliography

[1] A. A. Aguilar-Arevalo *et al.* [MiniBooNE Collaboration], Phys. Rev. **D81**, 092005 (2010).

[2] A. A. Aguilar-Arevalo *et al.* [MiniBooNE Collaboration], Phys. Rev. D **81**, 013005 (2010).

[3] A. A. Aguilar-Arevalo *et al.* [MiniBooNE Collaboration], Phys. Rev. **D82**, 092005 (2010).

[4] Y. Nakajima *et al.* [SciBooNE Collaboration], Phys. Rev. D **83**, 012005 (2011).

[5] A. A. Aguilar-Arevalo *et al.* [MiniBooNE Collaboration], Phys. Rev. D **83**, 052007 (2011).

[6] A. A. Aguilar-Arevalo *et al.* [MiniBooNE Collaboration], Phys. Rev. D **83**, 052009 (2011).

[7] C. Anderson *et al.* [ArgoNeuT Collaboration], Phys. Rev. Lett. **108**, 161802 (2012).

[8] A. A. Aguilar-Arevalo *et al.* [MiniBooNE Collaboration], Phys. Rev. D **88**, 032001 (2013).

[9] K. Abe *et al.* [T2K Collaboration], Phys. Rev. D **87**, 092003 (2013).

[10] G. A. Fiorentini *et al.* [MINERvA Collaboration], Phys. Rev. Lett. **111**, 022502 (2013).

[11] L. Fields *et al.* [MINERvA Collaboration], Phys. Rev. Lett. **111**, no. 2, 022501 (2013).

[12] R. Acciarri *et al.* [ArgoNeuT Collaboration], Phys. Rev. D **89**, no. 11, 112003 (2014).

[13] K. Abe *et al.* [T2K Collaboration], Phys. Rev. D **90**, no. 5, 052010 (2014).

[14] A. Higuera *et al.* [MINERvA Collaboration], Phys. Rev. Lett. **113**, no. 26, 261802 (2014).

[15] B. Eberly *et al.* [MINERvA Collaboration], arXiv:1406.6415 [hep-ex].

[16] R. Acciarri *et al.* [ArgoNeuT Collaboration], Phys. Rev. Lett. **113**, no. 26, 261801 (2014) [Erratum-ibid. **114**, no. 3, 039901 (2015)].

[17] T. Walton *et al.* [MINERvA Collaboration], Phys. Rev. D **91**, no. 7, 071301 (2015).

[18] T. Le *et al.* [for the MINERvA Collaboration], Phys. Lett. B **749**, 130 (2015)[arXiv:1503.02107 [hep-ex]].

[19] K. Abe *et al.* [T2K Collaboration], Phys. Rev. D **91**, no. 11, 112002 (2015)

[20] M. Martini, M. Ericson, G. Chanfray, J. Marteau, Phys. Rev. **C80**, 065501 (2009).

[21] M. Martini, M. Ericson, G. Chanfray, J. Marteau, Phys. Rev. **C81**, 045502 (2010).

[22] J. E. Amaro *et al.*, Phys. Lett. **B696**, 151-155 (2011).

[23] J. Nieves, I. Ruiz Simo, M. J. Vicente Vacas, Phys. Rev. **C83**, 045501 (2011).

[24] A. Bodek, H. Budd, M. E. Christy, Eur. Phys. J. **C71**, 1726 (2011).

[25] M. Martini, M. Ericson and G. Chanfray, Phys. Rev. C **84**, 055502 (2011).

[26] J. Nieves, I. Ruiz Simo and M. J. Vicente Vacas, Phys. Lett. B **707**, 72 (2012).

[27] J. E. Amaro *et al.*, Phys. Rev. Lett. **108**, 152501 (2012).

[28] O. Lalakulich, K. Gallmeister and U. Mosel, Phys. Rev. C **86**, 014614 (2012).

[29] J. Nieves, I. Ruiz Simo and M. J. Vicente Vacas, Phys. Lett. B **721**, 90 (2013).

[30] M. Martini and M. Ericson, Phys. Rev. C **87**, 065501 (2013).

[31] M. Martini and M. Ericson, Phys. Rev. C **90**, 025501 (2014).

[32] G. D. Megias *et al.*, Phys. Rev. D **91**, no. 7, 073004 (2015)

[33] M. Ericson and M. Martini, Phys. Rev. C **91**, no. 3, 035501 (2015).

[34] J. T. Sobczyk and J. Zmuda, Phys. Rev. C **91**, no. 4, 045501 (2015).

[35] U. Mosel, Phys. Rev. C **91**, no. 6, 065501 (2015) [arXiv:1502.08032 [nucl-th]].

[36] J. Blietschau *et al.* [Gargamelle Collaboration], Nucl. Phys. B **133**, 205 (1978).

[37] K. Abe *et al.* [T2K Collaboration], Phys. Rev. Lett. **113**, 241803 (2014).

[38] J. Wolcott *et al.* (MINERvA Collaboration), arXiv:1509.05729 [hep-ex].

[39] M. Day and K. S. McFarland, Phys. Rev. D **86**, 053003 (2012).

[40] N. Jachowicz, K. Heyde, J. Ryckebusch and S. Rombouts, Phys. Rev. C **65**, 025501 (2002).

[41] V. Pandey, N. Jachowicz, J. Ryckebusch, T. Van Cuyck and W. Cosyn, Phys. Rev. C **89**, 024601 (2014).

[42] V. Pandey, N. Jachowicz, T. Van Cuyck, J. Ryckebusch and M. Martini, Phys. Rev. C **92**, no. 2, 024606 (2015).

[43] G. Chanfray and P. Schuck, Phys. Rev. A **38**, 4832 (1988).

[44] W. M. Alberico, G. Chanfray, J. Delorme, M. Ericson and A. Molinari, Nucl. Phys. A **634**, 233 (1998).

[45] H. De Vries, C. W. De Jager and C. De Vries, Atom. Data Nucl. Data Tabl. **36** 495 (1987).

[46] W. M. Alberico, M. Ericson and A. Molinari, Nucl. Phys. A **379**, 429 (1982).

[47] M. Ericson and T. E. O. Ericson, Annals Phys. **36**, 323 (1966).

[48] J. Nieves, J. E. Amaro and M. Valverde, Phys. Rev. C **70**, 055503 (2004) [Phys. Rev. C **72**, 019902 (2005)].

[49] K. Abe *et al.* [T2K Collaboration], Phys. Rev. D **87**, 012001 (2013).

[50] A. A. Aguilar-Arevalo *et al.* [MiniBooNE Collaboration], Phys. Rev. D **79**, 072002 (2009).

[51] M. V. Ivanov, G. D. Megias, R. Gonzalez-Jimenez, O. Moreno, M. B. Barbaro, J. A. Caballero and T. W. Donnelly, arXiv:1506.00801 [nucl-th].

[52] A. Meucci and C. Giusti, Phys. Rev. D **91**, no. 9, 093004 (2015).

[53] O. Lalakulich and U. Mosel, Phys. Rev. C **87**, 014602 (2013).

[54] E. Hernandez, J. Nieves and M. J. V. Vacas, Phys. Rev. D **87**, 113009 (2013).

"Neutrino physics is largely an art of learning a great deal by observing nothing."

Haim Harari

4

Summary and Outlook

In recent years, the investigation of the fundamental properties of neutrinos has become a strong and active field in particle and nuclear physics. The confirmation of neutrino-oscillations by the Superkamiokande (1998) and SNO (2001) experiments, which resulted in a Nobel Prize in physics in 2015, opened new frontiers of physics beyond the standard model. The quest for a completion of our knowledge about neutrino-oscillation parameters, mass-squared differences and mixing angles, triggered enormous progress in accelerator-based neutrino-oscillation experiments. These experiments face a number of challenges related to the systematic uncertainties. Major challenges come from the fact that the incident neutrino energy is not precisely known because neutrinos are produced as the decay product of secondary beams of pions and this procedure results in a flux that extends over a wide energy range. The neutrino energy reconstruction is based on the kinematics of the final lepton. Hence in evaluating the neutrino-nucleus responses a number of nuclear effects over a broad kinematical range come into play. Microscopic nuclear structure models are needed in Monte-Carlo generators that model the neutrino-nucleus signal over the whole experimental energy range.

At the same time, neutrino scattering off nucleus also present a great opportunity to study the complexity of nuclear physics. Considering that most of our present knowledge about nuclear-structure physics arose by using electrons and hadrons as probes. Using neutrinos as a probe for nuclear physics provides a great opportunity to complement our knowledge of nuclear physics beyond the one obtained from electron-nucleus scatterings. As an example one can mention the study of the axial structure or the strangeness content of the nucleus. This makes neutrino-nucleus scattering as a great testing ground for nuclear structure, many-body mechanisms and nuclear reaction models.

We present a continuum random phase approximation (CRPA) approach for quasielastic (QE) electron and charged-current (CCQE) neutrino scattering off atomic nuclei. We start the description of the nucleus in a mean-field (MF) approach, i.e., in our initial picture of the nucleus, the nucleons experience the presence of the others through a mean-field generated by their mutual interactions. We obtain the mean-field potential by solving the Hartree-Fock (HF) equations using a Skyrme (SkE2) two-body nucleon-nucleon interaction. In the MF potential, we compute the bound and the continuum single-particle wave functions. In addition, we introduce long-range nuclear correlations by means of the CRPA framework. So, the nucleons which were initially solely under the influence of the HF potential, now additionally interact with each other by means of the residual SkE2 interaction. In this way, a nucleon interacting with an external field is able to exchange energy and momentum with other particles in the nucleus. We solve the CRPA equations using a Green's function method. We use the same Skyrme force to solve both the HF and CRPA equations, making our approach self consistent with respect to the nucleon-nucleon interaction.

We first used our existing nonrelativistic CRPA model to calculate MiniBooNE flux-folded QE contribution to the ^{12}C-antineutrino cross sections in terms of the experimentally measured quantities T_μ and $\cos\theta_\mu$. Overall, we achieved a satisfactory agreement with MiniBooNE measurements especially for forward scattering angles and lower muon kinetic energies. We underestimate the data at higher muon kinetic energies and backward scattering angles. At larger T_μ one observes a significant sensitivity to the choices made with regard to the nucleon-nucleon interaction and the single-particle wave-functions. In light of neutrino axial mass anomaly, we analyzed the impact of axial mass enhancement on the cross section. Enhancing M_A alters not only size but also the shape of the cross sections, mostly at higher T_μ and backward scattering angles.

In order to improve the CRPA formalism not only at lower energies but also at intermediate energies, we employed number of corrections. A folding procedure is used to take into account the spreading width of the single-particle states. We fold the HF and CRPA response functions with a Lorentzian using an effective energy width $\Gamma = 3$ MeV. This makes the description of the giant-resonance region and low-energy nuclear excitations more realistic within the RPA approach. The overall effect of folding is a redistribution of the strength from the peaks to the tails. The energy integrated nuclear responses are not much affected. To improve our description at higher energy and momentum transfers, we implemented relativistic kinematic corrections. The correction is sizable for $q \gtrsim 500$ MeV/c. The overall effect of relativistic corrections is the reduction of the width of the one-body responses and a shift of the QE peak towards smaller values of ω. The SkE2 interaction was optimized against ground-state and low-excitation properties of spherical nuclei. In order to control the strength of the SkE2 force at high virtuality Q^2, a dipole hadronic form factor is introduced at the nucleon-nucleon interaction vertices. Thereby, we introduced a free cut-off parameter, $\Lambda = 455$ MeV, a value which is optimized in a χ^2 test of the comparison of QE $A(e,e')$ CRPA cross sections with the experimental data. We implemented a modified effective momentum approximation (MEMA), in order to take into account the influence of the nuclear Coulomb field on the outgoing lepton.

In order to asses the reliability of our model, we calculated electron-nucleus cross sections for three nuclear targets ^{12}C, ^{16}O, and ^{40}Ca in the kinematic range where QE scattering dominates. We performed a detailed comparison of the HF and CRPA predictions with the experimental data over a broad range of three- and four-momentum transfers: $95 \lesssim q \lesssim 1050$ MeV/c, and $0.009 \lesssim Q^2 \lesssim 0.900$ (GeV/c)^2. Our predictions are reasonably successful in describing the data. We separated the longitudinal and transverse response on ^{12}C, for $300 \lesssim q \lesssim 570$ MeV/c and compared them with the experimental data. An overall satisfactory description of data over the whole QE region validates the reliability of the CRPA approach. Further, we moved to ^{12}C(ν_μ, μ^-) cross sections, relevant for accelerator-based neutrino-oscillation experiments. We illustrated how low-energy nuclear excitations are induced by neutrinos and paid special attention to contributions where nuclear-structure details become important, but remain unobserved in RFG-based models. We show that low-energy excitations can account for non-negligible contributions to the signal of accelerator-based neutrino-oscillation experiments, especially at forward scattering angle.

We calculated flux-folded double-differential cross sections off ^{12}C and compared them with MiniBooNE (CCQE neutrino and antineutrino) and T2K (inclusive QE) measurements. We also compared flux-unfolded total cross section with CCQE measurements of MiniBooNE and T2K. Our antineutrino predictions are in better agreement with the data compared to the neutrino ones. Overall, our calculations describe the gross features of the data. We underestimate the measurements, because of the absence of processes beyond quasielastic (that are present in MiniBooNE and T2K data) in our calculations. We focused on forward scattering bin, made a detailed analysis of the flux-folded double-differential cross sections, and presented a comparison with MiniBooNE and T2K data. The low-energy excitations seem to have a non-negligible contribution in those cross sections at forward scattering angles.

We performed a detailed comparison between two different theoretical models, our CRPA model and the RPA model of Martini *et al*. The approach of Martini *et al* starts from a semiclassical description of the bare polarization propagator with a realistic nuclear density distribution and adds RPA correlations through pion exchange, rho exchange and contact Landau-Migdal parameters. In general, our CRPA approach describes only giant resonances and quasielastic excitations while the Martini *et al.* approach includes quasielastic, multinucleon excitations and also coherent and incoherent pion production. Both approaches are in reasonable agreement in the QE peak region with a trend of more strongly suppressed RPA cross section (due to the mixing with Δ excitations) compared to the CRPA ones. The most significant difference in the two approaches is in the description of giant resonances in CRPA results. We also compared ν_e T2K and MiniBooNE flux-folded cross sections within two approaches. Further, we analyzed ν_e *vs* ν_μ cross sections, relevant for the experiments looking for ν_μ to ν_e oscillations. Due to the different lepton masses, the ν_e cross sections are in general expected to be larger than the ν_μ ones. But at low energies and forward scattering angles, for 1p-1h excitations, we found that ν_μ cross section dominates over the ν_e ones.

Outlook

In the ongoing effort to model neutrino-nucleus interactions for the precise measurement of neutrino-oscillation parameters, much more data is expected from current and planned accelerator-based neutrino oscillation (T2K, NOvA, DUNE, etc.) and neutrino-interaction (MINERvA, CAPTAIN-MINERvA, etc.) facilities around the world. The current version of the CRPA model can be used to model interactions from low-energy to the QE region. The neutrino energy fluxes are increasingly spanning a broader energy range, and further moving towards higher energies. Processes beyond QE, such as multinucleon excitations, pion production and other excitations in the nucleon resonance region will be required to fully model the neutrino-nucleus response in those experiments. Also, further modeling of electron- and neutrino-argon scattering will be required in near future, since the planned facilities are moving towards use of a liquid argon TPC (LArTPC) where the target will be argon nuclei.

The JPARC spallation neutron source will uniquely allow the possibility of mono-energetics kaon decay-at-rest (KDAR) neutrinos of 236 MeV. They expect to collect a sample of between 150,000 and 300,000 charged current events in 50 tons of fiducial volume in its 5 year run, which is expected to start in a couple of years. These low-energy mono-energetic neutrinos, pose a unique possibility to study nuclear structure with a weak-interaction-only probe. At this energy, a significant contribution to the cross section arise from $\omega < 50$ MeV excitations, where current CRPA model can describe the cross section significantly better than other models and the neutrino-induced low-energy nuclear excitations can be confronted with the data. These studies will be highly relevant to model neutrino interactions in experiments with a large fraction of few-hundred-MeV neutrinos, for example, T2K, MOMENT, the European Spallation Source Neutrino Super Beam (ESSSB), and a CERN-SPL-based neutrino beam CP search.

Samenvatting

Tijdens de voorbije decennia kwam het onderzoek van de fundamentele eigenschappen van neutrino's binnen de deeltjes- en kernfysica in een stroomversnelling terecht. De bevestiging van het bestaan van neutrino-oscillaties door de SuperKamiokande en SNO collaboraties–die resulteerde in een Nobelprijs in 2015- verlegde de grenzen van de neutrinofysica voorbij deze van het Standaard Model. De verdere ontwikkeling van versnellergebaseerde neutrino-oscillatie experimenten, leidde tot een enorme vooruitgang in de zoektocht naar een vollediger beeld van neutrino-oscillatie parameters, neutrinomassa's en menghoeken. Deze experimenten worden geconfronteerd met een aantal uitdagingen en onzekerheden. Een belangrijke bron van systematische onzekerheden vindt zijn oorzaak in het feit dat de individuele neutrino-energieën in het experiment niet gekend zijn omdat de neutrino's geproduceerd worden bij het verval van een pionbundel. De neutrino-energie in een reactie moet dan gereconstrueerd worden aan de hand van de kinematica van het lepton dat geproduceerd wordt bij de interactie. Een goed begrip van de interactie van het neutrino met de atoomkernen in het trefmateriaal is dan ook noodzakelijk om systematische onzekerheden te controleren.

In dit werk wordt een continuum random phase approximation (CRPA) methode gebruikt voor de beschrijving van quasi-elastische neutrinoverstrooiing aan atoomkernen. De beschrijving van de kern start met een gemiddeld-veld benadering. De gemiddeld-veld potentiaal wordt bepaald door de Hartree-Fock vergelijkingen op te lossen met de SkE2 Skyrme parametrisatie als residuele interactie. De gebonden en continuüm ééndeeltjesgolffuncties dienen dan als uitgangspunt voor de introductie van langedrachtcorrelaties binnen een CRPA beeld. De oplossing van de CRPA-vergelijkingen maakt gebruik van Greense-functietechnieken. De invoering van een dipoolvormfactor op de nucleon-nucleon interactievertex voorkomt dat de RPA-correlaties onrealistisch sterk worden bij hoge Q^2. Binnen de RPA-beschrijving wordt een meer realistische breedte van lage-energie excitaties en resonanties in het reuzeresonantie gebied verkregen door de responsfuncties te vouwen met een Lorentziaan. De invloed van het Coulombveld dat de kern uitoefent op het uitgaande lepton werd geïmplementeerd met een effectieve momentum benadering (MEMA). Bovendien worden voor reacties bij hoge energie- en momentumoverdracht ook relativistische correcties op een effectieve manier in rekening gebracht.

De berekeningen worden geconfronteerd met elektron-verstrooiingsdata waar de voorspellingen van het model in goede overeenstemming blijken te zijn met de data. Een belangrijk pluspunt van dit model is dat het in staat is zowel het quasi-elastische gebied als het reuze-resonantie gebied te beschrijven. Dit laatste biedt een rijke bron van informatie over de structuur van de kern.

We vouwen neutrino- en antineutrino verstrooiingswerkzame doorsneden met de experimentele energiedistributies en vergelijken deze met de MiniBooNe geladen stroom ν en $\overline{\nu}$ en inclusieve quasi-elastische en geladen stroom quasi-elastische ν T2K data. Onze berekeningen onderschatten de metingen lichtjes, wat te wijten is aan de contaminatie van de data met niet zuiver quasi-elastische processen, waarvan het effect niet in de berekeningen werd opgenomen. Er wordt bijzonder aandacht besteed aan lage-energie excitaties die een merkbare invloed hebben op voorwaartse leptonverstrooiingsprocessen, zelfs bij de relatief hoge experimentele energieën. Omdat verschillen tussen elektron- en muonneutrino geïnduceerde processen belangrijk zijn voor oscillatie-experimenten wordt ook hier speciaal aandacht aan besteed.